FUNDAMENTAL STUDIES OF CATALYTIC DEHYDROGENATION ON ALUMINA-SUPPORTED SIZE-SELECTED PLATINUM CLUSTER MODEL CATALYSTS

by

Eric Thomas Baxter

A dissertation submitted to the faculty of
The University of Utah
in partial fulfillment of the requirements for the degree of

Doctor of Philosophy

Department of Chemistry

The University of Utah

May 2018

The University of Utah Graduate School

STATEMENT OF DISSERTATION APPROVAL

The dissertation of **Eric Thomas Baxter**

has been approved by the following supervisory committee members:

Scott L. Anderson	, Chair	**11/13/2017** Date Approved
Peter B. Armentrout	, Member	**11/13/2017** Date Approved
Marc D. Porter	, Member	**11/13/2017** Date Approved
Ilya Zharov	, Member	**11/13/2017** Date Approved
Sivaraman Guruswamy	, Member	**11/13/2017** Date Approved

and by **Cynthia J. Burrows**, Chair/Dean of

the Department/College/School of **Chemistry**

and by David B. Kieda, Dean of The Graduate School.

ABSTRACT

The research presented in this dissertation focuses on the use of platinum-based catalysts to enhance endothermic fuel cooling. Chapter 1 gives a brief introduction to the motivation for this work. Chapter 2 presents fundamental studies on the catalytic dehydrogenation of ethylene by size-selected Pt_n (n = 4, 7, 8) clusters deposited onto thin film alumina supports. The model catalysts were probed by a combination of experimental and theoretical techniques including; temperature-programmed desorption and reaction (TPD/R), low energy ion scattering spectroscopy (ISS), X-ray photoelectron spectroscopy (XPS), plane wave density-functional theory (PW-DFT), and statistical mechanical theory. It is shown that the Pt clusters dehydrogenated approximately half of the initially adsorbed ethylene, leading to deactivation of the catalyst via (coking) carbon deposition. The catalytic activity was observed to be size-dependent and strongly correlated to the cluster structure, with Pt_7 demonstrating the highest activity.

In Chapter 3 the focus turns to selectively doping Pt_7 clusters with boron. A combination of experiment and theory were used investigate the alkene-binding affinity of the bimetallic (Pt_nB_m/alumina) model catalysts. A comparison of the theoretical and experimental results show that doping the Pt clusters with boron modifies the alkene-binding affinity and thus the tendency toward dehydrogenation to coke precursors.

Chapter 4 describes a way to produce bimetallic (Pt_nB_m/alumina) model catalysts by exposing prepared Pt_n/alumina samples to diborane and heating. It is shown that the

diborane exposure/hearting procedure results in the preferential binding of B to the Pt clusters.

TABLE OF CONTENTS

ACKNOWLEDGMENTS

I would like to thank Scott L. Anderson for giving me the opportunity to work in his laboratory, first as an undergraduate student, and then as a graduate student. His willingness to have discussions, share his experiences, and to provide encouragement has played a vital role in my development as a research scientist.

I would also like to thank the other members of my committee: Professor Peter B. Armentrout, Professor Marc D. Porter, Professor Ilya Zharov, and Professor Sivaraman Guruswamy for constantly challenging me as a scientist.

I would also like to thank the members of the Anderson group for creating an enjoyable environment to learn and develop as a scientist.

Most of all, I would like to thank my family: my parents Jeffrey and Tonya, my sister, Stephanie, and my brother, Matthew. Without their endless love and support I would never have had the drive to make it this far in my academic career.

CHAPTER 1

INTRODUCTION

1.1 Motivation

Hypersonic flight could revolutionize both commercial and commuter travel by significantly reducing the travel time. For example, travel from London to New York would take approximately two hours at hypersonic speeds. However, hypersonic flight has a major problem when it comes to dealing with the increased vehicle and engine heat as the aircraft speeds are increased. To sustain hypersonic flight would require a heat sink of approximately 3,500 kJ/kg to cool the engine and other vehicle components when traveling at speeds eight times the speed of sound.[1-5] The fuel may be the most promising source of cooling. The required heat sink of ~3,500 kJ/kg, equivalent to temperatures on the order of 700°C, can be achieved by flowing fuels that undergo endothermic (heat-adsorbing) reactions through channels machined into the walls of the vehicle, engine, and subsystems to adsorb the waste heat. Unfortunately, solid carbon deposits begin to form as the temperature of the fuel rises beyond the onset of thermal cracking (~750 K) for hydrocarbons. Solid carbon deposits ("coke") can interfere with heat transfer, clog fuel lines and filters, and disable fuel controls eventually leading to a system failure. Coke formation can occur through several mechanisms: interactions between hydrocarbons and the metal surfaces results in the formation of filamentous carbon; deposition of high-molecular-weight liquids (tar) results in amorphous carbon; amorphous carbon can also be formed on the surface from addition of small molecules and radicals. The formation of filamentous carbon can be avoided by careful selection of surface materials. The use of catalysts to selectively drive desired endothermic reactions (dehydrogenation of an alkane to produce an alkene and hydrogen) at temperatures below (~750 K) the onset of thermal cracking could provide a way to circumvent the formation of amorphous carbon.[5]

Platinum's ability to (de)hydrogenate hydrocarbons has been extensively studied making it a material of interest in many catalytic applications.[6,7] However, platinum catalysts have a tendency to deactivate during dehydrogenation reactions due to an accumulation of coke precursors. DFT-calculated potential energy surfaces for ethane dehydrogenation on the step and terrace sites of a Pt(433) single crystal show that ethane can readily dehydrogenate to ethylene.[8] However, on the under-coordinated sites (e.g., step sites) further dehydrogenation is enhanced leading to the formation of coke precursors and the deactivation of the catalysts. One strategy for minimizing the formation of coke might be to selectively block the highly active under-coordinated sites. It has been demonstrated that boron-doping the extended surfaces of Co[9] and Ni[10] extends the lifetime of the catalyst without compromising their catalytic activity in Fisher Tropsch synthesis and steam reforming, respectively. The results of the boron-doping were attributed to boron selectively blocking the step and subsurface octahedral sites, therefore, reducing the nucleation of graphene islands.

Model catalysts with atomically size-selected metal clusters deposited on well characterized supports can provide a useful means for studying catalytic mechanisms by allowing for independent control of the size and density of active catalytic sites.[11-19] Metal alloys/bimetallic catalysts can provide a valuable opportunity to tune catalytic activity, selectivity, and stability. However, extending the size-selected metal cluster approach to bimetallic clusters can be difficult. Synthesis of bimetallic clusters generally results in a wide distribution of cluster composition and structures limiting the ability to derive structure-property relations using characterization techniques (e.g., x-ray photoelectron spectroscopy) that provide information averaged over all the sites.

The work included within this dissertation provides results from studying the interactions between ethylene and alumina supported size-selected Pt_n (n= 4, 7, 8) model catalysts with and without boron doping. The results show that Pt_7 both binds and dehydrogenates ethylene more efficiently than Pt_4 and Pt_8, which is correlated to the diverse distribution of cluster morphologies accessible to Pt_7 under the reaction conditions. Exposing the Pt_7/alumina samples to diborane followed by heating results in the preferential deposition of boron atoms onto the Pt clusters. Boration of Pt clusters reduces the ethylene binding energies, such that ethylene preferentially desorbs intact rather than dehydrogenating to form coke precursors.

1.2 References

1. Lander, H. R., Jr.; Nixon, A. C. Endothermic Fuels for Hypersonic Vehicles. *J. Aircr.* **1971**, *8*, 200- 7.

2. Maurice, L.; Edwards, T.; Griffiths, J. Liquid Hydrocarbon Fuels for Hypersonic Propulsion. *Prog. Astronaut. Aeronaut.* **2000**, *189*, 757-822.

3. Edwards, T. Liquid Fuels and Propellants for Aerospace Propulsion: 1903-2003. *J. Propulsion Power* **2003**, *19*, 1089-1107.

4. Jackson, T. A.; Eklund, D. R.; Fink, A. J. High Speed Propulsion: Performance Advantage of Advanced Materials. *J. Mater. Sci.* **2004**, *39*, 5905-5913.

5. Edwards, T. Cracking and Deposition Behavior of Supercritical Hydrocarbon Aviation Fuels. *Combust. Sci. and Tech.* **2006**, *178*, 307-334.

6. Vajda, S.; Pellin, M. J.; Greeley, J. P.; Marshall, C. L.; Curtiss, L. A.; Ballentine, G. A.; Elam, J. W.;Catillon-Mucherie, S.; Redfern, P. C.; Mehmood, F.; Zapol, P. Subnanometre Platinum Clusters as Highly Active and Selective Catalysts for the Oxidative Dehydrogenation of Propane. *Nat. Mater.* **2009**, *8*, 213-216.

7. Goddard, S. A.; Cortright, R. D.; Dumesic, J. A. Deuterium Tracing Studies and Microkinetic Analysis of Ethylene Hydrogenation over Platinum. *J. Catal.* **1992**, *137*, 186-198.

8. Anderson, S. L.; Alexandrova, A. N.; Dumesic, J. A.; Mavrikakis, M.; Khanna, S.

N.; Winans, R. E.; Zare, R. N. *Catalyst and Fuel Interactions to Optimize Endothermic Cooling*; Air Force Office of Scientific Research, U.S. Government Printing Office: Washington, DC, 2016; 68

9. Tan, K. F.; Chang, J.; Borgna, A.; Saeys, M. Effect of Boron Promotion on the Stability of Cobalt Fischer–Tropsch Catalysts. *J. Catal.* **2011**, *280*, 50-59.

10. Xu, J.; Chen, L.; Tan, K. F.; Borgna, A.; Saeys, M. Effect of Boron on the Stability of Ni Catalysts During Steam Methane Reforming. *J. Catal.* **2009**, *261*, 158-165.

11. Heiz, U.; Schneider, W.-D. Nanoassembled Model Catalysts. *J. Phys. D: Appl. Phys.* **2000**, *33*, R85.

12. Goodman, D. W. Catalysis by Metals: From Extended Single Crystals to Small Clusters. *Surf. Rev. Lett.* **1994**, *1*, 449 -55.

13. Rainer, D. R.; Xu, C.; Goodman, D. W. Characterization and Catalysis Studies of Small Metal Particles on Planar Model Oxide Supports. *J. Mol. Catal. A: Chem.* **1997**, *119*, 307-325.

14. Henry, C. R. Surface Studies of Supported Model Catalysts. *Surf. Sci. Rep.* **1998**, *31*, 231235-233325.

15. Campbell, C. T.; Grant, A. W.; Starr, D. E.; Parker, S. C.; Bondzie, V. A. Model Oxide-Supported Metal Catalysts: Energetics, Particle Thicknesses, Chemisorption and Catalytic Properties. *Top. Catal.* **2000**, *14*, 43-51.

16. Lim, D.-C.; Hwang, C.-C.; Ganteför, G.; Kim, Y. D. Model Catalysts of Supported Au Nanoparticles and Mass-Selected Clusters. *Phys. Chem. Chem. Phys.* **2010**, *12*, 15172-15180

17. Habibpour, V.; Wang, Z. W.; Palmer, R. E.; Heiz, U. Size-Selected Metal Clusters: New Models for Catalysis with Atomic Precision. *J. Appl. Sci.* **2011**, *11*, 1164-1170.

18. Gao, F.; Goodman, D. W. Model Catalysts: Simulating the Complexities of Heterogeneous Catalysts. *Annu. Rev. Phys. Chem.* **2012**, *63*, 265-286.

19. Heiz, U.; Sanchez, A.; Abbet, S.; Schneider, W.-D. Tuning the Oxidation of Carbon Monoxide Using Nanoassembled Model Catalysts. *Chem. Phys.* **2000**, *262*, 189-200.

CHAPTER 2

ETHYLENE DEHYDROGENATION ON $Pt_{4, 7, 8}$ CLUSTERS ON Al_2O_3: STRONG CLUSTER SIZE DEPENDENCE LINKED TO PREFERRED CATALYST MORPHOLOGIES

2.1 Overview

Catalytic dehydrogenation of ethylene on size-selected Pt_n (n = 4, 7, 8) clusters deposited on the surface of Al_2O_3 was studied experimentally and theoretically. Clusters were mass-selected, deposited on the alumina support, and probed by a combination of low energy ion scattering, temperature-programmed desorption and reaction of C_2D_4 and D_2, X-ray photoelectron spectroscopy, density functional theory, and statistical mechanical theory. Pt_7 is identified as the most catalytically active cluster, while Pt_4 and Pt_8 exhibit comparable activities. The higher activity can be related to the cluster structure and particularly to the distribution of cluster morphologies accessible at the temperatures and coverage with ethylene in catalytic conditions. Specifically, while Pt_7 and Pt_8 on alumina have very similar prismatic global minimum geometries, Pt_7 at higher temperatures also has access to single-layer isomers, which become more and more predominant in the cluster catalyst ensemble upon increasing ethylene coverage. Single-layer isomers feature greater charge transfer from the support and more binding sites that activate ethylene for dehydrogenation rather than hydrogenation or desorption. Size-dependent susceptibility to coking and deactivation was also investigated. Our results show that size-dependent catalytic activity of clusters is not a simple property of single cluster geometry but the average over a statistical ensemble at relevant conditions.

2.2 Introduction

The subnano clusters are known to have special catalytic reactivity.[1-4] For example, a specific range of cluster size often results in preferential reaction pathways or significantly altered reactivity because in the subnano regime clusters are affected by

size-dependent electronic and geometric structure. One issue complicating this situation is that there may be multiple thermally accessible cluster structures with significantly different electronic and binding site properties. Here, we use a combination of experimental probes of cluster structure and binding site distributions together with density functional theory (DFT) to explore the range of thermally accessible structures and study the effects of size-dependent cluster structure on ethylene binding and dehydrogenation.

Platinum's ability to (de)hydrogenate hydrocarbons is well-documented, and it is of interest to see if small clusters of Pt can be good dehydrogenation catalysts with useful selectivity that might enable more economical use of precious metals in catalysis. An important part of the problem is the stability of small clusters with respect to both sintering or agglomeration and deactivation by carbon deposition (coking).[5-8]

This work focuses on catalytic dehydrogenation on Pt_4, Pt_7, and Pt_8 clusters supported on alumina. Significant differences have been found experimentally between Pt_7 and Pt_8, here and elsewhere, and much of our effort is focused on understanding why. Pt_4 was included as an example of a smaller cluster. In this size range, strong size effects on activity have been noted. Vajda *et al*. observed $Pt_{8–10}$'s activity of 40–100 times for oxidative dehydrogenation of propane;[2] Roberts *et al*. observed strongly size-dependent activity for CO oxidation, which was correlated to changes in both the valence electronic structure and the number of CO binding sites on top of the clusters.[9]

There is evidence suggesting that such effects may be at least partly related to a structural transition occurring around Pt_7 and Pt_8. Low energy ion scattering (ISS) for Pt_n/alumina/Re(0001) showed an abrupt ~15% drop in the Pt ISS signal going from Pt_7 to

Pt_8, indicating a transition to morphologies where fewer Pt atoms are in the ISS-accessible top layer of the clusters.[9] As discussed below, we verified that the effect also occurs for the Pt_n/alumina/Ta(110) system studied here. Indeed, the drop between Pt_7 and Pt_8 is actually somewhat larger (~24%) for alumina/Ta(110). The inference of a drop in the fraction of Pt in the surface layer at Pt_8 is consistent with a scanning tunneling microscopy study of Pt_n/TiO_2 by Watanabe *et al.*[10, 11] who observed a transition from single- to multilayer clusters between Pt_7 and Pt_8. Such transitions change the number and type of adsorbate binding sites exposed on the clusters; however, it is important to recognize that adsorbate binding can drive cluster isomerization, i.e., it is necessary to characterize both adsorbate-free and adsorbate-covered structures. As shown below, Pt_7 is able to adsorb more ethylene than Pt_4 or Pt_8, on either a per Pt atom or per cluster basis, consistent with additional Pt atoms exposed in the surface layer. DFT allows this effect and the earlier ISS observations to be explained.

2.3 Results and Discussion

We begin by discussing DFT results for adsorbate-free Pt_7 and Pt_8 on α-alumina, as summarized in Figure 2.1 and Table A.4. The charges on the Pt atoms in each structure are indicated and discussed below.

2.3.1 Cluster Catalyst Structures

Small Pt clusters have many structural isomers with similar energies,[12] and both Pt_7/alumina and Pt_8/alumina are found to have 5–7 isomers of very different geometries, predicted to be populated in the 450–700 K temperature range where dehydrogenation is

observed. At the elevated temperatures relevant to catalysis and in the limit of no kinetic trapping, strong structural fluxionality and the presence of several isomers are expected.[13] Because catalytic properties may be dominated by any one or few of the isomers, it is important to consider all thermally relevant structures.[14] We will generally describe the structures as being either single-layer, where all Pt atoms are exposed in the surface layer, or prismatic, where one or more atoms are buried under the cluster surface. The lowest energy isomers of Pt_7 and Pt_8 on alumina are shown in Figure 2.1 together with their Bader charges and Boltzmann populations at 700 K. Pt_7 is found to have both single layer and prismatic structures in the thermally accessible set, with prismatic geometries (global minimum and fourth isomer) comprising 66.7% of the Boltzmann population at 700 K and with the balance being single-layer geometries (second, third, and fifth isomers). In contrast, all of the accessible isomers of Pt_8 are prismatic.

The calculated structures provide an explanation for the ISS observation that the fraction of Pt in surface layer drops between Pt_7 and Pt_8.[9] ISS was done at 130 K; thus, if the isomer distribution is equilibrated, only the lowest energy structures of each cluster would have significant populations. For Pt_7, this structure is prismatic but exposes 6 of its 7 atoms (i.e., ~86%) in the ISS-accessible surface layer. The lowest energy isomer of Pt_8 exposes only 6 of its 8 atoms (75%) in the surface layer; thus, we would predict a ~12.5% drop in ISS intensity between Pt_7 and Pt_8. It is not unlikely; however, that there are barriers to isomerization, such that some higher energy structures remain as the sample is cooled. To the extent that this kinetic trapping occurs, it would tend to give an even larger intensity drop between Pt_7 and Pt_8 because Pt_7 has several single layer isomers where 100% of the Pt would be detectable, whereas all of the Pt_8 isomers are

prismatic.

At higher temperatures, relevant to the temperature-programmed desorption and reaction (TPD/R) experiments, the diversity of geometries of Pt_7 offers a richer set of binding sites for ethylene as opposed to the more uniform structures populated for Pt_8, and this should be reflected in the chemical activity.

2.3.2 Size-Dependent Catalytic Activity

The chemical properties of the clusters, as probed by TPD/R, are summarized in Figure 2.2 for two consecutive TPD/R experiments on samples containing Pt_4, Pt_7, and Pt_8. For each experiment, the samples were dosed with 5 L of C_2D_4 at 150 K and then cooled to ~130 K prior to each TPD/R heat ramp (3 K/sec). Figure 2.2 shows results for the two species, C_2D_4 and D_2, observed to have significant desorption signals. Desorption is reported in terms of C_2D_4 or D_2 molecules desorbing per Pt atom per second, taking advantage of the fact that we know the Pt loading quite precisely ($1.5 \times 10^{14}/cm^2$). The D_2 signals were corrected for the contribution from mass spectrometer cracking of desorbing C_2D_4, and the uncorrected data are reported in Figure A.1. To avoid interference from high background signals at masses 2 and 28, most experiments were done with C_2D_4. Experiments with C_2H_4 were also done to look for acetylene desorption; however, none was observed. In addition, no signal for ethane was observed, indicating that hydrogenation is negligible under these conditions.

C_2D_4 desorption from the cluster-free alumina/Ta(110) support is shown for comparison to the Pt_n/alumina results. Only the result of the first TPD/R run is shown because the second run was identical. To allow direct comparison, the data for cluster-

free alumina were scaled as if these samples also contained the same amount of Pt as the Pt_n/alumina samples. For the cluster-free alumina film, C_2D_4 began to desorb at the TPD starting temperature with desorption peaking at ~165 K and rapidly declining at higher temperatures. After correcting for the contribution from C_2D_4 cracking in the mass spectrometer, the D_2 signal is zero, i.e., all ethylene adsorbed on the alumina film desorbs intact. The integrated number of C_2D_4 molecules desorbing from alumina is ~$7 \times 10^{12}/cm^2$, i.e., on the order of 0.01 ML. The low intensity indicates that ethylene does not bind stably to most sites on the alumina film at 150 K but that there are a few stable binding sites, presumably corresponding to defects in the alumina surface. Even these defect sites bind C_2D_4 weakly such that it desorbs intact, well below room temperature. For the cluster-containing samples, ethylene desorption also begins as the heat ramp is started with a sharp peak near ~165 K for all three cluster sizes. There is weak D_2^+ signal at low temperatures (Figure A.1), but this is entirely due to dissociative ionization of desorbing C_2D_4. Both the temperature dependence and intensity of the 165 K peak match those for cluster-free alumina, indicating that this low temperature feature is simply due to C_2D_4 desorbing from defect sites on the alumina film. The fact that this low temperature component is not significantly affected by deposition of 0.1 ML equivalent of Pt_n suggests that the clusters do not diffuse to and occupy these defect sites, at least in the <300 K range where Pt_n deposition, C_2D_4 exposure, and desorption of the low temperature feature occur.

For Pt_n-containing samples, there is also a broad C_2D_4 desorption component extending between ~200 and 420 K, which clearly results from ethylene bound to the Pt clusters. The peak temperature of this component is ~280 K for Pt_4 and Pt_8 and ~300 K

for Pt_7, and the intensity is also significantly higher for the Pt_7-containing sample. Below ~250 K (Pt_4, Pt_8) or ~275 K (Pt_7), only intact C_2D_4 desorption is observed, but at higher temperatures, D_2 desorbs in a broad component extending to 650 K. In each case, the onset of D_2 desorption is just below the peak C_2D_4 desorption temperature, as would be expected if dehydrogenation to generate D_2 is in competition with C_2D_4 desorption. Figure 2.1 also lists the integrated amounts of C_2D_4 and D_2 observed to desorb from each sample, given in terms of number of molecules desorbing per Pt atom. Desorption/cm^2 can be obtained simply by multiplying by the Pt coverage (1.5×10^{14} Pt atoms/cm^2). These numbers include desorption from both alumina and Pt_n sites, and to compare the Pt_n-only desorption, it is necessary to subtract the alumina contribution, equivalent to ~0.08 C_2D_4/Pt atom. Thus, in the first TPD/R experiment, the corrected desorption is 0.24 C_2D_4 and 0.13 D_2 molecules per Pt atom for Pt_4, compared to 0.30 C_2D_4 and 0.20 D_2 for Pt_7, and 0.23 C_2D_4 and 0.15 D_2 for Pt_8.

No additional D_2 desorption was observed in select experiments where the temperature was ramped to 900 K, thus it is reasonable to assume that dehydrogenation is complete by 650 K. In that case, the total number of initially adsorbed C_2D_4 molecules per Pt_n cluster can be estimated as the sum of the C_2D_4 desorption plus half the D_2 desorption. This amounts to ~0.3 C_2D_4/Pt atom for both Pt_4 and Pt_8, compared to 0.4 C_2D_4/Pt atom for Pt_7. The numbers of C_2D_4 molecules initially adsorbed per cluster are ~1.1, ~2.7 and ~2.4, respectively, for Pt_4, Pt_7, and Pt_8. Thus, Pt_7 provides significantly more binding sites than the other two cluster sizes on either a per atom or per cluster basis.

Study of small supported clusters is complicated by substrate-mediated

adsorption, in which molecules initially land on the alumina support, where they bind too weakly to be stable, diffuse, and bind stably to the Pt_n. For our experiments with 0.1 ML equivalent Pt coverage, the effect is to substantially amplify the effective adsorbate exposure to the clusters, as will be demonstrated for C_2D_4 below. During the ~20 min elapsing between the start of cluster deposition and the first TPD/R heat ramp, the clusters, on average, are exposed to ~0.04 L of background CO, corresponding to ~0.01 CO impacting per surface atom. During the first TPD/R run, CO desorption amounting to ~0.5 CO molecules/cluster is observed, independent of cluster size. CO binds strongly to Pt_n (see below) and likely competes with C_2D_4 for Pt binding sites. Therefore, we expect that the integrated C_2D_4 numbers are somewhat lower than they would be if no CO were present.

As discussed above, a larger fraction of the Pt atoms is exposed in the surface layer of Pt_7/alumina compared to that in Pt_8/alumina, consistent with the observation that more C_2D_4 adsorbs on Pt_7 than on Pt_8. Clearly; however, understanding the TPD/R experiments requires consideration of how the Pt_n isomer distribution is affected by ethylene adsorption and also of the factors that control branching between ethylene desorption and dehydrogenation.

Before discussing DFT results for ethylene-Pt_n interactions, we consider the question of whether the temperature dependence observed for D_2 desorption is controlled by the energetics of C_2D_4 decomposition or simply reflects the activation energy for desorption of D_2. This point was tested by studying D_2 TPD, and Figure A.2 compares the D_2 desorption from separate samples of Pt_8/alumina/Ta(110) after 5 L exposure to either D_2 or C_2D_4 at 150 K. It can be seen that for the D_2 exposure, desorption starts at

~160 K compared to ~220 K for the C_2D_4 exposure and is 90% complete by ~400 K, at which point only about half the D_2 from C_2D_4 has desorbed. In this temperature range, D_2 desorption from Pt almost certainly involves recombination of absorbed D atoms; thus, the higher temperatures required to drive D_2 desorption after C_2D_4 exposure suggest that the limiting factor is the activation energy for some step(s) in the C_2D_4 decomposition process rather than the D_2 recombinative desorption energetics.

The desorption spectra were simulated to extract activation energies as described in Appendix A, which reports the best-fit energy distributions in Figure A.3. Simulation was based on assuming first-order kinetics for the limiting step, as might be expected for intact C_2D_4 desorption. On the basis of this assumption, the desorption energy for C_2D_4 bound on the alumina film is in the ~0.5 eV range, while for C_2D_4 at Pt cluster sites, the desorption energy would range from ~0.6 to 1.4 eV. For D_2 production, under the assumption of a first-order limiting step, the activation energy would be in the 0.7–2.3 eV range. A combination of DFT and coverage-dependent TPD/R studies was used to probe C_2D_4 adsorption and desorption, resulting in a more complex picture of the process.

Because theory on supported cluster systems is computationally demanding due to the large number of isomers and adsorption geometries involved, we focus our DFT work on ethylene adsorption and activation for dehydrogenation as the key processes influencing the kinetics for ethylene and hydrogen desorption. In addition, we chose the Pt_7/alumina system for the most in-depth work, both experimentally and theoretically. Because the TPD results indicate that roughly three C_2D_4 molecules adsorb initially per Pt_7, we consider theoretically adsorption of one, two, and three ethylene molecules on the most important Pt_7 isomers and also the factors that influence desorption vs

dehydrogenation.

The literature for ethylene binding and hydrogenation/dehydrogenation on various Pt surfaces provides an important insight that aids interpretation of the DFT results. Ethylene adsorption and decomposition has been extensively studied on various platinum surfaces using techniques such as TPD, reflection/absorption infrared spectroscopy (RAIRS), and high-resolution electron energy loss spectroscopy (HREELS). At temperatures below 100 K, adsorbed ethylene forms di-σ bonds on close-packed Pt(111)[15, 16] and Pt(100)[17] surfaces and π-bonds on the stepped sites of Pt(210) and (1 × 1)Pt(110).[18] On the close-packed surfaces, some of the di-σ bound ethylene desorbs intact at temperatures around 285 K; however, TPD of C_2D_4 and C_2H_4 coadsorbed on Pt(111) also yielded C_2D_3H and C_2H_3D, indicating that recombinative desorption of dissociatively chemisorbed ethylene also contributes to the ethylene desorption signal.[19] At temperatures just above the ethylene desorption peak, H_2 desorption begins, indicating the onset of dehydrogenation. The first dehydrogenation step results in formation of ethylidyne ($\equiv CCH_3$), which has been shown to adsorb in 3-fold hollow sites by HREELS[20] and tensor LEED.[21] Most studies consider ethylidene to be a spectator species.[22-24] At higher temperatures, the ethylidyne undergoes further decomposition, giving rise to additional H_2 desorption and going to completion by ~700 K. For the stepped surface of Pt(210), some of the π-bound ethylene desorbs at ~250 K, and then the remaining π-bound ethylene dehydrogenates at ~300 K, resulting in desorption of H_2 and formation of adsorbed ethylylidyne ($\equiv CCH_2-$, both C atoms bound to the surface), which undergoes further decomposition, giving rise to additional H_2 desorption and going to completion by ~700 K. In contrast, upon heating the (1 × 1)Pt(110) surface to ~160 K,

some of the π-bound ethylene is converted to di-σ bound ethylene. Between 270 and 330 K, the adsorbed ethylene reacts to form carbon atoms and ethylidyne on the surface accompanied by desorption of methane and H_2. The remaining ethylidyne undergoes complete dehydrogenation by 450 K. Studies on alumina-supported Pt nanoparticles showed that at temperatures below 180 K, ethylene adsorbs in three distinct forms: π-bound ethylene, di-σ bound ethylene, and the ethylidyne species.[25] By room temperature, all of the π-bound ethylene desorbs intact, while at higher temperatures, the remaining di-σ bound ethylene is converted to ethylidyne.

From the perspective of interpreting the DFT results, the key insight from these studies is a correlation between the adsorbed configuration of ethylene and its subsequent reactivity.[22, 24, 26-29] This correlation, which applies to both Pt surfaces and Pt clusters, is that π-bonded, sp^2 configurations tend to result in hydrogenated products, while di-σ bonded, sp^3 configurations result in dehydrogenated products. For our system, where no hydrogen is added and hydrogenation is not observed, we interpret this correlation as suggesting that the precursor to dehydrogenation is di-σ bonded ethylene, while π-bonded ethylene should tend to desorb intact. Our bonding analysis of ethylene adsorbed to Pt_7 corresponds well to near-edge X-ray-absorption fine-structure (NEXAFS) studies on Pt(111) with di-σ bound ethylene reflecting a bond-length of ∼1.5 Å and π-bound ∼1.4 Å.[29] Moreover, bond angles of ≈120° and ≈97–115° reflect sp^2 and sp^3 hybridization present in adsorbed ethylene, respectively. We therefore will use the geometries calculated for adsorbed ethylene as indicators of the propensity to dehydrogenate.

Figure 2.3 shows the DFT results for ethylene binding to both the single layer and prismatic Pt_7 isomers that were shown in Figure 2.1. The most stable structures (i) are

shown at the top, and additional local minima are shown below, with energetics and thermal populations summarized in Table 2.1. Recall that for adsorbate-free Pt_7/alumina, the global minimum is prismatic; however, because the binding energy for the first ethylene molecule is ~0.6 eV higher for the single-layer isomer, this becomes the global minimum for ethylene$_1$/Pt_7, and a variety of low energy ethylene$_1$/Pt_7 geometries based on the single layer isomer are shown in the left column. With one ethylene molecule adsorbed, the prismatic isomers shown in the second column are therefore local minima, stabilized by barriers associated with the considerable rearrangement required to convert to the single layer global minimum.

Bader charge analysis shows that ethylene adsorption is associated with electron transfer from Pt_n to the carbon atoms of ethylene, suggesting that the charges on the adsorbate-free Pt_n/alumina isomers should be related to their affinities for ethylene. The charges on each atom given in Figure 2.1 show that on average, Pt_7 has greater electron transfer from the support compared to that of Pt_8. Pt_7 isomers take up 1.22–1.44 e^- compared to 0.80–1.24 e^- for Pt_8. In addition, the single-layer Pt_7 isomers have higher charge than the prismatic isomers and less uniform charge distributions, with some Pt atoms carrying the majority of the negative charge. Pt_8, which has only prismatic isomers, has more uniform and lower charge distributions.

In principle, the extent of Pt_n charging can be probed by XPS, and Pt 4d spectra for Pt_7/alumina and Pt_8/alumina are shown in Figure A.4. The stronger Pt 4f peaks were unusable because of Al 2p background. Although the 4d signal is noisy for 0.1 ML Pt coverage, it appears that the 4d binding energy (BE) for Pt_7 is shifted ~0.4 eV to higher energy compared to the Pt_8 BE. We previously reported XPS BEs for Pt_n on glassy

carbon[30] and indium tin oxide,[31] and Isomura *et al.*[10] reported BEs for $Pt_n/TiO_2(110)$. In all cases, the Pt_7 BE is higher than that for Pt_8, opposite to what might be expected if Pt_7 is more negatively charged than Pt_8. Note; however, that XPS BEs for small clusters are strongly affected by size-dependent final state effects,[1, 32-34] and size-dependent rehybridization of metal orbitals has recently been identified as another factor in BEs for supported Pd_n.[35, 36] As a result, interpreting the BE shift in terms of the initial state charge is not possible.

Upon ethylene binding, the calculated charge on the Pt binding site increases by ≈0.2–0.7 e, reflecting electron transfer from Pt to ethylene. Therefore, it is not unreasonable to expect that the more negatively charged cluster isomers and binding sites should tend to have higher ethylene binding energies. For example, the single-layer local minimum is 0.22 e^- more negatively charged than the prismatic global minimum, and its ethylene adsorption energy is stronger by 0.68 eV. Therefore, both the larger average alumina-to-Pt_n electron transfer for Pt_7, and the existence of low-lying single-layer local minima that have the highest alumina-to-Pt_n electron transfer, are consistent with the observation (Figure 2.1) that Pt_7 binds ethylene more strongly than Pt_8. The fact that Pt_7 also binds more ethylene in saturation is also consistent with the larger fraction of Pt in the cluster surface layer. At low coverage, the prismatic global minimum Pt_7 structure shows more di-σ ethylene binding (configurations ii and iv–vi, Figure 2.3, Table A.5) than the single-layer local minimum (only configuration iii). The di-σ bound ethylene often carries more negative total charge ($\Delta Q_{\text{ethylene}}$) as compared to its π-bound counterpart at all studied coverages (Table 2.1 and Tables A.5–A.7).

Because at the ethylene exposure temperature (150 K), the prismatic isomer of Pt_7

should dominate, and because of the great computational expense, coverage-dependent ethylene binding was studied only for starting geometries based on this isomer. All possible adsorption sites (atomic, bridging, and hollow) were evaluated for this global minimum Pt_7 isomer, and the six lowest energy geometries were used in further analysis. The lowest energy minimum for one ethylene adsorbed on prismatic Pt_7 was used as the starting geometry for adding the second ethylene, and the resulting two-ethylene minima were taken as starting geometries for adding the third. This is an approximation because the lowest energy geometry is not necessarily the precursor for higher coverage structures. Thus, there is some uncertainty as to whether the thermal populations in our coverage study include all important structures; however, the results provide at least qualitative insights.

With one or two ethylene molecules adsorbed, the prismatic Pt_7 starting geometry is retained in the optimized structures, but for three adsorbed ethylene molecules, optimization from many of the prismatic starting geometries led to single layer isomers, dominating the thermally accessible ensemble (>78% Boltzmann populations at 450 and 700 K). As noted, even for the first adsorbed ethylene, the single layer structure is lower in energy than the prismatic isomer, but the prismatic isomer is stabilized by a barrier of unknown height. The same is likely true for two ethylene molecules, but clearly, the isomerization barrier vanishes when the third ethylene binds. Therefore, one inference from DFT is that adsorption of ethylene will tend to drive transition toward single layer isomers and that such structures are therefore likely to be more important in the experiments than would be suggested by consideration of only adsorbate-free Pt_n geometries. Additionally, we observe that as ethylene coverage increases and cluster

geometries flatten, the populations of di-σ ethylene binding geometries, which are precursors to dehydrogenation, also increase from 7.35 to 84.26% at 450 K, i.e., at the peak of D_2 desorption (Table 2.1).

A coverage-dependent TPD/R experiment was performed on Pt_7/Al_2O_3 to gain further insight into the energetics and dynamics of ethylene desorption and the competition between desorption and dehydrogenation. Figure 2.4 compares C_2D_4 and D_2 desorption from separately prepared Pt_7/alumina samples exposed to 5, 0.1, and ~0.01 L of C_2D_4 at 150 K, otherwise following the same procedure as in Figure 2.2 For comparison, C_2D_4 desorption from the cluster-free alumina film is also shown for 5 and 0.1 L C_2D_4 exposures. Figure 2.4 also gives the numbers of C_2D_4 and D_2 molecules desorbing per Pt atom, calculated by subtracting the desorption from cluster-free alumina and then integrating.

For the Pt_7/alumina samples, C_2D_4 desorption clearly is mostly from sites on alumina at the lowest temperatures and from Pt-associated sites at temperatures above ~200 K. The Pt-associated desorption feature is quite broad, which normally would be taken as evidence for a wide distribution of desorption energies, as suggested by the fits to the TPD/R results discussed above. In that scenario, we would expect desorption to shift to higher temperatures for decreasing coverage, because in subsaturation coverages, adsorbates should tend to diffuse to and desorb from the most stable sites available. Furthermore, if C_2D_4 in the strongest di-σ binding sites has the highest probability of decomposing rather than desorbing intact, we might expect that the branching to D_2 should increase with decreasing coverage, as is observed from ~32% in the 5 L exposure to ~52% for the 0.01 L exposure.

The coverage dependence of the desorption temperatures do not fit this simple scenario, however. The C_2D_4 desorption spectrum is weakly coverage dependent, and if anything, there is less desorption at the highest temperatures for the lowest coverage. Furthermore, while the upper and lower temperature limits for D_2 desorption are independent of initial coverage, the peak of D_2 production shifts to substantially lower temperatures for lower initial C_2D_4 coverage. Given the DFT results showing that the relative stability of different Pt_7 isomers is dependent on C_2D_4 coverage and that the isomer distribution evolves with temperature, we believe that the measured desorption temperature distributions reflect complex dynamics involving changes in cluster structure as part of the C_2D_4 desorption and decomposition mechanism.

Figure 2.4 also illustrates the importance of substrate-mediated adsorption for highly dispersed clusters. Exposure of 5 L corresponds to 1.8×10^{15} C_2D_4 collisions/cm^2 or ~1.2 collisions/surface atom. If adsorption at Pt sites occurred only in C_2D_4 collisions on Pt_7, reducing the C_2D_4 exposure substantially should substantially reduce the C_2D_4 coverage on Pt_7. Assuming that adsorbed C_2D_4 either desorbs intact or generates two D_2 molecules, and subtracting the contribution from the alumina sites, the initial C_2D_4 coverage on Pt_7 in the 5 L dose is ~2.7 per Pt_7 cluster. For a dose 50 times lower, the coverage is ~2.1 C_2D_4/Pt_7, and for exposure 500 times lower, the initial coverage is still ~0.6 molecules/Pt_7.

2.3.3 Routes of Deactivation

From the perspective of the catalytic properties of small Pt_n/alumina, it is important to understand how the clusters are modified by heating, adsorption, desorption,

and dehydrogenation of ethylene. The DFT results suggest that isomerization is likely during the TPD/R cycle, and the second TPD/R runs on each sample (Figure 2.2) indicate that irreversible changes also occur. The amount of C_2D_4 desorbing at high temperatures decreased in the second run with an offsetting increase in desorption at low temperatures. The total amount of C_2D_4 desorbing in the second run was ~0.3 molecules per Pt atom for all three samples, which is essentially identical to the amount observed in the first runs for Pt_4 and Pt_8. For Pt_7; however, ~0.3 C_2D_4/Pt atom represents a ~25% drop compared to the first run. As shown above, C_2D_4 adsorbed on the alumina support all desorbs intact at low temperatures, and the results in the first and second TPD/R runs are identical for cluster-free alumina. For Pt_n/alumina, it is reasonable to assume that the alumina contribution to the C_2D_4 signal is also identical in the first and second runs, thus implying that C_2D_4 desorption from Pt sites shifted to lower temperatures in the second TPD/R run, i.e., the ethylene-Pt desorption energies substantially decreased. The temperature dependence for D_2 desorption did not differ dramatically between the first and second TPD/R runs; however, the integrated amount of D_2 dropped by ~60–70%. This behavior is what would be expected if the activation energy for C_2D_4 dehydrogenation is unchanged in the second run so that more of the C_2D_4, which is bound more weakly in the second run, desorbs at temperatures below the onset for decomposition.

In the second TPD/R run, the dependence on deposited cluster size is much weaker than that in the first, where Pt_7 stands out. This change could indicate that thermal or adsorbate-induced ripening or sintering generates a size distribution that no longer depends on the deposited size; however, there are other possibilities. DFT suggests that

the larger amount, stronger binding, and greater propensity toward dehydrogenation of C_2D_4 on Pt_7 compared to that on Pt_8 (based on its structural and electronic characteristics) is related to the existence of a larger number of strong di-σ binding sites on Pt_7. If carbon left on the surface by D_2 desorption in the first TPD/R run tends to poison the strong di-σ binding sites, this would reduce both the average C_2D_4 binding energy in the second TPD/R run, and the amount of D_2 produced, in line with observations. The fact that more D_2 is produced per Pt atom in the first TPD/R run for Pt_7 than either Pt_4 or Pt_8 implies additional carbon poisoning for Pt_7 in the second run, tending to bring its binding/reactivity properties more in line with those of Pt_4 and Pt_8.

Several experiments were done to provide additional insight into how TPD/R changes the clusters. CO binds strongly to Pt and weakly to alumina, providing an alternative probe of the effect of different experimental manipulations on the availability of Pt binding sites. Figure 2.5 compares CO TPD for a set of Pt_7/alumina/Ta(110) samples that were each first exposed to a particular manipulation and then probed by CO TPD (10 L ^{13}CO exposure at 150 K, heating at 3 K/sec to 700 K). Little CO desorbs from the alumina support, but for as-deposited Pt_7/alumina, strong bimodal CO desorption is observed with a low temperature component peaking at ~165 K and a broader high temperature component peaking at ~520 K. Simply heating Pt_7/alumina to 700 K in vacuum results in a ~40% decrease in high temperature CO desorption and an increase in low temperature desorption. We previously studied CO TPD from Pt_n/alumina/Re(0001) ($2 \leq n \leq 18$)[9] with similar results to the Pt_7/alumina/Ta(110) TPD shown here. We found that the high temperature CO desorption intensity during the first TPD on Pt_n/alumina/Re(0001) increased substantially with increasing cluster size. Therefore, we

can conclude that the decrease in high temperature CO desorption following 700 K heating in Figure 2.5 cannot be explained by thermal sintering or ripening alone. We are not claiming that sintering/ripening are unimportant, but there must be other changes as well. For example, 700 K annealing may cause changes in the as-deposited isomer distribution.

After a single C_2D_4 TPD/R run, there is a 55% decrease in the high temperature CO desorption, and the decrease is ~75% for CO TPD following 6 C_2D_4 TPD/R runs. Both heating and C_2D_4 TPD/R result in an increase in low temperature CO desorption, but overall, the total amount of CO desorbing decreased by ~25% after 700 K heating and ~40 and 50%, respectively, for 1 and 6 ethylene TPD/R runs. The larger effect of C_2D_4 TPD/R compared to that of 700 K heating is attributed to carbon left on the surface by D_2 desorption, blocking the Pt binding sites associated with high temperature CO desorption.

To provide additional insight into how ethylene binds to Pt_n/alumina and the effects of heating and carbon deposition, we did two types of He^+ ISS experiments. Figure 2.6 compares raw ISS data for Pt_7/alumina after a variety of experimental operations. The peaks primarily result from scattering of He^+ from single Pt, O, and Al atoms in the top layer of the sample. He^+ signal from multiple or subsurface scattering events is strongly attenuated, contributing mostly to the weak background at $E/E_0 \leq 0.6$.[37, 38] Small Pt clusters, where most or all of the Pt atoms are in the surface layer, should give large Pt ISS signals and also cause some attenuation of ISS signals from the alumina support, although the attenuation should be small because the Pt_n coverage is low. Isomerization or agglomeration of clusters to form multilayer structures reduces the

fraction of Pt in the surface layer, which should appear as a drop in Pt ISS signal. Similarly, adsorbates binding on top of the clusters attenuate the Pt ISS signal, while adsorbates binding on the alumina or around the cluster periphery have little effect on Pt signal but may attenuate signal from alumina.

In the top frame of Figure 2.6, ISS data are compared for the cluster-free alumina film, as-deposited Pt_7/alumina, and Pt_7/alumina that was heated to 700 K in ultrahigh vacuum (UHV). Note the presence of a small peak at $E/E_0 \approx 0.9$ for cluster-free alumina, attributed to a ~1% concentration of Ta in the surface layer from diffusion during high temperature alumina growth on the Ta(110) substrate.[39, 40] For samples with Pt_n deposited, this Ta signal is presumably still present, underlying the much stronger Pt peak. Because the Ta intensity is so small, we have not attempted to subtract it.

When as-deposited Pt_7/alumina is heated to 700 K, there is a small increase in Pt ISS intensity. As discussed above, TPD shows that the as-deposited clusters are decorated with ~0.5 adventitious CO molecules per cluster, and Figure A.6 implies that these CO molecules bind such that they attenuate ISS signal from the Pt clusters. Using the extrapolation procedure illustrated in Figure A.5 and detailed previously,[9, 41, 42] we estimate the attenuation to be ~30%, and the star in Figure 2.6 indicates the estimated value for adsorbate-free Pt_7/alumina. CO desorbs by 700 K (Figure 2.5), which should restore the Pt ISS intensity; thus, the fact that only a small signal increase occurs implies that heating also drives morphology changes that offset the expected increase. From the size of the offset, we can rule out formation of large three-dimensional particles, but thermal isomerization from single layer to prismatic isomers or modest ripening of the cluster size distribution are possible.

The lower frame of Figure 2.6 compares the effects of C_2D_4 exposure and TPD/R. One sample was exposed to 5 L of C_2D_4 at 150 K and then probed by ISS while cold, resulting in Pt ISS attenuation by ~90% compared to the adsorbate-free limit, demonstrating that C_2D_4 adsorbs in geometries that strongly attenuate He^+ signal from Pt. The Al and O ISS signals are attenuated by much smaller amounts, consistent with the TPD data, indicating that little C_2D_4 adsorbs on alumina at this temperature. ISS data are also shown for a Pt_7/alumina sample after a single C_2D_4 TPD/R run under the conditions of Figure 2.2 and for another sample run through 6 consecutive TPD/R runs prior to ISS analysis. After one TPD/R run, the Al and O intensities recover to the pre-exposure values, but the Pt ISS intensity remains ~15% below the as-deposited value or ~45% below the adsorbate-free limit. This post TPD/R value is ~25% smaller than that measured after 700 K heating, and this additional attenuation is not surprising given that we know that carbon is left on the surface by D_2 desorption (~1.4 C atoms/Pt_7). Figure A.7 gives the integrated D_2 desorption signal during 6 sequential C_2D_4 TPD/R runs, allowing us to estimate that a total of ~3.4 C atoms are left behind per initially deposited Pt_7. If this carbon remains on top of Pt, it would cause at least a substantial fraction of the ~65% Pt ISS attenuation observed after 6 TPD/R runs, but the attenuation may also reflects sintering or other changes in the Pt morphology. We also probed the residual carbon by XPS. No C 1s signal was detected after one or two TPD/R runs, but as shown in Figure A.8, after six runs, C 1s signal was observed, albeit too weak for accurate quantitation.

Temperature-dependent ISS (TD-ISS) provides more detailed information about the nature of the adsorbate binding on Pt_7. TD-ISS is essentially a C_2D_4 thermal

desorption experiment in which a Pt_7/alumina sample was dosed with 5 L of C_2D_4 at 150 K and then characterized by ISS. The sample temperature was then increased in 50 K steps, with ISS measurements at each step. Figure 2.7 plots the Pt ISS intensities, normalized to the sum of Al and O intensities, as a function of temperature (open circles). The top axis gives the cumulative He^+ exposure to the sample at the time the Pt ISS peak was being measured at each temperature. For comparison, the C_2D_4 and D_2 desorption data from Figure 2.2 are superimposed, and a horizontal solid line indicates the expected intensity for adsorbate-free Pt_7, estimated as shown in Figure A.6. Comparing the first point at 150 K to the value for adsorbate-free Pt_7/alumina, we see that 5 L C_2D_4 exposure at 150 K resulted in attenuation by ~93%, essentially the same attenuation seen in the raw ISS data in Figure 2.6. From TPD, we know that this initial exposure leads to adsorption of ~2.7 C_2D_4 molecules associated with the clusters with some additional C_2D_4 bound on the alumina. The expectation is that as the sample is heated and C_2D_4 desorbs or decomposes, the Pt ISS signal should recover.

To interpret the results quantitatively, it is necessary to understand how He^+ sputtering of Pt and C_2D_4 affects the Pt ISS signal. The extrapolation experiment (Figure A.5) also gives the decay rate of Pt ISS signal as a function of He^+ exposure, and this is plotted in Figure 2.6 as a gray dashed line labeled “Pt signal loss from sputtering”. For C_2D_4-covered Pt_7/alumina, He^+ sputter removal of C_2D_4 will tend to increase the Pt signal, and this rate was measured in an experiment where a sample was dosed with 5 L of C_2D_4 at 150 K and then repeatedly probed by ISS while held at 150 K (green dotted line labeled “Pt signal recovery by sputtering”). The Pt ISS intensity just after a single TPD/R cycle (Figure 2.7) is indicated on the right axis by a red star.

As shown by the superimposed TPD/R data, by 200 K, the lowest temperature C_2D_4 component has desorbed, but there is no recovery of Pt ISS signal beyond that expected from C_2D_4 sputtering. By 400 K, most of the C_2D_4 desorption and ~30% of D_2 desorption should have occurred, i.e., 85% of the initial C_2D_4 should have either desorbed or decomposed, but the Pt signal recovered to only ~30% of the adsorbate-free value. By 550 K, ~95% of the total amount of C_2D_4 and D_2 desorption should have occurred, but the Pt ISS signal was still ~35% below that expected for adsorbate-free Pt_7/alumina. Note that the intensity at this point is essentially identical to that observed immediately after a TPD/R experiment (red star). The Pt ISS intensity continued to increase and then leveled off above ~600 K at a value well above that seen after a TPD/R run (red star) but ~10% below the value that would be expected based on the "Pt signal loss from sputtering" trend line.

We interpret the results as follows. The TPD component below 200 K is associated with C_2D_4 bound on alumina (Figure 2.2); thus, its desorption is not expected to have any effect on the Pt ISS signal, as observed. By 300 K, ~50% of the initial C_2D_4 has desorbed, including a significant fraction of the Pt-associated C_2D_4, but there is only modest recovery of Pt signal, indicating the weakly bound C_2D_4 is in sites where it does not strongly attenuate Pt ISS signal. Only as the more strongly bound C_2D_4 desorbs or decomposes at higher temperatures does the Pt signal recovery accelerate, indicating that this strongest C_2D_4 binding component is in sites that are efficient at attenuating ISS from Pt_7. TPD/R shows that it is this strongly bound C_2D_4 that is most likely to decompose, generating D_2. Given our 45° angle of incidence and detection along the surface normal, we expect that these sites should be generally on top of the clusters. The fact that Pt ISS

recovery reaches only 90% of the adsorbate-free limit is not surprising because we know that carbon is left on the surface by D_2 desorption. Indeed, the substantially lower Pt ISS signal measured after a TPD/R run (red star) suggests that without the effect of He^+ sputtering throughout the TD-ISS run, even more decomposition products are left on the cluster surface.

During an earlier study of CO interactions with Pt_n/alumina/Re(0001), we measured but did not publish a TD-ISS study of CO binding for Pt_4/alumina/Re(0001), and this data is shown in Figure A.6 for comparison. The aspect that is relevant to the C_2D_4 results here is that the experiment shows that for CO, the strongest binding sites are also those which cause the largest Pt ISS attenuation, i.e., sites on top of the Pt clusters. A similar conclusion was reached in TD-ISS studies of CO on Pd_n/TiO_2[41] and Pd_n/alumina.

Finally, DFT was also used to examine carbon atom binding to Pt_7 and Pt_8 to determine the most stable binding geometries and also to see if the propensity for coking has a role in the observed efficiency of dehydrogenation on these clusters. Shaikhutdinov *et al*. noted that in alumina-supported Pd catalysts, carbon deposits began to form at ca. 550 K from di-σ bound ethylene.[24] As a first approach to understanding coking, we analyzed C-sticking energetics for isomers of deposited Pt clusters whose Boltzmann populations sum to >99% at 700 K. By summing the C-sticking energies for the Boltzmann-weighed populations for Pt_7 and Pt_8 (i.e., $\sum P\,E_C$), we obtain an estimate of the coking susceptibility of the isomer ensemble for each cluster size. Higher affinity to C should also correlate with a lower barrier to the dehydrogenation vs desorption.

Pure Pt clusters succumb to coking at higher temperatures due to the increasing population of isomers with very little resistance to carbon deposits (Figure 2.8). For Pt_7,

$\sum P\,E_C$ decreases with increasing temperature from −7.30 eV at 450 K to −7.38 eV at 700 K. For Pt_8, $\sum P\,E_C$ remains high at > −8.0 eV (see Table 2 for details). This suggests that Pt_8 should undergo coking more readily. The electrophilic C pulls electrons from the Pt clusters, resulting in a ΔQ_C of −0.40 to −0.56 eV (Figures A14 and A15). C preferentially adsorbs on a hollow site with 3–4 Pt–C bonds and prefers the more electron-rich isomers of Pt_7 (Figure 2.1, isomers II–IV) and Pt_8 (Figure 2.1, isomers I–IV). We note that catalyst deactivation is a complicated process that may involve the buildup of the C-rich deposits, cluster ripening, and more dramatic restructuring, and it is not fully captured by theory. Experimentally, it is clear that Pt_7 deactivates more strongly after the first TPD run.

2.4 Conclusions

We reported on ethylene dehydrogenation on size-selected, alumina-deposited subnano Pt clusters accessed via a combination of experiment and theory. Remarkably, deposited Pt_7 is found to be significantly more active than deposited Pt_8 and Pt_4, which in turn have comparable activities. Pt_7 also deactivates more easily through a number of potential ways, including coking and ripening. Throughout this study, we found that understanding many aspects of the experimental results requires consideration of the accessible ensemble of cluster isomers and how this evolves with C_2D_4 coverage and temperature. For example, the higher C_2D_4 binding affinity and dehydrogenation branching for Pt_7 compared to those of Pt_8 can be recovered only if multiple cluster minima are considered. Furthermore, the importance of single-layer geometries becomes obvious only after realistic coverage is included because C_2D_4 binding drives a transition

to single layer isomers where binding is stronger and more likely to result in dehydrogenation. From the dependence of ethylene activation by more negatively charged Pt atoms, it can be proposed that surfaces that charge Pt cluster more should be better supports for Pt catalysts for dehydrogenation. In addition, pronounced differential affinity for C binding is seen only in the ensemble. These results call for a change in paradigm when subnano cluster catalysts are characterized computationally, tracking isomer distributions with and without the adsorbate(s) of interest.

2.5 Methodology

2.5.1 Experimental Section

The experiments were performed using a cluster deposition/surface analysis instrument described previously,[41, 43] which allows in situ sample preparation and characterization. Briefly, the instrument consists of a laser vaporization cluster ion source that feeds into a mass-selecting ion deposition beamline that terminates in a UHV chamber (base pressure ~1.5×10^{-10} Torr). The main UHV chamber is equipped for sample cleaning and annealing and houses a differentially pumped mass spectrometer for TPD/TPR studies and hardware for sample characterization by XPS and low energy ISS.

The model catalyst supports were prepared alumina films grown on a 7 × 7 mm Ta(110) single crystal (Princeton Scientific Corporation), which was spot-welded to tantalum heating wires that were attached to a liquid-nitrogen cooled cryostat mounted at the end of a manipulator. The sample could be cooled to ~120 K and resistively heated to ~1200 K. A filament mounted directly behind the sample that allowed heating by electron bombardment to temperatures greater than 2100 K. Sample temperature was

monitored by a type C thermocouple spot-welded to the back side of the crystal. Because type C thermocouples have low output at temperatures below 300 K, the temperature scale was calibrated by temporarily attaching an additional type K thermocouple, with the result that the two thermocouples agreed to within 3 K over the 120–1000 K range where type K can be used.

Alumina thin films were grown using procedures adapted from work of the Goodman[44-46] and Madey[47, 48] groups. Aluminum was evaporated from a crucible mounted normal to the Ta(110) surface in 5×10^{-6} Torr $^{16}O_2$ background pressure while holding the sample temperature at 970 K. Film thicknesses were determined for each sample from the Al 2s and Ta 4d XPS intensities, and for these studies, the growth rate was maintained at ~2 Å/min. As discussed by Chen and Goodman, thin (~1.5 nm) alumina films grown on Ta(110) show slightly distorted hexagonal symmetry attributed to either the (0001) or (111) face of α-alumina.[49] We studied the effects of alumina thickness on the core and valence electronic properties of alumina grown on both Ta(110)[39] and Re(0001)[40] and on the CO oxidation activity of Pd_n clusters supported on alumina/Ta and alumina/Re. Because we found that properties became thickness-independent only above ~3 nm, we used 3–6 nm thick films in the present study. Note that all experiments were carried out on freshly prepared samples to avoid issues of sample contamination or damage.

Model catalyst preparation began by cooling the cryostat and sample holder until the surface temperature reached 130 K and then flashing it to ~2100 K for 5 min to remove any contaminants (including the previous alumina film) and annealing the crystal. XPS and ISS of the surface after this heat treatment showed no contamination with the

exception of submonolayer amounts of surface oxygen. The sample was then lowered into a small UHV-compatible antechamber, where it was isolated from the main chamber by a triple differentially pumped seal to the cryostat. The antechamber was then flooded with 5×10^{-6} Torr of O_2, and the alumina film was grown.

Following XPS characterization of the alumina film, the sample was flashed from ~120 to 800 K to desorb any adventitious adsorbates that might have adsorbed during XPS. To minimize exposure of the deposited clusters to background gases, deposition of mass-selected Pt_n (n = 4, 7, or 8) clusters was done as the sample cooled back to 120 K, beginning when the sample reached 300 K. During deposition, the sample was positioned directly behind a 2 mm in diameter exposure mask, which defined the size of the cluster spot on surface. The Pt_n coverage was monitored via the neutralization current of the soft landed (~1 eV/atom) clusters on the support, and deposition was terminated for all samples such that they all had identical Pt loading of 1.5×10^{14} atoms/cm^2 (~0.1 ML), differing only in the size of clusters deposited. Deposition took 5–15 min.

For TPD/R measurements, a differentially pumped mass spectrometer (UTI 100 C with Extrel electronics) was used, viewing the main chamber through the ~2.5 mm diameter aperture in the tip of a skimmer cone. The skimmer cone is surrounded by four 6 mm diameter dosing tubes that point at the sample position and can be connected to either continuous or pulsed valves. For dosing, the sample was positioned with the cluster spot centered on the skimmer aperture with a 2 mm separation to allow line of site from the dosing tubes to the cluster area. Calibration experiments show that the gas exposure to the cluster spot is ten times greater than the exposure to the chamber walls. For ethylene TPD/R experiments, the samples were exposed to 5 L of C_2D_4 at 150 K sample

temperature, chosen to minimize adsorption on the alumina support. The sample was then moved to 0.5 mm distance from the skimmer aperture, cooled to 135 K, and then ramped to 700 K at 3 K/sec while monitoring masses of interest desorbing from the surface. To examine the effects of heating and adsorbate exposure on the clusters, the TPD/R experiment (with fresh ethylene exposure) was repeated multiple times on each sample. Select experiments were done under identical conditions but with C_2D_4 exposures of 0.1 and 0.01 L.

Because CO binds strongly to Pt_n but not to alumina, we also did ^{13}CO TPD experiments to investigate the effects of heating and ethylene decomposition on the availability of Pt binding sites. These experiments were carried out by exposing samples to 10 L of $^{13}C^{16}O$ at 150 K and then ramping the temperature from 135 to 700 K at 3 K/sec while monitoring desorption of ^{13}CO and other masses of interest. Because of substrate-mediated adsorption,[38] highly dispersed Pt clusters are also efficient at collecting adventitious CO, present in the chamber background at $\sim 5 \times 10^{-11}$ Torr. After correcting the mass 28 TPD signal for C_2D_4 cracking in the ion source, the amount of CO adsorbed onto the clusters was found to be ~0.5 CO molecules per cluster for Pt_4, Pt_7, and Pt_8, i.e., approximately half of the clusters have one CO molecule adsorbed, desorbing above 500 K. This adventitious signal is independent of whether the sample was dosed with C_2D_4, i.e., C_2D_4 is not able to displace CO from the clusters. The amount of adventitious CO desorbing from a Pt-free alumina film sample is negligible.

To convert the ion signals measured during TPD/R to absolute numbers of molecules desorbing from the surface, we calibrated the mass spectrometer sensitivity in several ways.[9, 50] Several times during the course of the experiments, we checked the

calibration of C_2D_4 and other gases of interest by filling the main UHV chamber with those gases to a measured pressure (correcting for ionization gauge sensitivity) while measuring the resulting ion signals. This results in a well-known flux of molecules effusing through the 2.5 mm diameter skimmer cone aperture into the mass spectrometer ion source (creating a known number density), allowing us to calculate the calibration factor for each gas. To check for possible changes in electron multiplier gain, this calibration was done daily for argon gas. The accuracy of this calibration approach was checked against calibrations based on desorption of saturated CO layers of known coverage from Pd(111) or Ni(110).[41] We estimate that the calibration should be accurate to ±30%, mostly because of uncertainties in the angular distributions for desorption from clusters and the ionization efficiency vs angle.

Low energy ISS was used to observe the effects of cluster size, adsorbate binding, and TPD/R on the fraction of Pt atoms in the surface layer. ISS was done by loosely focusing a beam of 1 keV He^+ onto the sample at 45° angle of incidence with an energy of 1 keV onto the sample and measuring the energy of He^+ scattered along the surface normal. Peaks in the resulting energy spectrum are due to scattering of He^+ from single atoms in the sample surface layer, identifying the masses of those atoms. Multiple scattering or subsurface scattering events contribute to a broad background, which is weak due to low ion survival probability in such trajectories.[37] Because ISS is not a nondestructive technique, it was either done on separately prepared samples or on samples at the end of experimental sequences.

2.5.2 Computational

Because the alumina film used in the experiments is structurally similar to α-alumina(0001),[49] all calculations were done for this surface, and the calculations focused on Pt_7 and Pt_8 because these showed interesting differences in the experiments. Plane wave density functional theory calculations of both gas-phase and adsorbed Pt_7 and Pt_8 were performed using Vienna Ab initio Simulation Package (VASP)[51-54] with projector augmented wave potentials[55] and the PBE[56] functional. Bulk calculations were performed with a 8 × 8 × 3 Monkhorst–Pack k-point grid with large kinetic energy cutoffs of 520.0 eV and a stringent SCF (geometric) convergence criteria of 10^{-6} (10^{-5}) eV, resulting in an optimized lattice constant of a = 4.807 Å and c = 13.126 Å for α-Al_2O_3 (0001), a slight increase compared to experiment.[57, 58] This overestimation is typical of GGA functionals and corresponds to <0.1 Å increase in lattice constants. The α-alumina slab was modeled as a 3 × 3 unit cell with a vacuum gap of 15 Å and the bottom half of the slab kept fixed. For calculations presented in this paper, large kinetic energy cutoffs of 400.0 eV and convergence criteria of 10^{-5} (10^{-6}) eV for geometric (electronic) relaxations were employed. Only the most thermodynamically stable, Al-terminated surface was explored with an inward relaxation of 89.7% of the surface Al and O layers. Reproducing experimental results of −51 to −63% relaxation would require hydroxylation of the surface and introduce even more permutations of adsorbed cluster configurations.[59, 60] Thus, this is beyond the scope of the current study.

Adsorbed structures were formed from the deposition of the lowest 5–6 gas phase structures under PBE levels of theory *per manum* with a thorough sampling of cluster faces to possible binding sites. Gas phase structures of Pt_8 were found with the Adaptive

Force Field Coalescence Kick (AFFCK),[61] an adaptive global minimum and local minima search based on the Coalescence Kick (CK).[62] For Pt_7, structures from a study by Tian *et al*. were further optimized under VASP/PBE levels of theory, resulting in a new structure (isomer II in Figure A.9 and Tables A.1 and A.2).[63] A CK search also uncovered a new configuration, isomer III (see Figure A.9 and Table A.2). Note that the order of clusters composed of seven or more atoms will often be DFT method-dependent.[61] This is further discussed in detail in the Supporting Information, utilizing the TURBOMOLE V6.6 program with def2-TZVP basis and both pure (hybrid) versions of the functionals, PBE (PBE0) and TPSS (TPSSh), respectively.

The relevant equations regarding formation (E_{form}), adsorption (E_{ads}), and reagent (E_{reag}) energies may be found in Appendix A and follow the conventions presented in previous studies.[64, 65] Appendix A also includes the relevant equations utilized for statistical and bonding analysis such as the Boltzmann probability for *i*th configuration (P_i) and the Gibbs' entropy (S_G). S_G allows us to estimate at a specific temperature T the entropic contribution (TS_G) to the Helmholtz free energy ($F = U - TS_G$). To evaluate the ensemble effects of local minima at Pt_n, the summation of the Boltzmann-weighted adsorption energies ($\sum P_T E_{ads} = \sum_i P_{i,T} E_{i,ads}$) and carbon-sticking energies at a temperature T were calculated ($\sum P_T E_c = \sum_i P_{i,T} E_{i,c}$). For the coverage study of ethylene, the calculated adsorption of ethylene took on the forms:

$$\mathrm{E}_{1\ \mathrm{ethylene}} = \mathrm{E}_{1\ \mathrm{ethylene+Pt7ads}} - \mathrm{E}_{1\ \mathrm{ethylene,gas}} - \mathrm{E}_{\mathrm{Pt7ads}}$$

$$\mathrm{E}_{2\ \mathrm{ethylene}} = \mathrm{E}_{2\ \mathrm{ethylene+glob,Pt7ads}} - \mathrm{E}_{1\ \mathrm{ethylene+glob,Pt7ads}} - \mathrm{E}_{1\ \mathrm{ethylene,gas}}$$

$$\mathrm{E}_{3\ \mathrm{ethylene}} = \mathrm{E}_{3\ \mathrm{ethylene+glob,Pt7ads}} - \mathrm{E}_{2\ \mathrm{ethylene+glob,Pt7ads}} - \mathrm{E}_{1\ \mathrm{ethylene,gas}}.$$

Details of computational methods, isomers of gas phase and deposited clusters,

clusters with 1-3 adsorbed ethylene molecules, and C with charges, populations, energies, and other properties are given in Appendix A, Figures A9-A15, Tables A.1-A.7.

2.6 Acknowledgments

This work was supported by the Air Force Office of Scientific Research under a Basic Research Initiative grant (AFOSR FA9550-16-1-0141) to A.N.A. and S.L.A. M.-A.H. acknowledges the UCLA Department of Chemistry and Biochemistry Dissertation Year Fellowship. CPU resources at the DoD High Performance Computing Modernization Program (the United States Air Force Research Laboratory DoD Supercomputing Resource Center (AFRL DSRC), the United States Army Engineer Research and Development Center (ERDC), and the Navy DoD Supercomputing Resource Center (Navy DSRC)) supported by the Department of Defense, XSEDE, and the UCLA-IDRE cluster were used to conduct this work.

2.7 References

1. Kaden, W. E.; Wu, T.; Kunkel, W. A.; Anderson, S. L. *Science* **2009**, 326, 826–829

2. Vajda, S.; Pellin, M. J.; Greeley, J. P.; Marshall, C. L.; Curtiss, L. A.; Ballentine, G. A.; Elam, J. W.; Catillon-Mucherie, S.; Redfern, P. C.; Mehmood, F.; Zapol, P. *Nat. Mater*. **2009**, 8, 213– 216

3. Lee, S.; Molina, L. M.; Lopez, M. J.; Alonso, J. A.; Hammer, B.; Lee, B.; Seifert, S.; Winans, R. E.; Elam, J. W.; Pellin, M. J.; Vajda, S. Angew. *Chem., Int. Ed.* **2009**, 48, 1467– 1471

4. Kwon, G.; Ferguson, G. A.; Heard, C. J.; Tyo, E. C.; Yin, C.; DeBartolo, J.; Seifert, S.; Winans, R. E.; Kropf, A. J.; Greeley, J.; Johnston, R. L.; Curtiss, L. A.; Pellin, M. J.; Vajda, S. *ACS Nano* **2013**, 7, 5808– 5817

5. Campbell, C. T.; Campbell, J.; Dalton, P.; Henn, F.; Rodriguez, J.; Seimanides, S.

J. Phys. Chem. **1989**, 93, 806– 814

6. Pettiette-Hall, C. L.; Land, D. P.; McIver, R. T., Jr; Hemminger, J. C. *J. Am. Chem. Soc.* **1991**, 113, 2755– 2756

7. Hansen, T. W.; DeLaRiva, A. T.; Challa, S. R.; Datye, A. K. *Acc. Chem. Res.* **2013**, 46, 1720– 1730

8. Brizuela, G.; Hoffmann, R. *J. Phys. Chem. A* 1998, **102**, 9618– 9624

9. Roberts, F. S.; Kane, M. D.; Baxter, E. T.; Anderson, S. L. *Phys. Chem. Chem. Phys.* **2014**, 16, 26443– 26457

10. Isomura, N.; Wu, X.; Hirata, H.; Watanabe, Y. J. *Vac. Sci. Technol., A* **2010**, 28, 1141– 1144

11. Watanabe, Y.; Wu, X.; Hirata, H.; Isomura, *N. Catal. Sci. Technol.* **2011**, 1, 1490– 1495

12. Zhai, H.; Alexandrova, A. N. J. *Chem. Theory Comput.* **2016**, 12, 6213– 6226

13. Zhai, H.; Alexandrova, A. N. *ACS Catal.* **2017**, 7, 1905– 1911

14. Gao, M.; Lyalin, A.; Takagi, M.; Maeda, S.; Taketsugu, T. *J. Phys. Chem.* C **2015**, 119, 11120– 11130

15. Steininger, H.; Ibach, H.; Lehwald, *S. Surf. Sci.* **1982**, 117, 685– 698

16. Ibach, H.; Lehwald, S. J. *Vac. Sci. Technol.* **1978**, 15, 407– 415

17. Hatzikos, G.; Masel, *R. Surf. Sci.* **1987**, 185, 479– 494

18. Yagasaki, E.; Backman, A. L.; Masel, R. I. *Vacuum* **1990**, 41, 57– 59

19. Janssens, T. V. W.; Zaera, F. *Surf. Sci.* **1995**, 344, 77– 84

20. Kesmodel, L.; Dubois, L.; Somorjai, G. *Chem. Phys. Lett.* **1978**, 56, 267– 271

21. Starke, U.; Barbieri, A.; Materer, N.; Van Hove, M.; Somorjai, G. *Surf. Sci*. **1993**, 286, 1– 14

22. Neurock, M.; van Santen, R. A. *J. Phys. Chem. B* **2000**, 104, 11127– 11145

23. Anderson, A. B.; Choe, S. *J. Phys. Chem.* **1989**, 93, 6145– 6149

24. Shaikhutdinov, S. K.; Frank, M.; Bäumer, M.; Jackson, S. D.; Oldman, R. J.;

Hemminger, J. C.; Freund, H.-J. *Catal. Lett.* **2002**, 80, 115– 122

25. Mohsin, S. B.; Trenary, M.; Robota, H. J. *J. Phys. Chem.* **1988**, 92, 5229– 5233

26. Perry, D. A.; Hemminger, J. C. *J. Am. Chem. Soc.* **2000**, 122, 8079– 8080

27. Carlsson, A.; Madix, R. *J. Chem. Phys.* **2001**, 115, 8074– 8082

28. Paz-Borbón, L. O.; Hellman, A.; Thomas, J. M.; Grönbeck, H. *Phys. Chem. Chem. Phys.* **2013**, 15, 9694– 9700

29. Stöhr, J.; Sette, F.; Johnson, A. L. *Phys. Rev. Lett.* **1984**, 53, 1684

30. Proch, S.; Wirth, M.; White, H. S.; Anderson, S. L. *J. Am. Chem. Soc.* **2013**, 135, 3073– 3086

31. von Weber, A.; Baxter, E. T.; Proch, S.; Kane, M. D.; Rosenfelder, M.; White, H. S.; Anderson, S. L. *Phys. Chem. Chem. Phys.* **2015**, 17, 17601– 17610

32. Chusuei, C. C.; Lai, X.; Luo, K.; Goodman, D. W. *Top. Catal.* **2000**, 14, 71– 83

33. Bagus, P. Chemical information from XPS binding energy shifts: A unified view. *Abstracts of Papers of the American Chemical Society*; American Chemical Society: Washington, DC, March 23–27, 2003; pp U676– U677.

34. Dai, Y.; Gorey, T. J.; Anderson, S. L.; Lee, S.; Lee, S.; Seifert, S.; Winans, R. E. *J. Phys. Chem. C* **2017**, 121, 361– 374

35. Kaden, W. E.; Büchner, C.; Lichtenstein, L.; Stuckenholz, S.; Ringleb, F.; Heyde, M.; Sterrer, M.; Freund, H.-J.; Giordano, L.; Pacchioni, G.; Nelin, C. J.; Bagus, P. S. Phys. Rev. B: Condens. *Matter Mater. Phys.* **2014**, 89 (115436) 115431– 115438

36. Roberts, F. S.; Anderson, S. L.; Reber, A. C.; Khanna, S. N. *J. Phys. Chem. C* **2015**, 119, 6033– 6046

37. Rabalais, J. W. *Principles and applications of ion scattering spectrometry: surface chemical and structural analysis*; Wiley: New York, 2003; p 336.

38. Aizawa, M.; Lee, S.; Anderson, S. L. *Surf. Sci.* **2003**, 542, 253– 275

39. Kane, M. D.; Roberts, F. S.; Anderson, S. L. *Faraday Discuss*. **2013**, 162, 323– 340

40. Kane, M. D.; Roberts, F. S.; Anderson, S. L. *J. Phys. Chem. C* **2015**, 119, 1359– 1375

41. Kaden, W. E.; Kunkel, W. A.; Roberts, F. S.; Kane, M.; Anderson, S. L. *J. Chem. Phys.* **2012**, 136, 204701– 204712

42. Kaden, W. E.; Kunkel, W. A.; Anderson, S. L. *J. Chem. Phys*. **2009**, 131 (114701) 114701– 114715

43. Kane, M. D.; Roberts, F. S.; Anderson, S. L. *Int. J. Mass Spectrom.* **2014**, 370, 1– 15

44. Chen, P. J.; Goodman, D. W. *Surf. Sci.* **1994**, 312, L767– L773

45. Street, S. C.; Goodman, D. W. *Chem. Phys. Solid Surf.* **1997**, 8, 375– 406

46. Lai, X.; Chusuei, C. C.; Luo, K.; Guo, Q.; Goodman, D. W. *Chem. Phys. Lett*. **2000**, 330, 226– 230

47. Wu, Y.; Garfunkel, E.; Madey, T. E. *J. Vac. Sci. Technol., A* **1996**, 14, 2554– 2563

48. Wu, Y.; Garfunkel, E.; Madey, T. E. *Surf. Sci.* **1996**, 365, 337– 352

49. Chen, M. S.; Goodman, D. W. J. Phys.: *Condens. Matter* **2008**, 20, 264013

50. Kane, M. D.; Roberts, F. S.; Anderson, S. L. *Int. J. Mass Spectrom.* **2014**, 370, 1– 15

51. Kresse, G.; Furthmüller, *J. Comput. Mater. Sci.* **1996**, 6, 15– 50

52. Kresse, G.; Furthmüller, *J. Phys. Rev. B: Condens. Matter Mater. Phys*. **1996**, 54, 11169

53. Kresse, G.; Hafner, *J. Phys. Rev. B: Condens. Matter Mater. Phys.* **1993**, 47, 558

54. Kresse, G.; Hafner, *J. Phys. Rev. B: Condens. Matter Mater. Phys.* **1994**, 49, 14251

55. Kresse, G.; Joubert, D. *Phys. Rev. B: Condens. Matter Mater. Phys.* **1999**, 59, 1758

56. Perdew, J. P.; Burke, K.; Ernzerhof, M. *Phys. Rev. Lett.* **1996**, 77, 3865

57. Bourdillon, A.; El-Mashri, S.; Forty, *A. Philos. Mag. A* **1984**, 49, 341– 352

58. Levin, I.; Brandon, D. *J. Am. Ceram. Soc.* **1998**, 81, 1995– 2012

59. Ahn, J.; Rabalais, *J. Surf. Sci.* **1997**, 388, 121– 131

60. Wang, X.-G.; Chaka, A.; Scheffler, M. *Phys. Rev. Lett.* **2000**, 84, 3650

61. Zhai, H.; Ha, M.-A.; Alexandrova, A. N. *J. Chem. Theory Comput.* **2015**, 11, 2385– 2393

62. Averkiev, B. Geometry and electronic structure of doped clusters via the Coalescence Kick method. Ph.D. Thesis, Utah State University, December 2009.

63. Tian, W. Q.; Ge, M.; Sahu, B.; Wang, D.; Yamada, T.; Mashiko, S. *J. Phys. Chem. A* **2004**, 108, 3806– 3812

64. Dadras, J.; Jimenez-Izal, E.; Alexandrova, A. N. *ACS Catal.* **2015**, 5, 5719– 5727

65. Ha, M.-A.; Dadras, J.; Alexandrova, A. *ACS Catal.* **2014**, 4, 3570– 3580

Table 2.1: Boltzmann populations of adsorbed ethylene of n = 1..3 coverage in the di-σ, sp^3 configuration (precursor to dehydrogenation)

Ethylene Coverage	n = 1	n = 2	n = 3
$E_{n\ ethylene,glob}$ (eV)	-1.29	-1.62	-1.73
$\Delta Q_{ethylene,glob}$ (e)	0.00	-0.02	-0.30
$\Sigma P_{450K,sp3}$	7.35%	17.51%	84.26%
$\Sigma P_{700K,sp3}$	14.93%	29.42%	69.22%

Table 2.2: Adsorbed isomers with C

Cluster	**Isomer**	**E_C (eV)**	**ΣP_{450K} E_C (eV)**	**ΣP_{700K} E_C (eV)**
Pt_7-C	I	-7.05	-7.30	-7.38
	II	-8.03		
	III	-7.70		
	IV	-7.61		
Pt_8-C	I	-8.17	-8.16	-8.12
	II	-7.60		
	III	-8.36		
	IV	-7.90		
	V	-7.27		

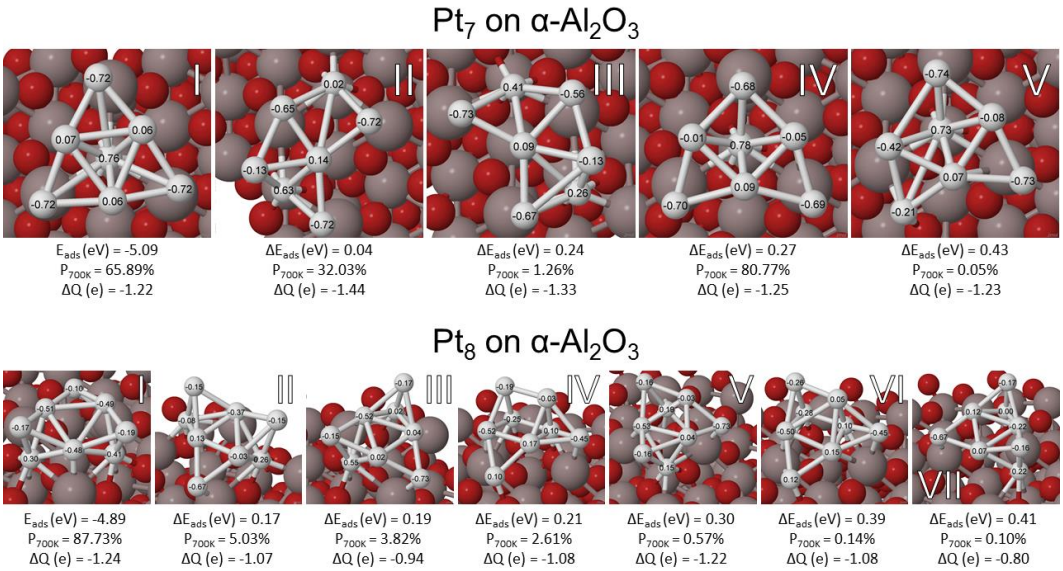

Figure 2.1: The lowest-energy minima of adsorbed Pt_7 and Pt_8, with adsorption energies (E_{ads}), Boltzmann population at catalytic temperature of 700 K (P_{700K}), and charge transfer from the support to the cluster (ΔQ).

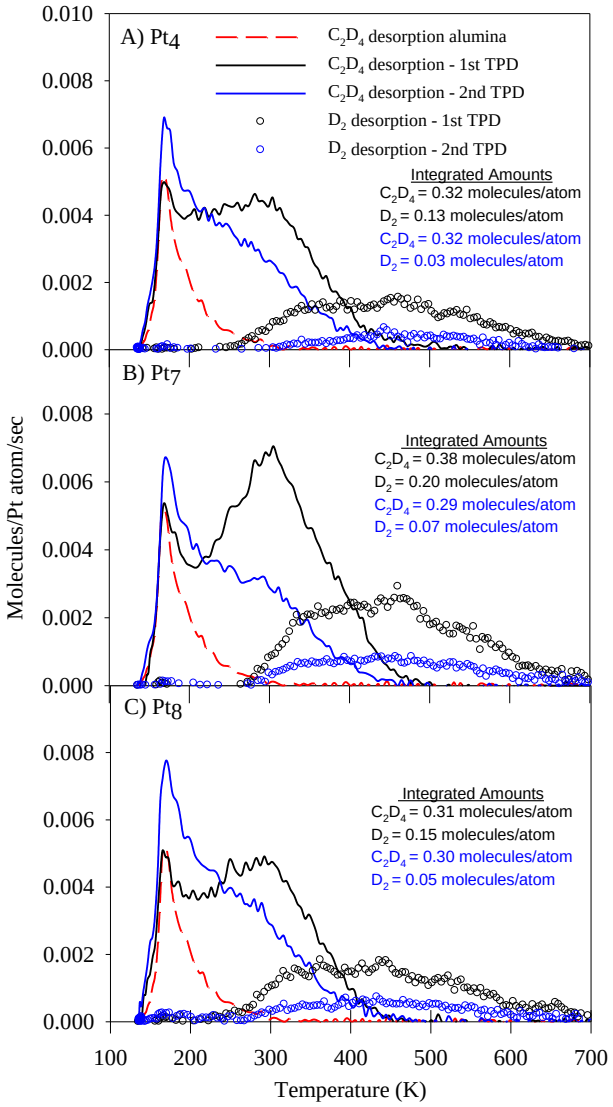

Figure 2.2: Desorption of unreacted C_2D_4 (solid) and D_2 products (circles) during the 1st and 2nd consecutive TPR runs. Each TPR measurement was made after a 5 L C_2D_4 exposure to Pt_n/alumina (n = 4, 7, or 8) at 150 K. The dashed red line shows desorption of unreacted C_2D_4 from the cluster-free alumina support and is scaled as if the sample contained an identical Pt loading as the Pt_n/alumina samples. Each set of spectra results from individual experiments. Included in each frame is the total integrated desorption of C_2D_4 and D_2 per Pt atom for each experiment.

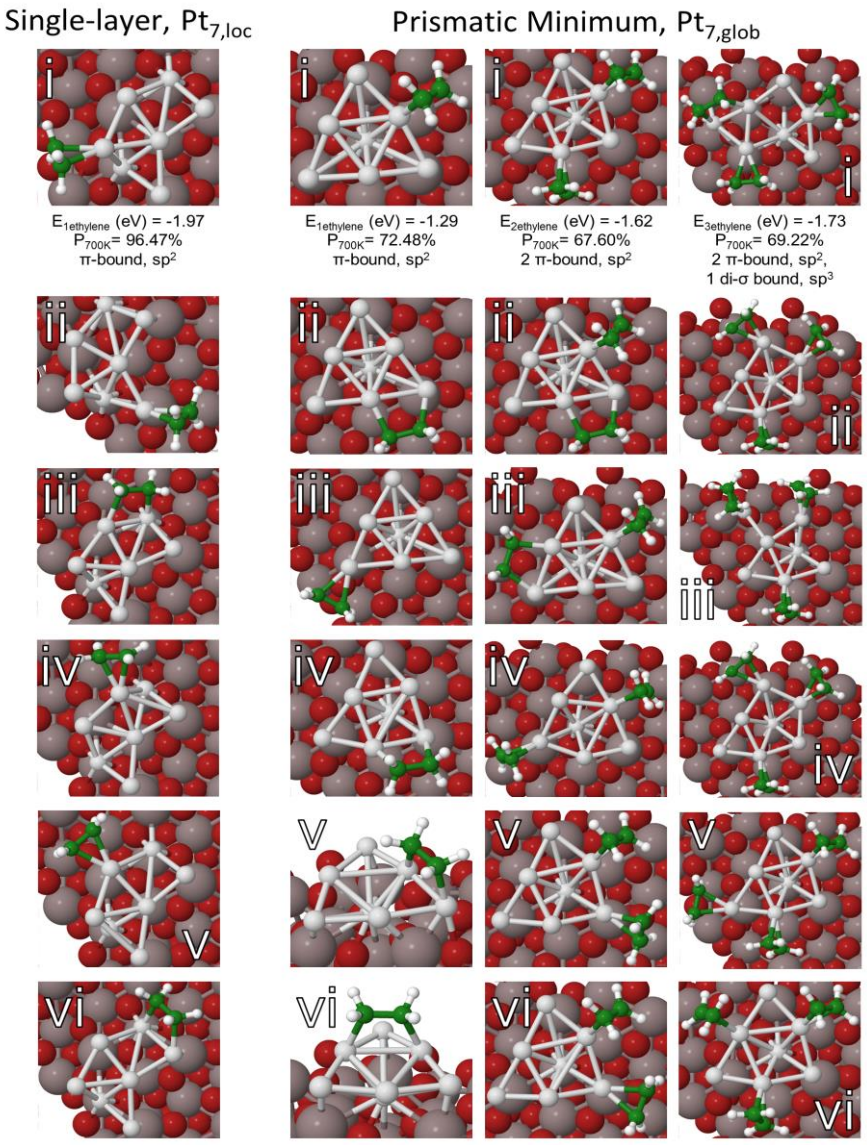

Figure 2.3: Structures of ethylene binding to Pt_7. Left column: Binding of a single ethylene molecule to different sites on single-layer Pt_7. Columns 2 – 4: Binding of 1, 2, or 3 ethylene molecules in different sites on the global minimum prismatic isomer of Pt_7. Energetics and bonding analysis are summarized in Table A.5 and adsorption geometries and thermal distributions are summarized in Table 2.2 For additional local minima at each coverage (n = 2, 3), refer to Appendix A.

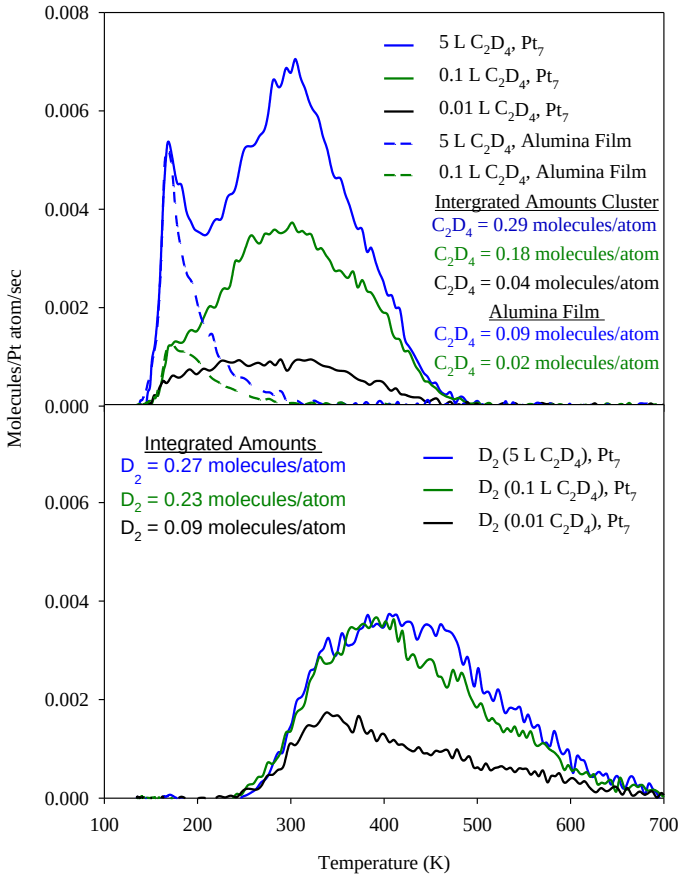

Figure 2.4: Desorption of unreacted C_2D_4 (top frame) and D_2 products (bottom frame) during TPR after 150 K C_2D_4 exposure to Pt_7/alumina and the cluster-free alumina support. Desorption of C_2D_4 from the cluster-free alumina support was scaled as if the sample contained an identical Pt loading as the Pt_7/alumina samples. Each set of spectra results from individual experiments with either a 5, 0.1, or 0.01 L C_2D_4 exposure. Each frame also includes the total integrated C_2D_4 and D_2 desorption per Pt atom for each experiment.

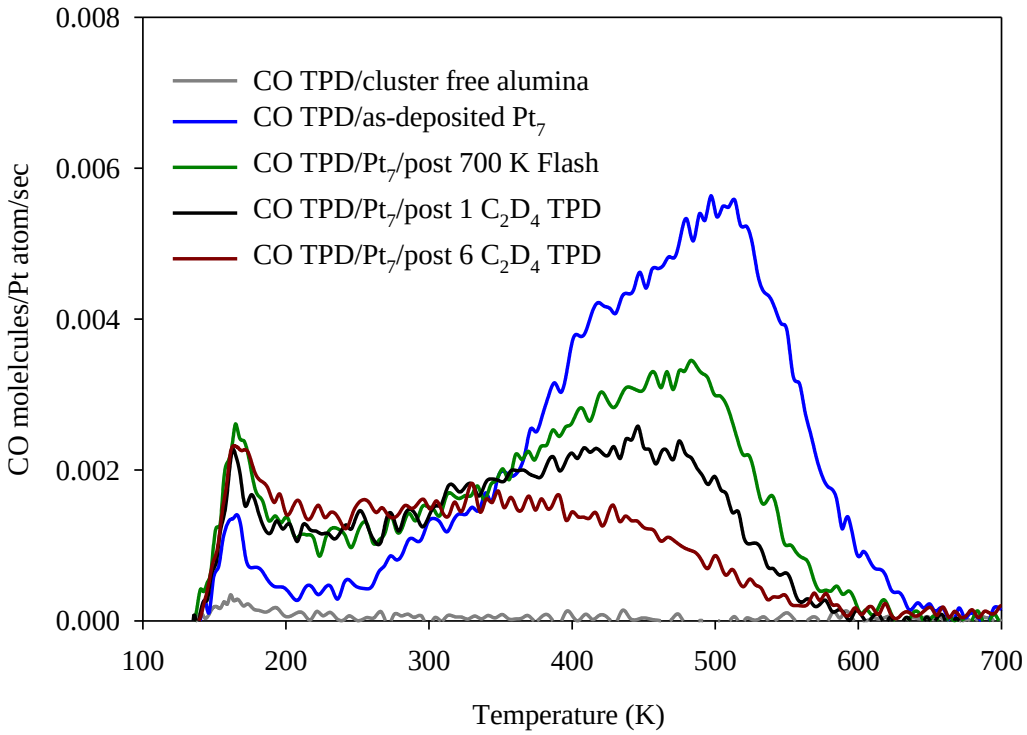

Figure 2.5: CO desorption from a Pt_7/alumina compared with CO desorption from separately prepared Pt_7/alumina samples after a 700 K flash, a single C_2D_4 TPD, and 6 consecutive TPD's. All samples were exposed to 10 L of CO at 150 K.

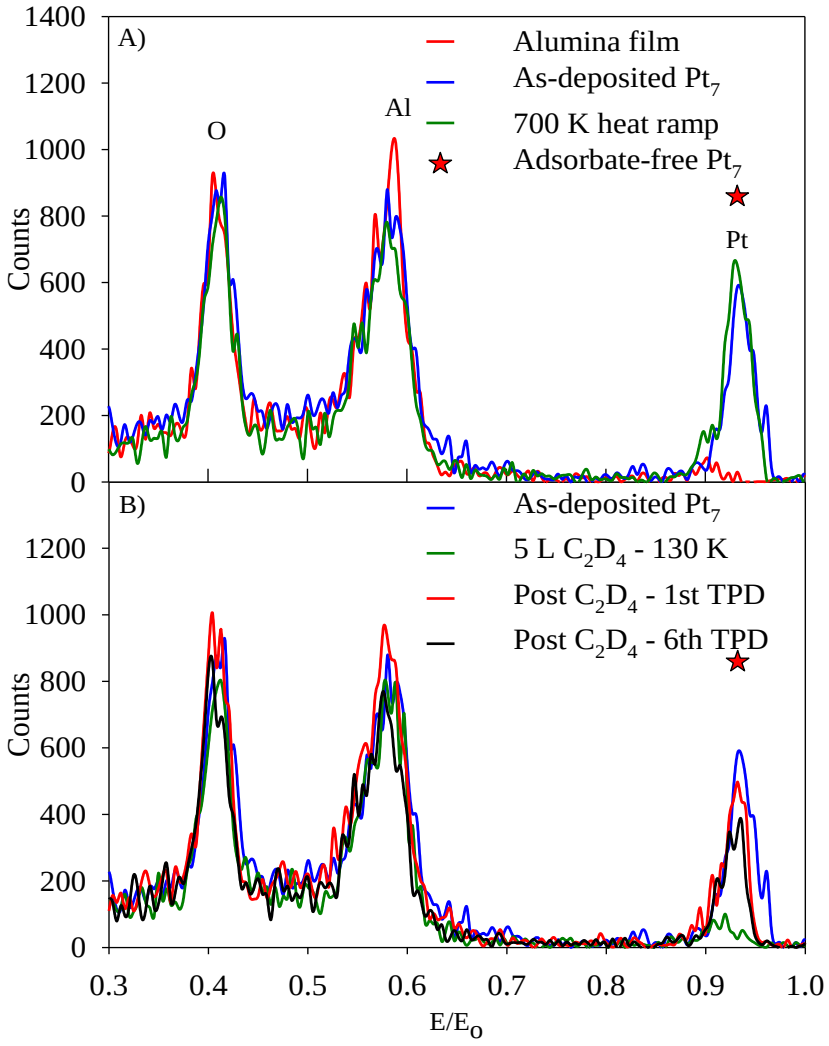

Figure 2.6: Raw ISS spectra for Pt_7/alumina samples (a) after a 700 K flash and measured as-deposited. Extrapolated as-deposited is represented by the star. (b) Raw ISS spectra Pt_7/alumina sample after the sample was exposed to 5 L of C_2D_4 at a 150 K and cooled to 130 K, after one C_2D_4 TPD, and after six consecutive C_2D_4 TPDs.

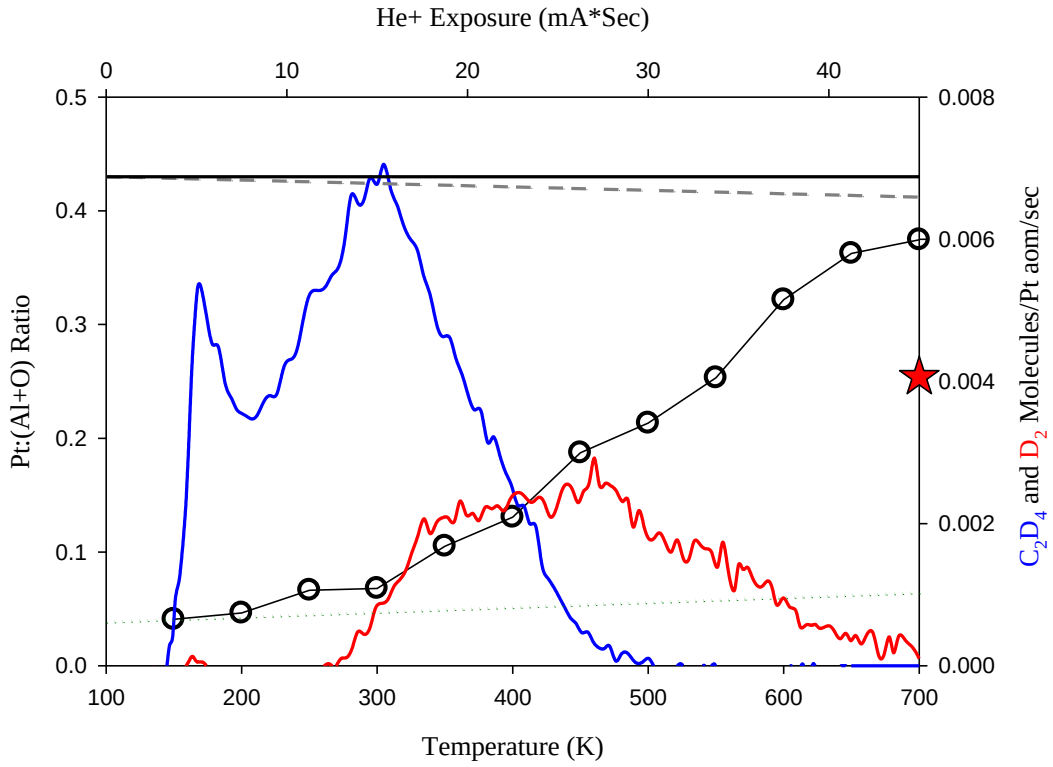

Figure 2.7: Pt/(Al + O) ISS intensity ratios for Pt_7/alumina after exposure to 5 L of C_2D_4 at 150 K and during a sequence where the sample was heated to the indicated temperatures (black circles). The as-deposited Pt intensity and calibrated rates of Pt recovery from C_2D_4 sputtering and for loss of Pt signal due to sputtering are represented by dashed lines. The Pt/(Al + O) intensity ratio (red star) was measured after completion of a single ethylene TPD cycle.

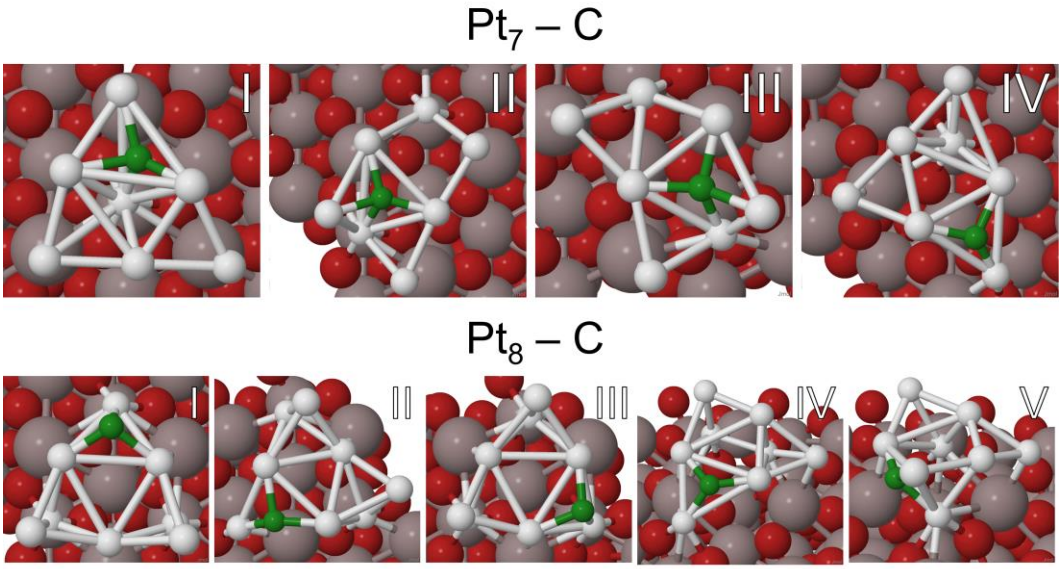

Figure 2.8: First-order approximation of coking on Pt_7 and Pt_8: lowest-energy structures for a single C atom adsorbed on these clusters.

CHAPTER 3

BORON SWITCH FOR SELECTIVITY OF CATALYTIC DEHYDROGENATION ON SIZE-SELECTED Pt CLUSTERS ON Al_2O_3

3.1 Overview

Size-selected supported clusters of transition metals can be remarkable and highly tunable catalysts. A particular example is Pt clusters deposited on alumina, which have been shown to dehydrogenate hydrocarbons in a size-specific manner. Pt_7, of the three sizes studied, is the most active and, therefore, like many other catalysts, deactivates by coking during reactions in hydrocarbon-rich environments. Using a combination of experiment and theory, we show that nanoalloying Pt_7 with boron modifies the alkene-binding affinity to reduce coking. From a fundamental perspective, the comparison of experimental and theoretical results shows the importance of considering not simply the most stable cluster isomer, but rather the ensemble of accessible structures as it changes in response to temperature and reagent coverage.

3.2 Introduction

In the subnano-regime of cluster catalysis, size-selected surface-supported clusters often exhibit nonmonotonic trends in reactivity and selectivity, inspiring the hunt for cluster sizes that are particularly active, selective, and resistant to deactivation.[1-4] Not only can they exhibit special catalytic properties due to size effects on electronic and geometric structure, but also most or all of the atoms in sub-nanoclusters are available to bind reactants, making them a promising and rising class of catalysts. In addition, size-selected clusters provide a theoretically tractable approach to testing strategies for catalyst improvement. We recently showed that Pt_7 deposited on alumina both binds and dehydrogenates ethylene more efficiently than Pt_4 or Pt_8 on either a per cluster or a per Pt atom basis. This higher activity was shown to result from the diverse cluster

morphologies accessible to Pt_7, particularly at higher temperatures and reagent coverages.[1] However, this finding is bittersweet, because these clusters and especially the most active Pt_7 easily deactivate via a combination of coke (i.e., carbon) deposition and sintering. Coke formation deactivates many catalysts in reactions such as Fischer–Tropsch synthesis,[5] cracking of hydrocarbons,[6] and alkene dehydrogenation.[7] Sintering, that is, cluster migration, ripening, and agglomeration into larger nanoparticles, where fewer atoms are available on the surface, is another major route of activity loss.[8] Thus, improved cluster catalysts would sustain the activity and selectivity of the highly promising Pt_n, while resisting coking and sintering.

In this work, we test the strategy of nanoalloying to tune the selectivity for dehydrogenation by Pt_n/Al_2O_3, focusing on Pt_7, with the goal of minimizing deactivation by coking and sintering. Doping and alloying can be used to tune the properties of bulk Pt. Alloying Pt with Sn[9] and Zn[10, 11] has been used for selectivity control and with Pd to reduce sintering.[12, 13] Here, our inspiration is drawn from the boration (boron-doping) of extended surfaces of Co and Ni, used in Fischer–Tropsch synthesis and steam methane reforming, respectively.[14, 15] Boration of these metal surfaces extended the lifetime of the catalyst by preventing coke adsorption. In general, boron interacting with metals can lead to a variety of interesting phenomena, such as alloy ultrahardening,[16] emergence of topological and Kondo insulators,[17] exotic magnetism,[18] surface reconstructions,[19] record coordination chemistry,[20] and the selectivity of Pd catalysts in hydrogenation.[21, 22] Recently, we began to theoretically probe boron as a dopant for small Pt clusters deposited on magnesia,[23] and found it to reduce affinities of these systems to carbon atoms. Building from this promising initial result, we now address the effect of boration

on the selectivity of catalytic dehydrogenation and coking sensitivity of Pt_7 on alumina, using both ab initio and statistical mechanical theory, in conjunction with experiment. In what follows, we show that nanoalloying with boron dramatically changes the properties toward alkene binding and dehydrogenation.

3.3 Results and Discussion

Size-selected $Pt_{4,7,8}$ on alumina have been prepared as discussed in detail previously,[1, 24] and then borated by exposure to diborane (B_2H_6). Boration and its effects on binding and dehydrogenation of a model alkene, ethylene, were probed by temperature-programmed desorption/reaction (TPD/R), low energy ion scattering (ISS), plane wave density-functional theory (PW-DFT) calculations, and molecular dynamics (MD) simulations. Initial studies suggested that Pt_7 is not only the most active, but also the most susceptible to the effect of boration. We therefore focused our experimental and theoretical work on Pt_7 and will explore size effects in future studies.

We find that diborane adsorbs dissociatively on the Pt_7 clusters, undergoing both B–H and B–B bond scission, and leaving atoms of boron in the clusters, as it has been reported to do also on the surfaces of Ni,[25] Pd,[26] Ru,[27] Fe or steel,[28] Al_2O_3,[29] and Pt/Al_2O_3.[30] Pt^0 complexes are also well-known for the successful formation of unique boronated complexes containing borenes, boranes, and borylanes.[31, 32] Notably, Söderlund *et al*. observed the formation of BH_3, B_3H_7, B_3H_9, B_5H_9, and B_6H_{10} in fixed bed reactor studies of diborane on Pt/Al_2O_3, and it is likely that this also occurs in our experiments.[30] ISS of as-deposited Pt_7/alumina (Figure 3.1a) shows peaks for O, Al, and Pt. B, itself, is undetectable due to a combination of low ISS sensitivity for B, low B

coverage, and high background at low E/E_0. Nonetheless, because adsorbates attenuate ISS signal from underlying atoms, the presence of diborane and fragments thereof can be inferred by the effects on other signals.

Considering the Pt signal as reported previously,[1] efficient substrate-mediated adsorption of background CO ($\sim 5 \times 10^{-11}$ mbar) leaves ~0.5 CO molecules adsorbed per cluster, on average, and by extrapolation we estimate that the as-deposited Pt signal is ~30% below the adsorbate-free limit (indicated by a ★). Only a small recovery of Pt ISS signal is seen after 700 K heating to desorb adventitious CO, indicating that heating also causes structural changes that result in a smaller fraction of Pt in the surface layer.[1] Initial exposure of a Pt_7/alumina sample to 1.5 L of B_2H_6 at 130 K results in ~80% attenuation of the Pt ISS signal (Figure 3.1a), demonstrating that diborane binds efficiently on top of Pt_7.[1, 24] Note that 1.5 L exposure may lead to adsorption of more than one diborane per cluster. Because of computational limits, only adsorption of a single diborane adsorbed to Pt_7 clusters was pursued (Figure 3.1b).

PW-DFT calculations were performed to probe adsorption of a single diborane on Pt_7 isomers. In these 0 K and *in vacuo* calculations, binding of diborane on the prismatic global minimum of Pt_7 results in B–H bond scission with some hydrogen leaving for Pt sites; on the more catalytically active[1] single layer isomer, the B–B bond also breaks with diborane spontaneously decomposing to form BH_y fragments. These results are consistent with the large Pt ISS attenuation observed. The Al and O ISS peaks in ISS underwent only a small attenuation upon diborane exposure at 130 K, indicating that only a small amount of diborane binds to alumina at 130 K, possibly at defects, and the Al and O peaks largely recover when the sample is heated to 300 K, indicating that most of this

initial coverage desorbs at low temperatures.

In the sample heated to 300 K, the Pt signal recovered to ~50% of the as-deposited value, indicating some desorption of diborane or its fragments, but with a significant B_xH_y coverage remaining, attenuating ISS signal from underlying Pt. After heating to 700 K, the Pt signal recovered to the as-deposited value, but was still ~30% below the expected adsorbate-free limit, and also below the signal observed after heating without diborane exposure.

CO TPD (Figure 3.2) probed the number and energetics of exposed Pt sites. For CO on as-deposited Pt_7, the main desorption peak is between 300 and 600 K, with a small peak below 200 K. If as-deposited Pt_7 is first simply heated to 700 K in UHV, the total amount of CO desorbing from Pt sites is reduced by ~10%, but the temperature dependence is essentially unchanged. A similar effect is observed if the Pt_7/alumina is exposed to a saturation dose of D_2 and then heated to 700 K (not shown), consistent with the ISS suggesting thermal restructuring causing a small reduction in the number of exposed Pt sites.

Sintering/agglomeration of the Pt_7 into larger clusters, with fewer exposed Pt sites, could potentially account for this small decrease in CO desorption; however, a previous study of CO TPD from Pt_n/alumina/Re(0001) ($2 \leq n \leq 18$)[24] found that this CO desorption feature increased significantly with increasing cluster size. Therefore, we conclude that the observed decrease in high-temperature CO desorption after heating cannot be explained by sintering/agglomeration alone. As discussed previously,[1] theory suggests that the ensemble of Pt_7/isomers favors more prismatic isomers that would also provide fewer CO binding sites.

In any case, it is clear that boration has a much larger effect. For Pt_7 first exposed to 1.5 L of B_2H_6 and heated to 300 K, the CO desorption is attenuated by ~40%, and the main CO desorption peak shifts ~100 K, demonstrating that boration significantly weakens the Pt–CO binding. B_2H_6 exposure followed by 700 K heating has little additional effect on either the number or the energetics of CO binding sites, despite the observation that 700 K heating results in recovery of the Pt ISS signal to the as-deposited value. The recovery of Pt ISS signal to the as-deposited value following the 700 K heating is further evidence that the observed changes in the CO binding are not a result of thermal sintering.

DFT calculations show that diborane adsorbs dissociatively atop the clusters as fragments of H, B_xH_y, or BH_y (Figure 3.1b), consistent with the low Pt ISS intensity observed after diborane exposure. However, the majority of Pt_7B/Al_2O_3 structures accessible at 700 K feature the boron acting as a $B–O_{surf}$ anchor between the cluster and the support ($R(B–O_{surf}) \approx 1.4$ Å, isomers I–IV, VII, VIII) with some structures displaying flatter, single-layer geometries with highly coordinated Pt–B bonds (isomers V–VI, IX, X, Figure 3.1b). All of these structures expose a large fraction of Pt atoms in the surface layer, accounting for high Pt ISS intensity. Pt atoms bonded to B and reduced charge transfer from the support, presumably account for the weakened CO binding. The decomposition of diborane may undergo many pathways,[33-35] and a future study will elucidate the complex interactions between the borating agent and size-selected clusters.

In our study of nonborated Pt_n/alumina,[1] it was shown that the experimental results were consistent with the theoretical finding of cluster size-dependent ensembles of thermally accessible structures. Predicted evolution of the ensembles with respect to both

temperature and ethylene binding was essential to interpreting the ISS and ethylene adsorption results. Because of the increase in complexity of the borated system, such detailed experiment–theory comparison is not feasible; however, theory indicates, perhaps not surprisingly, that Pt_7B/alumina has an even more complex ensemble than Pt_7/alumina.

In Pt_7B, 10 distinct isomers contribute significantly to the ensemble at 700 K, with the global minimum constituting only 59% of the population. For comparison, the global minimum of Pt_7 on alumina comprised 66% of the ensemble and for the less active Pt_8, 88%.[1] Thus, the structural diversity unique to Pt_7/alumina[1] leading to a manifold of binding sites is enhanced in the Pt_7B/alumina ensemble. Having access to diverse isomers introduces the possibility of at least one of them being dominant in catalysis, making the entire ensemble more active, although in more complicated reactions diversity can have an adverse effect on selectivity. At the same time, Pt_7B's diversity results in a substantial increase in the configurational entropy's contribution to the free energy of the system (Appendix B, Tables B.3 and B.4).[12] These observations are valid only if all thermodynamically accessible isomers are also kinetically accessible.

The effects of boration on ethylene binding and dehydrogenation on Pt_7 were also probed by TPD/R. Figure 3.3b compares the temperature dependence for C_2D_4 and D_2 desorption from separate Pt_7/alumina samples, studied as-deposited and after heating to 300 or 700 K, with and without prior 130 K 1.5 L diborane exposure. For as-deposited Pt_7/alumina, unreacted ethylene desorbs in two components. The low-temperature component is identical to that seen for Pt-free alumina and is attributed to ethylene bound to the alumina support. Desorption from Pt_7 sites occurs in a broad component from

~200 to 500 K. D_2 desorption (dehydrogenation) is not observed for alumina, but appears between ~300 and 650 K for as-deposited Pt_7/alumina. We previously showed that the onset temperature for D_2 desorption is determined by the activation energy for C_2D_4 dehydrogenation rather than for D_2 desorption.[1] Integrating the desorption signal allows us to estimate the number of C_2D_4 and D_2 molecules desorbing, which, after subtraction of C_2D_4 desorption from alumina, amounts to ~2.1 C_2D_4 and ~1.5 D_2 molecules per Pt_7 cluster. Assuming that no hydrogen is left on the surface at 700 K,[1] the number of C_2D_4 molecules initially adsorbed is ~2.6 per Pt_7 cluster. For as-deposited Pt_7/alumina heated to 700 K prior to C_2D_4 TPD/R, the amount of C_2D_4 (~1.8/Pt_7) and D_2 (~1.3/Pt_7) is 10–15% lower, and shifted to lower temperatures. The reduction in desorption is stronger if Pt_7/alumina is heated to only 300 K prior to C_2D_4 TPD/R (~1.4 C_2D_4, ~1.0 D_2), presumably because 300 K causes some cluster restructuring, but does not desorb adventitious CO.

Crampton *et al*. recently reported a study of ethylene hydrogenation to ethane over size-selected Pt_n deposited on MgO that provides an interesting point of comparison.[36] In their experiment, they coadsorbed hydrogen and ethylene before carrying out TPR, and measured desorption of ethane. In our experiments, there could potentially also be hydrogen present on the surface due to dissociative adsorption of ethylene; however, we did not see any evidence for ethane production. This absence of ethane production may simply reflect the relatively low concentration of hydrogen, as compared to a situation where hydrogen is dosed along with ethylene. However, we note that Crampton *et al*. did not observe hydrogenation for Pt_n smaller than Pt_{10}.

The effects of boration, that is, of 1.5 L diborane exposure and heating, are more

dramatic. For either 300 or 700 K heating, desorption of C_2D_4 is strongly attenuated and shifted to lower temperatures (Figure 3.3b). Note that we do observe a small amount of boron deposition on Pt-free alumina films, presumably at defects; however, this is found to have no effect on the amount or temperature of C_2D_4 desorption. After these contributions are subtracted, the integrated C_2D_4 desorption is found to be only 0.75/Pt_7 (300 K) and 0.9/Pt_7 (700 K). Boration has no significant effect on the temperature onset for D_2 production, but the amount of D_2 is more than 5 times lower than for as-deposited Pt_7/alumina (0.27 and 0.25/Pt_7–B_2H_6 for 300 and 700 K heating, respectively). Assuming again that no hydrogen is left on the surface at 700 K, the total initial coverage of ethylene is ~0.83/Pt_7B and ~1.02/Pt_7B for samples heated to 300 and 700 K, respectively. It is somewhat surprising that there is not a larger difference between the ethylene chemistry on samples prepared by diborane exposure followed by heating to 300 or 700 K. ISS shows that substantially more B_xH_y adsorbates remain on the surface of the Pt clusters after 300 K heating; yet they appear to have only a modest effect on the amount of ethylene binding and its propensity to dehydrogenate.

One question is whether any hydrogen is left on the Pt clusters after boration, that is, after diborane exposure and heating to 700 K. If so, this would complicate measurement of ethylene TPD/R because of possible H/D exchange. To test for this process in a somewhat simpler system, we exposed a borated sample to D_2, which adsorbs dissociatively on Pt_7/alumina, undergoing recombinative desorption between ~200 and 350 K. If there were significant H concentration on the sample, significant HD (mass 3) desorption should occur. None was observed, indicating insignificant residual H concentration on the borated samples.

From the perspective of coke reduction, these effects of boration should increase the durability of the catalyst. In alkane dehydrogenation, the goal is to produce alkenes plus hydrogen, but to avoid further dehydrogenation to coke precursors like alkylidenes or alkynes.[6, 9, 37, 38] It is clear that boration substantially reduces the ethylene adsorption energy to Pt_7, such that desorption occurs below the onset temperature for dehydrogenation (Figure 3.3b). This constitutes the main result of the present work. Boration tempers but does not kill the catalytic activity of Pt clusters and thus provides a lever for adjusting the selectivity of the catalytic process and a way to eventually optimize it.

DFT provides insight into the mechanism for boron's effects on ethylene binding and decomposition. Pt_7 on alumina is negatively charged from 1.2 to 1.4 e^-, depending on cluster isomer, due to electron transfer from alumina. Upon boration, the amount of net electron transfer (ΔQ) to the cluster decreases, ranging from nearly neutral −0.3 to −1 e^-, depending on the isomer. Thus, the nucleophilicity of the Pt_7B/alumina ensemble is substantially reduced as compared to pure Pt_7/alumina. There is charge separation between atoms: positive Pt coordinated to O_{surf}, negative Pt to Al_{surf}, and positive B to O_{surf}; that is, Pt atoms within the clusters are charged nonuniformly. Negative charge is associated with cluster nucleophilicity and strong ethylene binding;[1] thus a substantial reduction in ethylene adsorption energy would be predicted just on the basis of the effects of boron on clusters' charge, consistent with the TPD/R results.

The propensity for coking is governed by how likely ethylene is to desorb from the catalyst rather than undergo dehydrogenation to form coke precursors (CH_y or C_n).[1, 7, 37-41] Therefore, we theoretically probed ethylene binding on the ensemble of

Pt_7B/alumina structures at relevant temperatures and up to the maximum coverage observed experimentally (~3 ethylene/Pt_7; see Figure 3.3a). Ethylene binds to Pt in either π- or di-σ-bonded geometries, the latter being associated with further dehydrogenation.[1, 7, 37-41] We extracted the structural information for all isomers considered, to construct ensemble percentages of di-σ-bound ethylene as a metric of ethylene activation at rising temperatures and coverages (Figure 3.3a, see the Appendix B for details). As noted above, in the experiment, borated Pt_7 binds roughly one ethylene molecule per cluster. DFT shows that ethylene preferentially binds to the more nucleophilic Pt sites on the cluster periphery and avoids the electropositive B (Appendix B, Figures B.4–B.8, Tables B.5–B.7). Moreover, with increasing coverage, ethylene reflects less cooperative adsorption on Pt_7B than observed on Pt_7: it destabilizes the system by ~0.2 eV/ethylene in Pt_7B, but stabilizes by ~0.3 eV/ethylene in Pt_7.[1]

The Pt_7B cluster ensemble also activates a decreasing fraction of ethylene as compared to Pt_7.[1] Pt_7 binds and activates for dehydrogenation more ethylene as the temperature and coverage increase. At 700 K with low coverage, only 15% of Pt_7 isomers contain di-σ ethylene; with high coverage, the percentage increases to >69%. On Pt_7B the effect is the opposite: as the temperature and coverage increase, less additional ethylene bind in the di-σ fashion. This occurs because the population becomes enriched in the species that do not activate ethylene such as the π-configuration. While the first ethylene may bind in the di-σ fashion, all subsequent ethylene molecules prefer the weaker, π-configuration associated with hydrogenation or the desorption observed in experiment. At higher coverage, configurations containing additional sp^3, di-σ bound ethylene drop from ~90% to 1.7%. This is the key to the reduced activity of Pt_7B.

Additionally, this illustrates the importance of the ensemble description of cluster catalysts. Note that if we take just the lower limit of temperature and coverage (i.e., consider just global minima with low ethylene content), we would be tempted to conclude that boration promotes rather than suppresses dehydrogenation, based on the prevalence of di-σ-bound ethylene. This result emphasizes that size- and composition-specific properties of surface-deposited cluster catalysts are not just the properties of a single structure, but of the ensembles present under reaction conditions. A number of studies have noted the importance of dynamic fluxionality in the presence of reagents, such as gas-phase Au clusters with CO/H_2O[42] or H_2,[43] H_2S splitting by heterotrimetallic anions,[44] and supported Au on magnesia[45] or ceria[46] for CO oxidation. Our theoretical study provides a comprehensive perspective of ensembles, moving the discussion beyond the low-coverage and low-temperature limit into the realm of real catalysis as evidenced by our discussion and agreement with experiment.

Born–Oppenheimer MD simulations reveal further differences between Pt_7 and Pt_7B interacting with ethylene (Appendix B, Figures B.9–B.13). In a previous publication, we predicted that in pure Pt_7 clusters, prismatic geometries would stabilize to single-layer geometries during ethylene adsorption.[1] We observe this in MD trajectories at 450, 700, and 1000 K (Appendix B, Figure B.9). At 450 and 700 K, the prismatic geometry undergoes multiple transformations: it opens from a prism to a distorted hexagon (circa MD step 150) and varies between other prismatic configurations and other single-layer configurations. At 1000 K, ethylene adsorbed to either the prismatic or the single-layer Pt_7 converts to the di-σ configuration. On single-layer Pt_7, ethylene exhibits C–H bond activation, followed by H_2 formation (Appendix B, Figure B.10). These MD

trajectories demonstrate the high reactivity of single-layer structures, particularly, in pure Pt_7.

We considered Pt_7B isomers I, II, and V as representatives of different structural classes. At 450 and 700 K with one bound ethylene molecule, the prismatic isomers I and II undergo flattening into single-layer and extended, branched configurations around the $B–O_{surf}$ anchor, exhibiting high fluxionality. At 700 K, the strongly bound, di-σ ethylene either desorbs (on isomer I) or interconverts to π-bound (on isomer II), i.e., reverts to a geometry where it should tend to hydrogenate or desorb. On the single-layer isomer V of Pt_7B, we observe activation of the C–C and C–H bonds. At 450 K, we see the activation of the C–H bonds proceeding to dissociation of 2H. At 700 K, minor restructuring of the single-layer cluster isomer occurs, and the di-σ-bound ethylene converts to π-bound. Dehydrogenation appears to proceed through a transition of an H atom from C to a neighboring Pt atom. Born–Oppenheimer MD shows that a vast variety of structures of Pt_7B with bound ethylene are dynamically visited at temperatures of 450 and 700 K (see Appendix B, Figures B.11–B.13). Even though these MD trajectories give only a partial view on the kinetic accessibility of the isomers, the results of dynamics simulations support the high isomeric diversity and the ensemble description used throughout this study. Thus, MD of these representative Pt_7B isomers available for catalysis supports the reduced activity of borated Pt_7 as compared to pure Pt_7.

Evidence that boration stabilized the catalyst is provided by monitoring changes during 6 sequential TPD/R runs (Figure 3.4a). For Pt_7/alumina, the amounts of both C_2D_4 and D_2 desorbing decrease substantially, and post-reaction XPS shows significant carbon deposition.[1] For borated Pt_7/alumina, there is essentially no change in C_2D_4 and D_2

desorption and no XPS-detectable carbon deposition. Indeed, boration lowers the C_2D_4 binding energy such that desorption, rather than dehydrogenation and coking, is favored.

The CO TPD in Figure 3.4b reveals additional details. For pure Pt_7, the number of CO binding sites is reduced dramatically after 1 C_2D_4 TPD/R run, and continues to drop during 6 C_2D_4 TPD/R runs, exhibiting binding site loss from some combination of coke deposition and cluster sintering/restructuring. Borated clusters also show a gradual decrease in the number of CO sites from sequential C_2D_4 TPD/R runs. Because no C deposits are detected with XPS, we conclude that the effect is likely attributable to cluster sintering, as supported by the smaller calculated binding energies of Pt_7B to the support (Appendix B, Tables B.3 and B.4) and greater fluxionality of shapes seen in MD, as compared to Pt_7.

Finally, we consider coking in terms of the affinity of the clusters to C atoms. As a first-order approximation, we analyzed the Boltzmann-weighted ensemble-averages of the C-binding energies (E_C) of the isomers that constitute >96% of the population at 450 and 700 K, for Pt_7, Pt_7B, and Pt_8 (Figure 3.4c), the latter included because it tends to have prismatic isomers like Pt_7B. Carbon affinity is both temperature- and isomer-dependent, but the temperature dependence for Pt_7 and Pt_7B is opposite. For Pt_7, the ensemble-average E_C increases with temperature; that is, the population evolves to include more isomers with high carbon affinity. In contrast, for Pt_7B, higher-energy planar configurations (isomers V and VI) in which B is exposed, rather than anchored to alumina (isomers I–IV), exhibit weaker E_C. As a result, the evolving ensemble for Pt_7B has decreasing carbon affinity and therefore increasing coke-resistance as temperature rises. For Pt_8, E_C also decreases with temperature, but remains much higher than for Pt_7B.

Pt_7B's resistance to carbon can again be traced to its reduced negative charge and nucleophilicity.

3.4 Conclusion

We show that nanoalloying of small, alumina-supported Pt clusters with boron has a substantial effect on the selectivity of catalytic dehydrogenation of ethylene. Boration reduces the ethylene binding energy and thus the tendency toward undesired dehydrogenation to coke precursors. Coking is one of the major mechanisms for cluster catalyst deactivation, and therefore the proposed strategy of its mitigation might be broadly valuable. The effect is linked to cluster morphologies in the statistical ensemble accessible at experimental conditions of temperature and ethylene coverage. As both temperature and coverage increase, borated clusters activate less ethylene for dehydrogenation and bind less carbon more weakly, as an ensemble, while the opposite is true for pure Pt clusters. Fundamentally, this work illustrates how size- and composition-specific properties of cluster catalysts are necessarily ensemble-averages and cannot be described by individual structures, even if they are the global minima.

3.5 Methods

3.5.1 Experimental Section

The experimental protocol has been detailed elsewhere.[1] Briefly, experiments were performed using an instrument that allows in situ sample preparation by cluster deposition and characterization by a variety of methods. Pt_7/alumina samples were prepared in ultrahigh vacuum ($\sim 1.5 \times 10^{-10}$ Torr) by growing an alumina thin film ($\sim$3

nm) on a Ta(110) single crystal, and soft landing (1 eV/atom) mass-selected Pt_7 clusters onto the support. The alumina thin films were grown using procedures adapted from the work of the Goodman[47-49] and Madey[50, 51] groups. A detailed study by Chen and Goodman[47] concluded that alumina thin (~1.5 Å) films grown on a Ta(110) single crystal have slightly distorted hexagonal symmetry that can be related to either the (0001) face of α-Al_2O_3 or the (111) face of γ-Al_2O_3. Because the films were inert to a variety of gas molecules under vacuum, the films were proposed to be preferentially oxygen terminated. In previous publications,[52, 53] we demonstrated that the adsorbate binding, reactivity, and electronic properties of Pd clusters deposited on these alumina thin films were independent of film thickness in the 3–10 nm range. In the present study, we used 3–6 nm thick films. Cluster coverage was controlled by monitoring the cluster neutralization current. All samples contained Pt_7 coverage corresponding to 1.5×10^{14} atoms/cm^2 (~0.1 Pt monolayer). Deposition took ~5–15 min.

TPD/R measurements were made with a differentially pumped mass spectrometer that views the sample through a ~2.5 mm diameter orifice in a skimmer cone, which is surrounded by directional dose tubes allowing gas exposures to the sample. For the ethylene TPD/R measurement, the sample was exposed to 5 L of C_2D_4 at a sample temperature of 150 K. The sample was then cooled to 135 K and ramped to 700 at 3 K/s, while monitoring masses of interest desorbing from the surface. For CO TPD, samples were exposed to 10 L of $^{13}C^{16}O$ at a sample temperature of 150 K, cooled to 135 K, and ramped to 700 at 3 K/s, while monitoring desorption of ^{13}CO and other masses of interest. Boration was done by exposing samples to 1.5 L of B_2H_6 at a sample temperature of 130 K, and then ramping the sample temperature up to either 300 or 700

at 3 K/s. Note that all experiments were carried out on separately prepared samples to avoid thermal or adsorbate-induced changes to the samples.

Low energy He^+ ion scattering spectroscopy (1 keV He^+, 45° angle of incidence, normal detection) was used to observe the effects of cluster size, sample heating, boration, and ethylene TPD/R on the fraction of Pt atoms exposed in the surface layer. ISS peaks result from He^+ scattering from single atoms in the surface layer, identifying the masses of those atoms. Because ISS is a destructive technique, all measurements were made on separately prepared samples or at the end of a series of experimental sequences.

3.5.2 Computational

As discussed previously,[1] PW-DFT calculations were performed using the Vienna Ab initio Simulation Package (VASP)[54-57] utilizing projector augmented wave potentials[58, 59] and the PBE[60] functional. A dense Monkhorst–Pack 8 × 8 × 3 *k*-point grid was implemented for bulk calculations of the α-Al_2O_3 unit cell with large kinetic energy cutoffs of 520.0 eV. The optimized lattice constants of a = 4.807 Å and c = 13.126 Å exhibited a slight increase of <0.1 Å as compared to experiment, typical of GGA functionals.[61, 62] The unit cell was grown to a (3 × 3) surface with the bottom half of the surface kept fixed and a vacuum gap of 15 Å. A 1 × 1 × 1 *k*-point grid centered at Γ-point, stringent convergence criteria of 10^{-5} (10^{-6}) eV for geometric (electronic) relaxations, and kinetic energy cutoffs of 400.0 eV were employed in all calculations. The Adaptive Force Field Coalescence Kick (AFFCK),[63] an adaptive global minimum and local minima search based on the Coalescence Kick (CK),[64] was used to find gas-phase Pt_7B. A per manum search of adsorbed structures consisted of deposition of the

lowest 5–6 gas-phase structures (Appendix B, Figure B.1) under PBE levels of theory with a thorough sampling of cluster faces to possible binding sites. It must be noted that with larger gas-phase clusters, the order of the lowest minima may be DFT method dependent.[63] All relevant equations such as the adsorption of reagents, sintering penalty, Gibbs or configurational entropy, among others, may be found in the Appendix B. MD calculations were also performed in VASP requiring electronic iterations to reach a convergence criterion of 10^{-8} eV per 1 fs time-step. MD trajectories of >1.5 ps were analyzed to compare adsorption behavior of ethylene on pure Pt versus borated Pt. The Nose–Hoover thermostat was used to equilibrate the system, approximating conditions to that of the NVT ensemble.

3.6 Acknowledgements

This work was supported by the Air Force Office of Scientific Research under a Basic Research Initiative grant (AFOSR FA9550-16-1-0141) to A.N.A. and S.L.A. M.-A.H. was also funded by the UCLA Graduate Division Dissertation Year Fellowship. CPU resources at the DoD (Department of Defense) High Performance Computing Modernization Program (the U.S. Air Force Research Laboratory DoD Supercomputing Resource Center–AFRL DSRC, the U.S. Army Engineer Research and Development Center–ERDC, and the Navy Supercomputing Resource Center–Navy DSRC), Pacific Northwest National Laboratory's Environmental Molecular Sciences Laboratory's (EMSL) Cascade cluster, Extreme Science and Engineering Discovery Environment's (XSEDE) computing resources, and the UCLA-IDRE cluster were used to conduct this work.

3.7 References

1. Baxter, E. T.; Ha, M.; Cass, A. C.; Alexandrova, A. N.; Anderson, S. L. *ACS Catal.* **2017**, 7, 3322– 3335

2. Kaden, W. E.; Wu, T.; Kunkel, W. A.; Anderson, S. L. *Science* **2009**, 326, 826– 829

3. Vajda, S.; Pellin, M. J.; Greeley, J. P.; Marshall, C. L.; Curtiss, L. A.; Ballentine, G. A.; Elam, J. W.; Catillon-Mucherie, S.; Redfern, P. C.; Mehmood, F. *Nat. Mater.* **2009**, 8, 213– 216

4. Lee, S.; Molina, L. M.; López, M. J.; Alonso, J. A.; Hammer, B.; Lee, B.; Seifert, S.; Winans, R. E.; Elam, J. W.; Pellin, M. J. *Angew. Chem*. **2009**, 121, 1495– 1499

5. Schulz, H. *Appl. Catal., A* **1999**, 186, 3– 12

6. Rahimi, N.; Karimzadeh, R. *Appl. Catal., A* **2011**, 398, 1– 17

7. Shaikhutdinov, S. K.; Frank, M.; Bäumer, M.; Jackson, S. D.; Oldman, R. J.; Hemminger, J. C.; Freund, H. *Catal. Lett.* **2002**, 80, 115– 122

8. Hansen, T. W.; DeLaRiva, A. T.; Challa, S. R.; Datye, A. K. *Acc. Chem. Res.* **2013**, 46, 1720– 1730

9. Galvita, V.; Siddiqi, G.; Sun, P.; Bell, A. T. *J. Catal.* **2010**, 271, 209– 219

10. Dadras, J.; Shen, L.; Alexandrova, A. *J. Phys. Chem. C* **2015**, 119, 6047– 6055

11. Shen, L.; Dadras, J.; Alexandrova, A. N. *Phys. Chem. Chem. Phys.* **2014**, 16, 2 6436– 26442

12. Ha, M.; Dadras, J.; Alexandrova, A. *ACS Catal.* **2014**, 4, 3570– 3580

13. Johns, T. R.; Gaudet, J. R.; Peterson, E. J.; Miller, J. T.; Stach, E. A.; Kim, C. H.; Balogh, M. P.; Datye, A. K. *ChemCatChem* **2013**, 5, 2636– 2645

14. Tan, K. F.; Chang, J.; Borgna, A.; Saeys, M. *J. Catal.* **2011**, 280, 50– 59

15. Xu, J.; Chen, L.; Tan, K. F.; Borgna, A.; Saeys, M. *J. Catal.* **2009**, 261, 158– 165

16. Levine, J. B.; Tolbert, S. H.; Kaner, R. B. *Adv. Funct. Mater.* **2009**, 19, 3519– 3533

17. Cooley, J.; Aronson, M.; Fisk, Z.; Canfield, P. *Phys. Rev. Lett.* **1995**, 74, 1629

18. KüPers, M.; Lutz-Kappelman, L.; Zhang, Y.; Miller, G. J.; Fokwa, B. P. *Inorg. Chem.* **2016**, 55, 5640– 5648

19. Nandula, A.; Trinh, Q. T.; Saeys, M.; Alexandrova, A. N. *Angew. Chem., Int. Ed.* **2015**, 54, 5312– 5316

20. Popov, I. A.; Jian, T.; Lopez, G. V.; Boldyrev, A. I.; Wang, L. S. *Nat. Commun.* **2015**, 6, 8654

21. Chan, C. W. A.; Mahadi, A. H.; Li, M. M.; Corbos, E. C.; Tang, C.; Jones, G.; Kuo, W. C. H.; Cookson, J.; Brown, C. M.; Bishop, P. T. *Nat. Commun.* **2014**, 5, 5787

22. Krawczyk, M.; Sobczak, J.; Palczewska, W. *Catal. Lett.* **1993**, 17, 21– 28

23. Dadras, J.; Jimenez-Izal, E.; Alexandrova, A. N. *ACS Catal.* **2015**, 5, 5719– 5727

24. Roberts, F. S.; Kane, M. D.; Baxter, E. T.; Anderson, S. L. *Phys. Chem. Chem. Phys.* **2014**, 16, 26443– 26457

25. Desrosiers, R. M.; Greve, D. W.; Gellman, A. J. *J. Vac. Sci. Technol., A* **1997**, 15, 2181– 2189

26. Krawczyk, M. *Appl. Surf. Sci.* **1998**, 135, 209– 217

27. Rodriguez, J. A.; Truong, C. M.; Corneille, J.; Goodman, D. W. *J. Phys. Chem.* **1992**, 96, 334– 341

28. Casadesus, P.; Frantz, C.; Gantois, M. *Metall. Trans. A* **1979**, 10, 1739– 1743

29. Weiss, H.; Knight, J.; Shapiro, I. *J. Am. Chem. Soc.* **1959**, 81, 1826– 1827

30. Söderlund, M.; Mäki-Arvela, P.; Eränen, K.; Salmi, T.; Rahkola, R.; Murzin, D. Y. *Catal. Lett.* **2005**, 105, 191– 202

31. Arnold, N.; Braunschweig, H.; Dewhurst, R. D.; Ewing, W. C. *J. Am. Chem. Soc.* **2016**, 138, 76– 79

32. Cui, Q.; Musaev, D. G.; Morokuma, K. *Organometallics* **1998**, 17, 742– 751

33. McKee, M. L. *J. Phys. Chem.* **1990**, 94, 435– 440

34. Curtiss, L. A.; Pople, J. A. *J. Chem. Phys*. **1989**, 90, 2522– 2523

35. Ganguli, P.; McGee, H., Jr. *J. Chem. Phys.* **1969**, 50, 4658– 4660

36. Crampton, A. S.; Rötzer, M. D.; Ridge, C. J.; Schweinberger, F. F.; Heiz, U.; Yoon, B.; Landman, U. *Nat. Commun.* **2016**, 7, 10389

37. Neurock, M.; van Santen, R. A. *J. Phys. Chem. B* **2000**, 104, 11127– 11145

38. Chen, Y.; Vlachos, D. G. *J. Phys. Chem. C* **2010**, 114, 4973– 4982

39. Anderson, A. B.; Choe, S. *J. Phys. Chem.* **1989**, 93, 6145– 6149

40. Windham, R. G.; Koel, B. E. *J. Phys. Chem.* **1990**, 94, 1489– 1496

41. Windham, R.; Koel, B. E.; Paffett, M. *Langmuir* **1988**, 4, 1113– 1118

42. Xing, X.; Li, X.; Yoon, B.; Landman, U.; Parks, J. H. *Int. J. Mass Spectrom*. **2015**, 377, 393– 402

43. Gao, M.; Lyalin, A.; Takagi, M.; Maeda, S.; Taketsugu, T. *J. Phys. Chem. C* **2015**, 119, 11120– 11130

44. Adhikari, D.; Raghavachari, K. *J. Phys. Chem. A* **2016**, 120, 466– 472

45. Häkkinen, H.; Abbet, S.; Sanchez, A.; Heiz, U.; Landman, U. *Angew. Chem., Int. Ed.* **2003**, 42, 1297– 1300

46. Ghosh, P.; Farnesi Camellone, M.; Fabris, S. *J. Phys. Chem. Lett.* **2013**, 4, 2256– 2263

47. Chen, P.; Goodman, D. *Surf. Sci.* **1994**, 312, L767–

48. Street, S.; Goodman, D.; King, D.; Woodruff, D. *Chem. Phys. Solid Surf.* **1997**, 8, 375– 406

49. Lai, X.; Chusuei, C. C.; Luo, K.; Guo, Q.; Goodman, D. *Chem. Phys. Lett.* **2000**, 330, 226– 230

50. Wu, Y.; Garfunkel, E.; Madey, T. E. *Surf. Sci.* **1996**, 365, 337– 352

51. Wu, Y.; Garfunkel, E.; Madey, T. E. *J. Vac. Sci. Technol., A* **1996**, 14, 2554– 2563

52. Kane, M. D.; Roberts, F. S.; Anderson, S. L. *Faraday Discuss*. **2013**, 162, 323– 340

53. Kane, M. D.; Roberts, F. S.; Anderson, S. L. *J. Phys. Chem. C* **2015**, 119, 1359– 1375

54. Kresse, G.; Hafner, J. Phys. Rev. B: Condens. *Matter Mater. Phys.* **1993**, 47, 558

55. Kresse, G.; Hafner, J. Phys. Rev. B: Condens. *Matter Mater. Phys.* **1994**, 49, 14251

56. Kresse, G.; Furthmüller, *J. Comput. Mater. Sci.* **1996**, 6, 15– 50

57. Kresse, G.; Furthmüller, *J. Phys. Rev. B: Condens. Matter Mater. Phys.* **1996**, 54, 11169

58. Blöchl, P. E. *Phys. Rev. B: Condens. Matter Mater. Phys.* **1994**, 50, 17953

59. Kresse, G.; Joubert, D. *Phys. Rev. B: Condens. Matter Mater. Phys.* **1999**, 59, 1758

60. Perdew, J. P.; Burke, K.; Ernzerhof, M. *Phys. Rev. Lett.* **1996**, 77, 3865

61. Bourdillon, A.; El-Mashri, S.; Forty, A. *Philos. Mag. A* **1984**, 49, 341– 352

62. Levin, I.; Brandon, D. *J. Am. Ceram. Soc.* **1998**, 81, 1995– 2012

63. Zhai, H.; Ha, M.; Alexandrova, A. N. *J. Chem. Theory Comput.* **2015**, 11, 2385–2393

64. Averkiev, B. Ph.D. Thesis, Utah State University, Logan, UT, 2009.

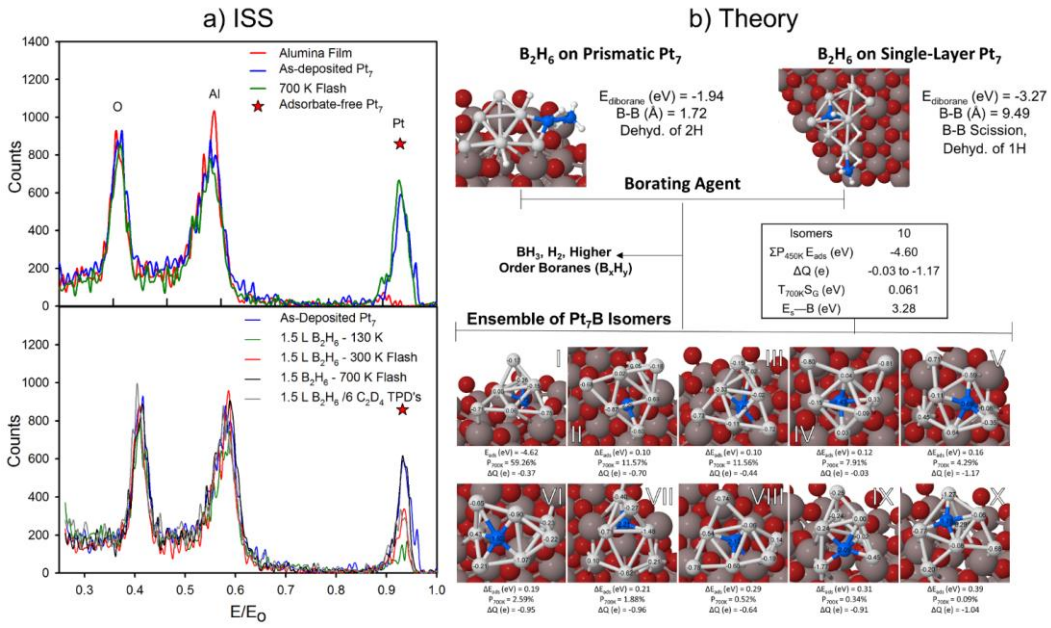

Figure 3.1: (a) Raw ISS spectra for Pt_7/alumina samples (top) measured immediately after depositing 0.1 ML of Pt_7 (blue) and after flashing Pt_7/alumina to 700 K (green). The spectrum for Pt-free alumina is shown for comparison. (bottom) Raw ISS spectra for as-deposited (blue), after 1.5 L B_2H_6 exposure at 130 K (green), after 1.5 L B_2H_6 at 130 K exposure followed by heating to 300 K (red) or 700 K (black), and after 700 K boration followed by 6 C_2D_4 TPD/R runs (gray). The extrapolated value for adsorbate free Pt_7/alumina is shown by red ★. (b) Diborane adsorption results in borated Pt sub-nanoclusters (top). The lowest minima of adsorbed isomers of Pt_7B with adsorption energy (E_{ads}), adsorption energies of local minima relative to the global minimum (ΔE_{ads}), Boltzmann populations at 700 K, and charge transfer (ΔQ) (bottom). Aluminum atoms are dark gray; oxygen, dark red; platinum, light gray; boron, blue; and hydrogen, white.

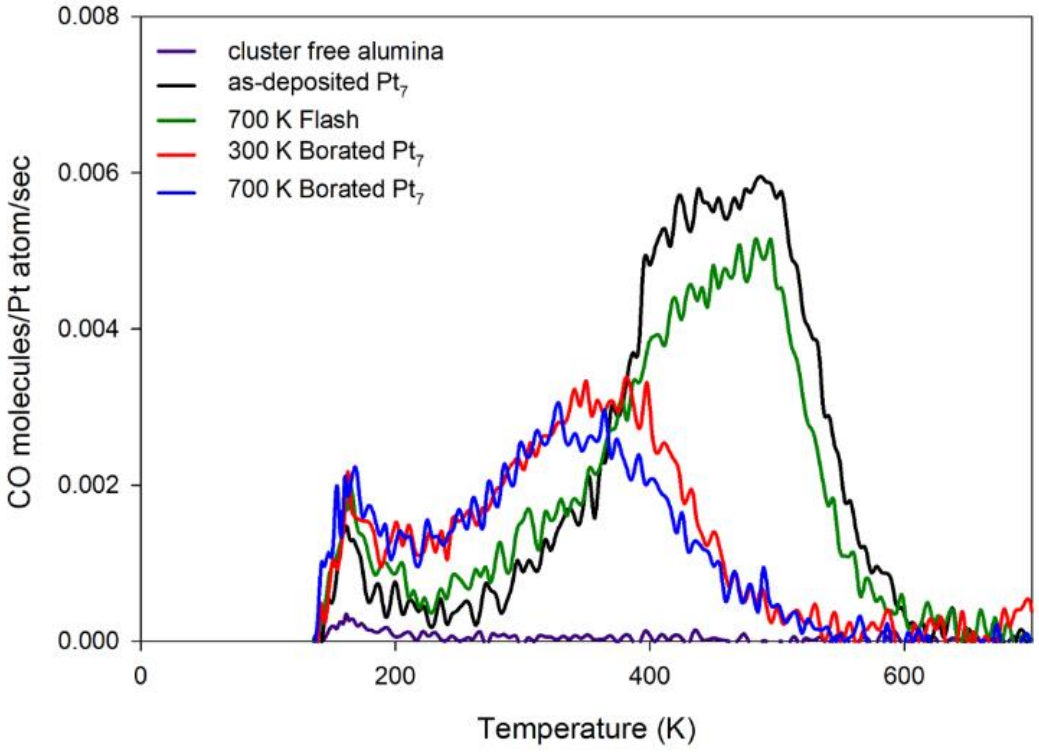

Figure 3.2: Comparison of CO TPD for a set of Pt_7/alumina samples that were first exposed to a particular manipulation and then probed by CO TPD (10 L ^{13}CO exposure at 150 K, heating at 3 K/s to 700 K).

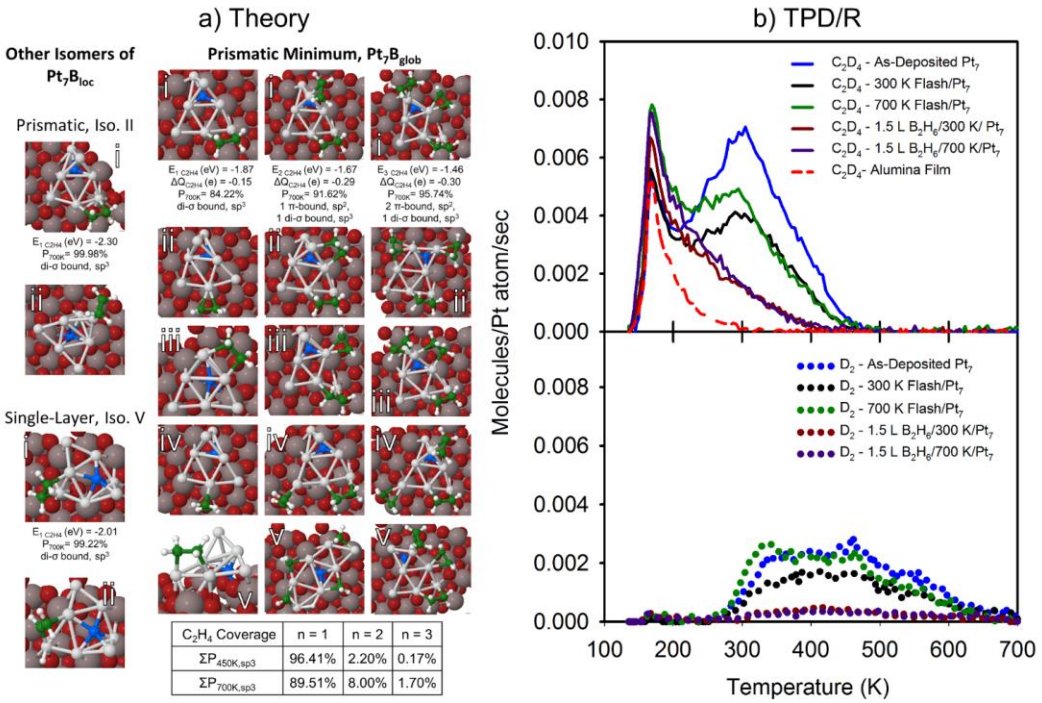

Figure 3.3: (a) Deposition of ethylene on isomers I, II, and V of Pt_7B from DFT. In π-bound ethylene, both C atoms adsorb to a single Pt site and remain sp^2-hybridized (bond angles of ~120° and a C–C bond-length of ~1.4 Å). Di-σ bound ethylene binds to two Pt sites and becomes sp^3-hybridized (bond angles of ~109° and a C–C bond of ~1.5 Å). With increasing temperature and coverage, less ethylene binds as di-σ. Additional minima not visualized here may be found in APPENDIX B along with other structural data such as charges and bonding discussion. Aluminum atoms are dark gray; oxygen, dark red; platinum, light gray; boron, blue; carbon, green; and hydrogen, white. (b) Intact C_2D_4 (solid) and D_2 (dots) desorbing from Pt_7/alumina samples after various treatments: as-deposited (blue), 300 K flash (black), 700 K flash (green), 1.5 L of B_2H_6 with 300 K flash (dark red), and 1.5 L of B_2H_6 with 700 K flash (purple). The (red) dashed line represents ethylene desorption from the cluster-free alumina.

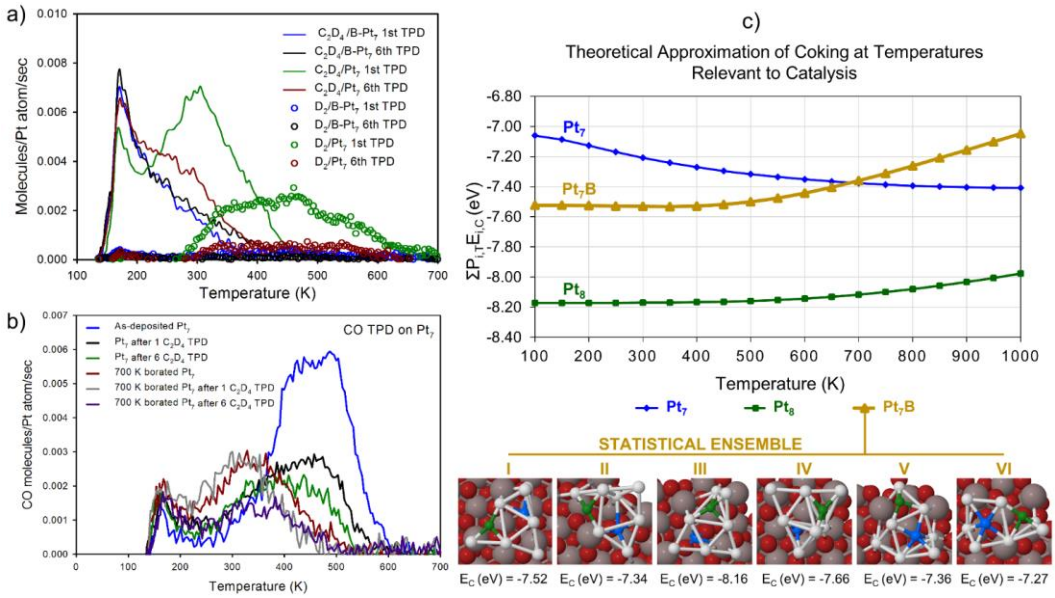

Figure 3.4: (a) Intact C_2D_4 (solid) and D_2 (dots) desorbing from Pt_7/alumina samples after various treatments: Pt_7 1st TPD/R run (green), Pt_7 6th C_2D_4 TPD/R run (dark red), borated Pt_7 1st TPD/R run (blue), and borated Pt_7 6th TPD/R run (black). (b) CO TPD from Pt_7 with different treatments: Pt_7 as-deposited (blue), Pt_7 after one C_2D_4 TPD/R run (black), Pt_7 after six C_2D_4 TPD/R runs (green), borated Pt_7 as prepared (dark red), borated Pt_7 after one C_2D_4 TPD/R run (gray), and borated Pt_7 after six C_2D_4 TPD/R runs (purple). The number of CO binding sites on pure Pt_7/alumina dramatically decreases after dehydrogenation, whereas borated clusters show fewer CO binding sites and shift toward weaker CO binding. (c) First-order approximation of coking: Boltzmann-weighted C-sticking energies for an ensemble. The Pt_7B isomers included in the ensemble are visualized at the bottom. As temperature rises, borated Pt exhibits increasing resistance to carbon. Boltzmann weights utilized as-deposited Pt_7, Pt_8, and Pt_7B adsorption energies. Aluminum atoms are dark gray; oxygen, dark red; platinum, light gray; boron, blue; and carbon, green.

CHAPTER 4

DIBORANE INTERACTIONS WITH Pt_7/ALUMINA: PREPARATION OF SIZE-CONTROLLED BORATED Pt MODEL CATALYSTS WITH IMPROVED COKING RESISTANCE

4.1 Overview

Bimetallic catalysts provide the ability to tune catalytic activity, selectivity, and stability. Model catalysts with size-selected bimetallic clusters on well-defined supports offer a useful platform for studying catalytic mechanisms, however, producing size-selected bimetallic clusters can be challenging. In this study, we present a way to prepare bimetallic model (Pt_nB_m/alumina) cluster catalysts by depositing size-selected Pt_7 clusters on an alumina thin film, then selectively adding boron by exposure to diborane and heating. The interactions between Pt_7/alumina and diborane were probed using temperature-programmed desorption/reaction (TPD/R), X-ray photoelectron spectroscopy (XPS), low energy ion scattering (ISS), plane wave density functional theory (PW-DFT), and molecular dynamic (MD) simulations. It was found that the diborane exposure/heating process does result in preferential binding of B in association with the Pt clusters. Borated Pt clusters are of interest because they are known to exhibit reduced affinity to carbon deposition in catalytic dehydrogenation. At high temperatures, theory, in agreement with experiment, shows that boron tends to migrate to sites beneath the Pt clusters forming Pt-B-O_{suf} bonds that anchor the clusters to the alumina support.

4.2 Introduction

Carbon deposition (i.e., "coking") leads to deactivation of catalysts in important reactions such as Fisher-Tropsch synthesis,[1] hydrocarbon cracking,[2] and alkene dehydrogenation.[3] It has been demonstrated that boration of extended surfaces of Co[4] and Ni[5] can extend the lifetime of catalysts without compromising their activity toward Fischer-Tropsch synthesis and steam reforming, respectively. In both processes, coking is the

mechanism of deactivation. We recently showed that boration also reduces coking on size-selected Pt clusters deposited on alumina during dehydrogenation of alkenes.[6] This type of catalytic system is novel and so-far largely under-investigated, including several aspects of their preparation, experimental characterization, theoretical analysis, and structural, dynamical, and chemical properties.

Model catalysts with atomically size-selected clusters on well characterized supports provide a useful platform for studying catalysis mechanisms, allowing independent control of the size and density of catalytic sites, and facilitating detailed theoretical studies. Bimetallic catalysts provide important opportunities to tune catalytic activity, selectivity, and stability. However, extending the size-selected model catalyst approach to bimetallic clusters is challenging. One approach is to use alloy or dual target cluster sources that directly produce bimetallic clusters in the gas phase, which can then be mass selected and deposited to create bimetallic model catalysts.[7-10] This approach is quite general, in principle, however, for several reasons it becomes increasingly difficult as the cluster size increases. The cluster source intensity is "diluted" over an increasing number of possible M_xN_y combinations, and the intensity is further decreased by the need for high mass-selector resolution to separate closely spaced masses. Intensity is important, because clusters quickly become contaminated due to substrate-mediated adsorption,[11-13] even in ultra-high vacuum (UHV). In many cases, natural isotope distributions exacerbate these problems such that clean selection of both size and composition may be impossible except for very small clusters. For example, Pt has *major* isotopes with atomic masses 194, 195, 196, and 198, and boron has isotopes with atomic masses 10 and 11. Thus, even for clusters containing only three Pt atoms, the width of the Pt isotopologue distribution is greater than

the boron mass, resulting in mass overlaps between Pt_3B_n and $Pt_3B_{n\pm1}$.

One motivation for this paper is to report a complementary approach to producing size-selected bimetallic cluster catalysts, in which mass-selected cluster deposition is used to create a size-selected model catalyst (here, Pt_n/alumina), which is then used to seed deposition of a second element to create a bimetallic model catalyst (here, Pt_nB_m/alumina). The challenge is to find conditions where boron deposits only on the Pt clusters, and then to characterize the nature of the resulting doped clusters.

4.3 Methods

As outlined below, alumina-supported size-selected $Pt_{4,7,8}$ model catalysts were prepared, and then exposed to diborane and heated to drive decomposition and H_2 desorption. The goal is to selectively borate the Pt clusters, thus it is important to understand how diborane interacts with both Pt_n clusters and the alumina support. These interactions were probed by temperature-programmed desorption and reaction (TPD/R), low energy He^+ ion scattering (ISS), and X-ray photoelectron spectroscopy (XPS) experiments on both Pt-free alumina and Pt_n/alumina samples, by plane wave density functional theory (PW-DFT) calculations of adsorption geometries and energetics, and molecular dynamic (MD) simulations of borane surface chemistry. We previously showed that the chemical consequences of boration are similar for different Pt cluster sizes.[6] Here we focus on the boration mechanism, using Pt_7/alumina as the example system.

4.3.1 Computational

As discussed previously in detail,[14] PW-DFT calculations with projector augmented wave potentials[15-16] and the PBE[17] functional were implemented in the Vienna Ab initio Simulation Package (VASP).[18-21] The bulk-optimized unit cell with lattice constants of a = 4.807 Å and c = 13.126 Å was grown to a (3 × 3) surface, a slight expansion as compared to experiment.[22-23] A vacuum gap of 15 Å was added to the slab. The bottom half of the surface was kept fixed. For all calculations, convergence criteria of 10^{-5} (10^{-6}) eV for geometric (electronic) relaxations, expansion of the plane waves' kinetic energy to 400.0 eV, and a k-point grid of 1 × 1 × 1 centered at the Γ-point were instituted. We previously discussed the global optimization of Pt_7 on the model α-alumina surface,[14] finding a number of low-lying isomers for Pt_7/alumina. As shown below, the global minimum has Pt_7 in a prismatic (i.e., 3D) structure with Pt_7-alumina adsorption energy of -5.09 eV, however, there are isomers only 0.05 eV higher in energy in which all Pt atoms are in a single layer bound to the alumina surface.

A *per manum* search for diborane adsorption geometries associated with both the prismatic and single layer Pt_7/alumina structures was made, starting with the molecule positioned at bridging, hollow, and atomic (atop) sites, oriented both parallel and normal to the surface plane, and rotated in various orientations. The starting geometries focused on adsorption of diborane to the Pt clusters, rather than to the α-Al_2O_3 surface. The adsorption energy of diborane was calculated via the relation:

$$E_{B2H6} = E[\text{Surf} + Pt_7\text{-}B_2H_6] - E[B_2H_6]_{gas} - E[\text{Surf} + Pt_{7,glob}].$$

Ab-initio MD calculations, starting at the lowest minimum of diborane adsorbed on both the prismatic and single-layer Pt_7/alumina structures, were also performed.

Equilibration of the system utilized the Nose-Hoover thermostat and an electronic convergence criterion of 10^{-8} eV per 1 fs time-step was implemented. The global optimization of Pt_4B_4 adsorbed on alumina was performed using the Basin Hopping method adapted for surface deposited clusters.[24] The local minima search for gas phase Pt_4B_4 also utilized Basin Hopping. The adsorption energy of Pt_4B_4 was taken as:

$$E_{ads} = E[Surf + Pt_4B_4] - E[Pt_4B_4]_{gas,glob} - E[Surf].$$

4.3.2 Experimental

The experiments were conducted with an instrument consisting of a mass-selected metal cluster ion deposition beamline[25] that terminates in an ultrahigh vacuum (~1.5×10^{-10} Torr) analysis chamber that allows *in situ* sample preparation and characterization, as discussed previously, along with several of the experimental protocols used here.[12, 26-27] The Pt_n/alumina model catalysts were prepared on a 7×7 mm Ta(110) single crystal mounted using Ta heating wires to a liquid nitrogen reservoir at the end of a manipulator. The sample temperature was controlled between 110 and >2100 K by the combination of resistive and electron-bombardment heating and liquid nitrogen cooling. Temperature was measured by a C-type thermocouple spot welded to the back of the Ta single crystal.

Procedures for alumina film growth were adapted from the Goodman[28-30] and Madey[31-32] groups. At the beginning of each experiment, the Ta single crystal was annealed above 2100 K for 5 minutes or until no surface contaminants were detected by XPS and ISS. For alumina film growth, the Ta(110) substrate was transferred to a separately pumped UHV antechamber, heated to 970 K in 5×10^{-6} Torr of O_2, while exposed to Al evaporating from a crucible mounted normal to the Ta(110) surface. In previous studies, we

demonstrated that the reactivity, adsorbate binding, and electronic properties of Pd clusters deposited on alumina were independent of film thickness in the 3-10 nm range. For these studies the typical growth rate was ~0.2 nm/min and 3-6 nm thick films were used.

Before beginning cluster deposition, the alumina/Ta(110) support was flashed to ~800 K to desorb adventitious adsorbates. To minimize the time the clusters were exposed to background gases, Pt cluster deposition was done as the sample cooled after the flash, beginning when the sample reached ~300 K. The clusters were deposited onto the alumina support through a 2 mm diameter mask, and cluster coverage was controlled by monitoring the neutralization current of soft landed (~1 eV/atom) clusters on the support. Unless stated otherwise, all samples were prepared with Pt_7 coverage of 2.14 x 10^{13} clusters/cm^2, amounting to 1.5×10^{14} Pt atoms/cm^2, equivalent to ~10% of a close-packed Pt monolayer.

TPD/R measurements were made using a differentially pumped mass spectrometer that views the main UHV chamber through the ~2.5 mm diameter aperture in a skimmer cone. The cone was surrounded by four directional dose tubes that pointed at the sample position, and gas doses for both TPD/R and diborane exposure were done using the tubes to minimize gas exposures to the vacuum system. To calibrate the exposures, we compared subsaturation CO TPD signals for CO delivered through the dose tubes and through a gas inlet remote from the sample position. During both gas dosing and the subsequent TPD/R heat ramp, the chamber pressure was monitored by a nude ion gauge, and ion signals of interest were measured by the differentially pumped mass spectrometer. The analyte molecules were ionized by electron impact ionization (EI) using electrons with a nominal energy of 65 eV. This energy was found to give the best intensity for D_2 and C_2D_4 detection. Diborane TPD/R was done by exposing samples to B_2H_6 at 130 K sample temperature,

followed by heating to 700 K. For ethylene TPD/R, the sample was exposed to 5 L of C_2D_4 at a sample temperature of 150 K (to minimize multilayer adsorption), cooled to 130 K, and then heated to 700 K while monitoring signals for $C_2D_4^+$, D_2^+, and various background gases.

Boron was introduced into the UHV system in the form of a diborane/argon gas mixture that we characterized mass spectrometrically to have actual composition of 4.8% diborane, 85% argon, and 10.2% H_2, the latter assumed to result from diborane decomposition during storage.[33] Diborane exposures were calculated based on the measured diborane mole fraction. In most experiments, boration was done by exposing the samples to 1.5 L of diborane at a sample temperature of 130 K, followed by heating to 700 K, which was found to be sufficient to drive desorption to completion. Note that 1.5 L diborane exposure corresponds to ~5.8 x 10^{14} diborane molecules impinging *per* cm^2, that is, smaller than the total number of surface atoms, but almost four times larger than the number of Pt atoms. A few experiments were performed using a 0.5 L diborane exposure, where the number of impinging diborane molecules (1.9 x $10^{14}/cm^2$) was only ~25% greater than the number of Pt atoms present. The dose variation had little effect on the sample properties, suggesting that 1.5 L should be more than sufficient to saturate the Pt cluster binding sites.

Because the gas mixture contained hydrogen, and diborane decomposition also produces hydrogen, we studied TPD following pure D_2 exposure, in separate experiments. H_2 desorption during diborane TPD/R could not be monitored because the mass 2 background in the mass spectrometer was too high.

XPS (Al Kα) was used to examine both alumina and Pt_7/alumina samples after B_2H_6

exposure, both while holding the sample at the 130 K dose temperature, and after heating the sample to 700 K. Since both boron and Pt are present only in the surface layer, and we know the Pt coverage quite precisely, the boron coverage was estimated from the ratio of B 1s and Pt 4d XPS integrated intensities. The Pt 4d XPS signal was used because of overlap between Pt 4f and Al 2p. Both Pt and B are present at low coverage, and because the B 1s photoemission cross section is ~40 times smaller than that for Pt 4d,[34] the boron XPS signal is quite weak. To improve the signal/noise, the boron XPS measurements were done using samples with double the normal Pt_n coverage (i.e., 0.2 ML). Higher cluster coverage undoubtedly resulted in some increase in cluster agglomeration during deposition and heating, however, because the effects of boration do not appear to be very dependent on cluster size,[6] a modest degree of agglomeration is unlikely to have a significant effect on the B/Pt ratio. To insure that the diborane exposure was sufficient to saturate the larger number of Pt_7 present, we also doubled the diborane dose to 3.0 L.

For ISS, a beam of 1 keV He^+ was loosely focused onto the surface at 45° angle of incidence and the energy distribution of He^+ scattered along the surface normal was measured. Peaks in ISS result from scattering of He^+ from single atoms in the sample, predominantly in the surface layer.[35] Multiple scattering and scattering from subsurface layers contributes primarily to a weak background. In these experiments, ISS was used to monitor the intensities associated with Pt, Al, and O atoms in the top sample layer. H is undetectable by ISS, and the boron ISS signal also proved to be undetectable, due to the combination of low He^+ scattering cross section ($\sigma_{scatt} \propto Z_{target}$), low boron coverage, and rising background in that energy range from multiple scattering. Because ISS is a destructive technique, the ISS experiments were done either on separately prepared

samples or at the end of other experimental sequences.

4.4 Results

4.4.1 Temperature Programmed Desorption/Reaction Following Adsorption of B_2H_6 and D_2

TPD/R experiments were used to identify species desorbing from alumina and Pt_7/alumina surfaces, and the associated temperature dependences (i.e., energetics). Because the literature shows that diborane can polymerize on surfaces,[36] we monitored masses relevant to known boranes of various sizes. Figure C.1 in Appendix C shows the raw TPD signals for ion masses 11, 26, 48, and 59, which are low background masses corresponding to $B_1H_x^+$,$B_2H_x^+$, $B_4H_x^+$, and $B_5H_x^+$ (the ^{11}B:^{10}B isotope ratio is ~80:20). Figure 4.1 shows the data corrected, as described below, for the estimated contributions from fragmentation of higher boranes during election impact ionization (EI). Data are shown for desorption from both alumina and Pt_7/alumina samples, each exposed to 1.5 L of B_2H_6 at 130 K, then heated at 3 K/sec. Note that desorption starts at ~120 K, i.e., slightly below the dose temperature. This reflects the fact that diborane pumps out of the system slowly, so that there was a small additional exposure as the sample cooled to the TPD/R start temperature.

The assignment of the ion signals to desorbing species is complicated by the fact that boranes fragment extensively in EI.[37] We corrected the TPD signals for fragmentation of diborane, tetraborane (B_4H_{10}) and pentaborane (B_5H_9), which all have tabulated standard EI mass spectra, but did not attempt to correct for possible contributions from higher boranes (i.e., B_nH_m, $n > 5$). It should be noted that ion fragmentation is very sensitive to

the internal energy of the neutral. Therefore, analysis of the TPD/R products using standard mass spectra from the NIST database is useful, but my not be quantitative. The dominant EI fragment ions for boranes tend to preserve the number of boron atoms ($B_nH_m \rightarrow B_nH_{m-x}^+$), however, there is some signal for essentially all possible $B_xH_y^+$ ($x \leq n$, $y \leq m$) fragments.[37] For example, mass 59 is the strongest peak in the EI mass spectrum of pentaborane (MW = 63.13), and mass 48 is the strongest peak for tetraborane (MW = 53.32), however, pentaborane EI also produces mass 48 with ~18% of the mass 59 intensity. Mass 26 is the most intense peak in the EI mass spectrum of diborane (MW=27.67), but 26 is also produced at the few percent level by EI of tetra- and pentaborane.

In Figure 4.1, no correction was made to the mass 59 intensity for possible contributions from EI of B_nH_m ($n \geq 6$), but the mass 48 signal was corrected for cracking of pentaborane, the mass 26 signal was corrected for cracking of pentaborane and tetraborane, and the mass 11 signal was corrected for contributions from penta-, tetra-, and diborane, using NIST standard mass spectra.[37] As can be seen by comparing Figures 4.1 and C.1, the corrections are generally quite small. The only qualitatively obvious change is that a peak in the raw signal for mass 48 in the 150 – 170 K range is shown to result almost entirely from EI cracking of pentaborane.

One surprise is that the mass 11 signal ($^{11}B^+$ and $^{10}BH^+$) is quite high, even after subtraction of the expected contributions from EI fragmentation of di-, tetra-, and pentaborane. We considered the possibility that the high mass 11 intensity might be an artifact of high mass spectrometer sensitivity to light masses, but this explanation is ruled out by the excellent agreement of our mass spectrum for diborane with the NIST standard

diborane spectrum.[37] For example, when we leak diborane into our UHV system, we measure a mass 11:26 intensity ratio of ~0.3:1, in good agreement with the 0.28:1 ratio reported in the NIST database. It is also unlikely that the high mass 11 signal could result from EI fragmentation of higher boranes (B_nH_m, $n \geq 6$), because these, if present in high enough yield to account for such high mass 11 signal, would also result in much higher mass 59 signal than is observed. For example, hexaborane (B_6H_{10}) fragments in EI to produce both masses 11 and 59, however, the mass 59 intensity is ~1.5 times that of mass 11.[37]

Therefore, we conclude that the high mass 11 signal must largely result from desorption of some BH_x species, such as borane (BH_3). Diborane is a hydrogen-bridge-bonded dimer, with gas-phase dissociation enthalpy to 2 BH_3 of only 1.78 eV (i.e., 0.89 eV/BH_3),[38] and both BH_3 and BH_2 are detected mass spectrometrically in gas-phase pyrolysis of diborane at 300 °C.[39] We observe mass 11 desorption signal at low temperatures, raising the question of how BH_2 or BH_3 production is energetically feasible. For reactions of diborane on a surface, the energy required to generate gas-phase BH_x may be supplied by recombination reactions (e.g., producing tetra- and pentaborane) or by formation of strong B-surface bonds.

We also looked for possible desorption of diborane surface reaction products during the 130 K dose, by monitoring masses 11, 26, 48, and 59 during diborane dosing. Signals for masses 11 and 26 were observed in a 0.27:1 ratio, as expected for gas phase diborane, indicating that the diborane sticking probability at 130 K is less than unity, and that little or no borane (BH_3) desorbs during the dose. Subunit sticking probability is unsurprising, given that 130 K is only 10 K below the peak of the diborane desorption during TPD/R.

Small signals were also observed for masses 48 and 59 during the dose, but these were only 1.2 % and 0.4 % of the mass 26 (diborane) signal for the alumina sample and just 0.2 % and 0.1 % of the diborane signal for Pt_7/alumina. Clearly, if borane, tetraborane, or pentaborane form on the surface during the diborane dose, they mostly remain adsorbed until the sample is heated.

We estimated desorption energies for the different species by fitting the TPD/R temperature dependence to a second order kinetic model, that is, assuming that the rate-limiting step is recombination of adsorbed B_xH_y fragments to generate the various boranes observed. The desorption energy distributions are shown in Figures C.2 and C.3, and the desorption energies all fall in the 0.4 to 0.5 eV range.

Diborane surface chemistry will be discussed in more detail after the rest of the experimental and theoretical results are presented. The most important points to keep in mind are:

1. Because all boranes fragment in EI to produce at least some mass 11, the absence of mass 11 signal above ~200 K implies that desorption of boron-containing species is complete by 200 K.

2. The mass 11 signal is far too large to be explained by EI fragmentation of B_nH_m ($n \geq 2$), implying that there is considerable desorption of BH_x.

3. The fact that masses 11, 48, and 59 are observed with higher intensities than mass 26 implies that most of the desorbing boron fraction is in the form of reaction products, rather than diborane.

4. Desorption from alumina and Pt_7/alumina are qualitatively similar, as might be expected, considering that 90% of the Pt_7/alumina surface is alumina.

5. The total amount of B_nH_m desorption is ~13% lower when Pt_7 is present at 10% coverage, and the desorption peaks are shifted 5 to 10 K to higher temperatures.

Species such as B_4H_{10} and B_5H_9 have the H:B ratios that are smaller than that for diborane (3:1). In addition, the XPS results discussed next show that a significant amount of boron remains on the surface after B_nH_m desorption has gone to completion. It is clear, therefore, that hydrogen must also be desorbing during diborane TPD/R. Observation of the diborane → H_2 desorption channel is not possible, both because the mass 2 background is high, and because the diborane reactant gas mixture has substantial H_2 concentration. To provide some insight into the binding/desorption behavior of hydrogen on Pt_7/alumina, we measured D_2 desorption from a separate Pt_7/alumina sample dosed with 5 L of D_2 at 130 K, and the result is shown in Figure C.5. A small amount of D_2 desorption is observed in the temperature range below ~200 K, where borane desorption occurs, but ~90% of hydrogen desorption occurs at higher temperatures, between 200 and 400 K.

4.4.2 X-Ray Photoelectron Spectroscopy

TPD/R probes the B_nH_m species that desorb upon heating, but from the perspective of selectively borating the Pt clusters, it is more important to understand the fate of the boron that remains on the surface. XPS was used to probe the fraction of B on the samples before and after heating. Figure 4.2 compares B 1s spectra for both alumina and Pt_7/alumina samples, after exposure to 3 L of B_2H_6 at 130 K and after subsequent heating to 700 K. As noted above, the low B 1s photoemission cross section results in poor signal, and the XPS experiments were done using a sample with Pt_7 deposited at

twice the normal coverage (~3 x 10^{14} Pt atoms/cm^2).

The B 1s XP spectrum of diborane adsorbed at 130 K on Pt_7/alumina is noisy (bottom right frame) but clearly indicates the presence of two components, fit by peaks at 189.7 and 193.9 eV, suggesting the presence of at least two boron chemical environments. The 130 K spectrum for Pt-free alumina (bottom left) has similar intensity peaking near 193 eV, but the low binding energy intensity is weaker than in the Pt_7/alumina sample. A similar two-component fit was used for this spectrum, resulting in peaks centered at 189.7 and 193.1 eV. After heating to 700 K, only a single broad B 1s feature remains for both alumina and Pt_7/alumina, peaking at 190.5 eV binding energy.

The integrated intensities, indicated in each frame of the figure, provide additional insight into diborane interactions with alumina and Pt_7. Note that the integrated B 1s intensity at 130 K, that is, the total amount of boron adsorbed, is ~45% higher when Pt_7 is present. Heating to 700 K to desorb all volatile boron species, leads to loss of ~34% of the initial B 1s signal for alumina, but only ~22% of the (initially larger) B 1s signal for Pt_7/alumina. Thus, after heating, the amount of boron remaining on the sample is ~71% higher when Pt_7 is present, even though the Pt_7 coverage was only ~20%. This result can be compared to the TPD/R results, which showed ~13% less desorption of boron-containing species when Pt_7 was present (at 10% coverage). Taken together, both TPD/R and XPS show that substantially more boron adsorbs when Pt_7 is present, but that less desorbs, that is, the presence of a low coverage of Pt_7 leads to substantially more boron deposition on the samples.

4.4.3 Temperature-Dependent Ion Scattering Spectroscopy

The final experimental probe of diborane-surface interactions was temperature-dependent He^+ ion scattering (TD-ISS). TD-ISS involves cooling the sample, exposing it to an adsorbate of interest, then monitoring changes in ISS intensities as the sample is heated. A typical raw ISS scan (Figure C.4) shows distinct peaks for single scattering from Pt, O, and Al atoms in the surface layer,[35] along with a featureless background due to multiple and subsurface scattering. As discussed previously,[12, 14] Pt_7 deposits in an ensemble of prismatic and single layer structures, with most of the Pt in the surface layer, and thus detectable by ISS. Adsorbates attenuate ISS signals from the underlying surface through a combination of shadowing, blocking, and reduced ion survival probability.[35, 40] For our scattering geometry, attenuation primarily affects signal from atoms directly under, or surrounding, the adsorbate. Thus, adsorbates binding directly on top of the Pt clusters attenuate Pt signal, with little or no effect on Al or O signals. Conversely, adsorption on the alumina film, or at sites around the periphery of the clusters, tends to attenuate Al and O signals, with little or no effect on the Pt signal. As heating drives desorption, the attenuated ISS signals should tend to recover toward the adsorbate-free values. To the extent that diborane exposure and heating leads to cluster agglomeration, forming larger multilayer Pt particles, this would reduce the fraction of Pt in the surface layer, and thus the Pt ISS signal.

As shown in Figure C.4, there is no obvious ISS signal for boron ($E/E_0 \approx 0.26$) in the spectrum taken immediately after diborane exposure at 110 K, nor is B ISS signal observed after heating the sample, despite the evidence that boron must be present on these samples (Figures 4.1 and 4.2). Lack of boron signal could be taken as evidence that boron

is not in the surface layer, however, boron may simply have been undetectable due to a combination of low coverage, small He^+-B scattering cross section ($\propto$ target atomic number[35]), and high multiple-scattering background at low E/E_0.

Figure 4.3 compares the Pt, O, and Al ISS signals as a function of temperature, for a Pt_7/alumina sample that was exposed to 1.5 L of B_2H_6 at 110 K, probed by ISS, and then heated to 700 K in 50 K steps, with an ISS measurement made at each temperature. All spectra were collected with low (0.1 μA) He^+ flux impinging at 45° and detected along the surface normal, with 30 second scan time used to minimize sample damage. The horizontal dashed lines show the Pt, O, and Al intensities measured for adsorbate-free Pt_7/alumina in a separate experiment. Compared to these adsorbate-free values, the signals measured after the B_2H_6 dose are attenuated by ~80% for Pt and ~20% for O and Al, indicating that B_2H_6 binds preferentially in sites that attenuate Pt ISS signal. ISS, thus, is consistent with the XPS and TPD/R results indicating that diborane binds preferentially in association with Pt_7, and provides the additional insight that some or all of this Pt-associated diborane binds on top of the clusters, where it attenuates scattering from underlying Pt. The ~20% attenuation of Al and O signals indicates that some diborane binds in sites that shadow or block scattering from alumina, which could include both sites around the periphery of the clusters, and on the alumina film remote from the clusters.

Interpretation of changes in signal as the sample is heated requires knowledge of the effects of He^+ bombardment occurring during the repeated ISS scans used in TD-ISS. To probe the rate of Pt loss by sputtering, an experiment was made on a separate adsorbate-free Pt_7/alumina sample, held at constant temperature, while taking a series of ISS spectra. The rate of Pt ISS signal decrease is indicated in Figure 4.3 by the dashed line labeled “Pt

signal loss from sputtering." Conversely, for a diborane-covered Pt_7/alumina sample held at 110 K, the Pt signal slowly increased during successive ISS scans, due to sputtering of adsorbates initially bound on top of the clusters, as indicated by the line labeled "Pt signal recovery from B_2H_6 sputtering." The Al and O ISS signals were not observed to change significantly in either control experiment, presumably because the diborane coverage on alumina is low, and sputtering of Al or O from the top layer simply exposes more Al and O in the second layer.

As shown in Figure 4.3, the Pt ISS signal starts to recover significantly faster than would be expected from B_2H_6 sputtering at ~200 K, gradually recovering to ~95% of the adsorbate-free value by ~550 K, then is constant at higher temperatures. The Al and O signals remain attenuated up to ~450 K but then recover to their adsorbate-free values by 700 K.

4.4.4 DFT Results for Adsorption of Diborane on Pt_7 Clusters

PW-DFT calculations were performed to identify low energy adsorption geometries for diborane on Pt_7/alumina, as summarized in Figure 4.4. We previously reported on the energetics and geometries of numerous isomers of Pt_7 and Pt_8 bound to alumina.[14] Here, we focus on adsorption of diborane on the two lowest energy minima of Pt_7/alumina, which are shown in the small figures next to the titles of each section of Figure 4.4. The most stable Pt_7/alumina structure is prismatic (E_{ads} = -5.09 eV, relative to alumina + gas phase Pt_7), but there is a single-layer isomer that is only slightly higher in energy (E_{ads} = -5.04 eV). Seven different isomers of diborane adsorbed on both prismatic and single layer Pt_7/alumina are shown, all of which would contribute to the population at 700

K and below, according to Boltzmann statistics. In these 0 K, *in vacuo* calculations, the most stable configurations of diborane on the prismatic Pt_7 cluster preserve the B-B bond and are adsorbed atop or peripherally to the cluster. On single-layer Pt_7, however, the most stable structures involve B-B bond scission.

There are several factors to bear in mind in comparing theory to experiment. Due to computational limits, our DFT calculations were restricted to adsorption of only a single diborane and focused on the strongest diborane binding sites, that is, diborane binding on the clusters. The experimental diborane coverages were higher and populated binding sites on both Pt_7 and the alumina film. As a result, the calculations cannot address complex chemistry such as higher borane formation and desorption. In addition, while the minima found by DFT clearly illustrate a variety of binding arrangements, we cannot guarantee that they represent all possible low energy binding geometries. Indeed, the fluxionality of these clusters is important in their catalysis but also resists facile theoretical description.[6, 14, 41-44] The complexity of the problem will certainly increase at elevated temperatures or for increasing coverage of B_2H_6.

For prismatic Pt_7/alumina, the most stable isomer in absence of adsorbates, diborane adsorbs atop or at peripheral sites on the cluster. The B-B bond is preserved with only one or two H atoms transferred from diborane to Pt sites. The B-B bond lengths range from 1.72 to 1.88 Å, compared to 1.76 Å calculated for gas-phase diborane (Figure C.6), in excellent agreement with the experimental value (1.7645 Å).[45] Relative to prismatic Pt_7/alumina + gas phase B_2H_6, the most stable binding geometry for diborane on prismatic Pt_7 has E_{ads} = -1.94 eV, and the other structures shown are all within 0.2 eV (ΔE_{ads}). The atomic charges for the various isomers of diborane adsorbed on prismatic Pt_7/alumina are

shown in Figure C.7.

Diborane binds more strongly to the single layer Pt_7/alumina isomer, with E_{ads} = -3.22 eV for the most stable structure. Note that three of the seven isomers shown involve B-B bond scission and other isomers feature a B-B bond elongated by 7-14% compared to gas-phase B_2H_6. All isomers involve transfer of up to three H atoms from B to Pt sites. The atomic charges for the various isomers of diborane adsorbed on single layer Pt_7/alumina are shown in Figure C.8.

The substantially higher E_{ads} for diborane on the single layer Pt_7 isomer implies that with one diborane adsorbed, single layer Pt_7/alumina becomes the global minimum by ~1.2 eV. The barrier height for diborane-induced isomerization from the prismatic local minimum to the single layer global minimum is unknown, but comparison with ethylene adsorption is suggestive. DFT also found that ethylene adsorbed more strongly on single layer Pt_7/alumina (E_{ads} = -1.97 eV), compared to prismatic Pt_7/alumina (E_{ads} = -1.29 eV), and in that case, adsorption of three ethylene molecules was sufficient to eliminate the prismatic-to-single-layer isomerization barrier for Pt_7.[14] The difference in adsorption energy for diborane on the two Pt_7 isomers is almost twice as large as the difference for ethylene, suggesting that isomerization is not unlikely at the diborane exposures used in the experiments.

4.4.5 Molecular Dynamics Simulations of Diborane/ Pt_7/Alumina Thermal Chemistry

To probe adsorbate effects and chemistry at the elevated temperatures used in the experiments, we used Born-Oppenheimer MD simulations to examine the fate of

diborane adsorbed on Pt_7 at 450 and 700 K. Both of these temperatures are well above the range where B_nH_m desorption is observed (Figure 4.1) and in the range where H_2 desorption occurs on Pt clusters (Figure C.5). This is also the range of interest for ethylene dehydrogenation, which peaks near 450 K for Pt_7/alumina and goes to completion below 700 K.[14] The prismatic and single-layer minima of Pt_7 represent different initial geometries for diborane to adsorb and react on. Selected highlights from MD trajectories on each structure at both temperatures are given in Figures 4.5 and 4.6, respectively (each MD time step corresponds to 1 fs).

Starting with the lowest energy minimum for diborane on prismatic Pt_7, MD shows that at these elevated temperatures diborane undergoes B-B scission to form BH_2, BH_3, or BH_4 fragments, which may then re-adsorb onto Pt sites (Figure 4.5). Interestingly, in the 450 K trajectory, diborane dehydrogenated completely with one of the boron atoms moving to a position underneath the Pt_7 cluster, forming Pt-B-O_{surf} bonds and anchoring the cluster to the alumina surface. In contrast, in the 700 K trajectory, the Pt cluster flattened to a triangular, single-layer structure with BH fragments maximizing the number of Pt-B bonds. Throughout the MD trajectories, at both temperatures, hydrogen atoms are mobile, translating to adsorb onto the Pt cluster, to Al, O atoms on alumina, or forming H_2 (shown desorbing from the surface). Moreover, both the 450 and 700 K MD trajectories favored B-B bond scission early on, within the first 120 fs of the simulation.

Starting with lowest energy isomer of diborane on single-layer Pt_7, at either 450 or 700 K, the Pt cluster retains much of its structure with B or BH_y fragments making small translations (Figure 4.6). Similar to the prismatic Pt cluster, at 450 K, diborane's boron atoms either sit on top of the cluster to maximize Pt-B bonds or move below the cluster to

form Pt-B-O_{surf} anchor bonds. At 700 K, BH fragments sit on the Pt cluster facets, forming 3-4 Pt-B bonds.

Due to computational time limitations, we were only able to run a few trajectories, following the dynamics for ~5 ps. Of course, the MD picture is incomplete, and only accesses a small portion of configurational space accessible to our systems. Nonetheless, these MD results give insight into possible decomposition mechanisms of diborane on alumina-supported Pt clusters. One obvious point is that Pt, B, and H atoms are all mobile at these temperatures, consistent with the DFT finding of numerous structures within a few tenths of an eV of the global minimum. By the end of the trajectories, the Pt_7 clusters remained intact, but most of the initial B-H bonds had broken, with H atoms binding instead to Pt or to O atoms of the support, and some H atoms recombined to form H_2 seen desorbing from the surface, even on the relatively short time scale of the trajectory. Boron atoms prefer to bind either under the cluster, forming Pt-B-O_{surf} linkages, or to facets of the Pt clusters, forming multiple Pt-B bonds. Boron atoms bound to Pt facets may block preferred carbon adsorption sites or weaken carbon adsorption, which may account for the observed resistance to coking of borated Pt clusters.[4-6] However, B bound between the cluster and the support also affects the affinity to C by altering the electronic structure of the system, particularly, the charge transfer from the support to the cluster, as was shown previously.[6]

At the higher diborane coverages of the experiments, additional processes, presumably, would occur, such as coupling of BH fragments to form higher boranes that might desorb (Figure 4.1) and more extensive recombinative desorption of H_2. Over longer time scales, particularly at 700 K, additional hydrogen desorption would almost certainly occur, leaving behind Pt_7B_x clusters. The simulations suggest that the Pt_7B_x clusters would

have a range of Pt morphologies (prismatic and single-layer) and boron binding sites (Pt facets, Pt-B-O_{surf}), and the cluster structures are likely fluxional at high temperatures.

4.4.6 Pt_4B_4/Alumina

As a computationally tractable model for Pt_nB_m clusters with higher boron mole fraction, as probably form in the experiments, we chose to study Pt_4B_4 clusters. The global optimization search for gas-phase and adsorbed Pt_4B_4 was performed utilizing the Basin Hopping method,[24] and the set of low energy isomers is shown in Figures 4.7 and C.9 for Pt_4B_4/alumina and gas-phase Pt_4B_4, respectively. Both gas-phase and adsorbed Pt_4B_4 structures tend to be (quasi-)planar. Huynh *et al*. ascribed the drive towards planarity with increasing boron concentration to the covalent nature of boron-boron bonds and boron-metal bonding in mixed metal-boron clusters in B_nAl_{6-n} and LiB_nAl_{6-n} systems, and proposed that this effect may be general to other metal-boron systems.[4-6, 46] Noticeably, their study found the transition from predominantly 3D to 2D structures occurs when the Al:B ratio is 1:1. The Pt-B clusters seem to follow a similar pattern, with the single-layer geometry dominating in gas-phase Pt_4B_4 (isomers i-iii, see Appendix C) as compared to Pt_7B (isomers v).[6]

For alumina-supported Pt_4B_4, the Pt_4 moiety is also near-planar, however, the B atoms tend to be bent toward the alumina support to allow formation of short B-O_{surf} bonds anchoring the Pt_4 moiety to the alumina. The B-B bonds in surface-bound clusters are ~1.7 Å, and Pt-B bonds are ~2 Å. The results also show that, even for high boron concentrations, the energetically favorable structures have all the Pt atoms in the surface layer, with most or all of the B atoms underneath the clusters. This has important implications for

interpretation of the TD-ISS results, and also means that all the Pt atoms are exposed and available to act as catalytic sites.

In previous publications, we predicted that addition of electropositive boron would temper the highly active and electronegative Pt clusters by reducing the charge of the cluster.[6, 47] High electron density favors ethylene adsorption in sp^3-hybridized geometries, a precursor to dehydrogenation. On the other hand, sp^2-hybridization tends to favor hydrogenation or desorption.[1, 3, 48-50] In pure Pt_7 and Pt_8 clusters on alumina, Pt atoms were found to have charges ranging from +0.78 e, when bound primarily to O_{surf}, to -0.73 e, when bound primarily to Al_{surf}, with net cluster charge being ca. -1 e.[14] For Pt_7B on alumina, the net charge on the clusters dropped to ca. -0.35 e, with strong variations from one isomer to another.[6] With increasing boron content, Pt_4B_4 clusters on alumina become positively charged, between +0.68 and +1.32 e. In addition, the charge separation between Pt and B atoms increases with increasing boron concentration: Pt remains negative, ranging from -0.5 to -1.1 e, and B atoms are positively charged, between +0.4 e, when forming a mix of Pt-B or B-B bonds within the cluster, and +1.87 e, when forming a B-O_{surf} anchor. Increasing the B:Pt ratio also increases the stability of supported Pt-B clusters with Pt_4B_4 adsorbing more strongly by ~1.9 eV as compared to Pt_7B (E_{ads} = -4.62 eV[6]). This may be attributed to the cluster maximizing B-O_{surf} interactions and optimizing the electrostatic attraction between the electronegative Pt atoms and electropositive B atoms with a 1:1 ratio of Pt:B.[51]

4.5 Discussion

4.5.1 Decomposition of Diborane on Pt_7/Alumina

From our previous study of ethylene dehydrogenation on borated Pt clusters, we know that boration of Pt_7/alumina substantially reduces the ethylene desorption temperature, resulting in a significant decrease in the fraction of ethylene that undergoes unwanted dehydrogenation.[6] The obvious questions are how much boron is deposited on the Pt_7/alumina surface by the boration process used, and in what kinds of binding sites is it found.

Figure 4.1 shows that quite complex chemistry occurs when diborane is adsorbed on both alumina and Pt_7/alumina surfaces. The chemistry is qualitatively similar for the two surfaces, reflecting the fact that the Pt_7 coverage is only 10%. Similarities include the low intensity for diborane desorption (mass 26), and higher intensities for desorption of both BH_x (mass 11) and higher boranes such as tetraborane (mass 48) and pentaborane (mass 59). The fact that desorption is dominated by B_1 or B_n $(n \geq 4)$ species indicates that adsorbed diborane dissociates at low temperatures, undergoing complex recombination chemistry.

The DFT results support this conclusion, showing that, even at 0 K, diborane spontaneously loses H atoms on both prismatic and single layer Pt_7, and that on the single layer isomer, B-B bond scission also occurs. Given that the single layer isomer becomes the global minimum upon diborane adsorption, extensive diborane decomposition is expected. That expectation is supported by the MD trajectory results, in which B-B bond scission and Pt_7 isomerization is observed on the picosecond time scale at moderate temperatures. Experimentally (Figure C.5) and computationally (Figure 4.6), hydrogen

recombinative desorption is observed at moderate temperatures, suggesting that the final state of the borated Pt_7/alumina samples consists primarily of Pt and B atoms, binding in some fashion to the alumina support.

The XPS results in Figure 4.2 show that a significant fraction of the boron initially adsorbed as diborane is left behind after thermal desorption is complete. The amount of boron on the surface can be estimated from XPS peak intensities. For this analysis we take advantage of the fact both Pt and B are deposited on the sample surface at low coverage, and that we know the amount of Pt deposited quite precisely (1.5×10^{14} Pt atoms/cm^2). Attenuation by inelastic scattering can be neglected for photoelectrons emitted by atoms in the surface layer, thus for the Pt_7/alumina sample, the B/Pt coverage ratio can be calculated from the ratio of integrated B 1s and Pt 4d intensities. The only information needed for this calculation is the ratio of B 1s and Pt 4d photoemission cross sections, for which we used theoretical cross sections reported by Yeh *et al.*[34] ($\sigma_{B1s} = 6.6 \times 10^{-3}$ Mb, $\sigma_{Pt4d} = 2.64 \times 10^{-1}$ Mb), which we checked against empirical atomic sensitivity factors[52] taking the electron attenuation length into account.[53] (For our 54.7° x-ray source-analyzer angle, photoemission asymmetry can be neglected).[54] For the Pt-free alumina sample, we determined the boron coverage by comparison to the Pt_7/alumina sample studied under identical conditions. Because of the extremely weak B 1s signal (Figure 4.2), the resulting boron coverages are estimated to have uncertainties of ±40%.

For the Pt-free alumina film, this analysis gives a boron coverage immediately after 130 K diborane exposure of ~9.8 B atoms/nm^2 corresponding to ~5 B_2H_6/nm^2. From its structure, we can estimate that an intact diborane molecule lying flat on a surface would occupy roughly 0.06 nm^2, thus the boron coverage is equivalent to roughly 30% of a close-

packed monolayer. That can be compared to the ~20% attenuation of Al and O ISS signals observed after 130 K diborane exposure in the ISS experiment (Figure 4.3). After heating the alumina sample to 700 K, the B 1s signal decreased by ~34% to ~6.5 B/nm^2, compared to ~15 O atoms, and 10 Al atoms *per* nm^2 of the alumina film.

For the sample containing 0.2 ML-equivalent of Pt_7 clusters, the amount of B_2H_6 adsorbed at 130 K increased to ~14.2 B/nm^2 or ~7 B_2H_6/nm^2. If we assume the diborane coverage on the alumina portion of the 0.2 ML Pt_7/alumina sample is just 0.8 of the coverage observed on Pt-free alumina, we can estimate that ~4 of the B_2H_6 molecules are on alumina sites, and ~3 are associated with Pt sites. This 0.2 ML-equivalent sample had 0.43 Pt_7 clusters deposited *per* nm^2, leading to the conclusion that ~7 diborane molecules are associated with each Pt_7 cluster. The large attenuation of Pt ISS signal upon diborane exposure (Figure 4.3) shows that a significant fraction of the Pt-associated diborane is bound in sites on top of the clusters, but we cannot rule out some diborane in sites around the cluster periphery. We note that for a single B_2H_6, DFT found that diborane fragments occupy both "on top" and peripheral sites (Figure 4.3). Heating the sample to 700 K resulted in final B coverage of ~11 B/nm^2. On Pt-free alumina, the final B coverage was 6.5 B/nm^2, thus from the 80:20 alumina:Pt area ratio, we can estimate that of the 11 B/nm^2, ~5.2 are bound to alumina sites, and the remaining ~5.8 B are bound to Pt sites, or 13.5 B atoms/Pt_7. Prior to heating, there were 7 diborane molecules = 14 B atoms in Pt-associated sites. This observation suggests that diborane initially adsorbed in Pt-associated sites decomposes during heating, leaving nearly all of its boron atoms on the surface. The implication is that essentially all the boranes desorbing from Pt_7/alumina (Figure 4.1) can be attributed to diborane initially adsorbed on alumina sites. If that conclusion is correct,

we would expect ~10% less borane desorption from 0.1 ML Pt_7/alumina, compared to Pt-free alumina, which is reasonably consistent with the observation of ~13% less desorption.

The B 1s binding energies also provide insight into the nature of the binding. Diborane adsorbed at 130 K on Pt_7/alumina gives rise to a high binding energy peak at 193.9 eV and a broader low binding energy feature that peaks around 189.7 eV. For diborane on alumina, there is a peak at 193.1 eV with similar intensity to that for Pt_7/alumina but the signal at low binding energies is much weaker than for the Pt_7/alumina. The higher binding energy features are in the energy range (193 – 193.7 eV) typically reported for fully oxidized boron (B^{3+}) in compounds such as boron oxide or boric acid.[55] Elemental boron (B^0) is reported to have binding energies around 188 eV,[55] thus the broad 189.7 eV features are suggestive of boron in some partially oxidized form, which obviously is more prevalent when Pt_7 is present. DFT was used to calculate the charges for a single diborane on both prismatic and single layer isomers of Pt_7/alumina, as shown in Figures C.7 and C.8, respectively. It can be seen that roughly half the boron atoms in the various isomers tend to be fully oxidized (B^{3+}), and half are in intermediate oxidation states ($B^{1.5+}$ to $B^{1.6+}$). These results appear to be in good agreement with the observed binding energies. It should be noted, however, that for the higher diborane coverages in the experiments, higher boranes form on the surface. B 1s binding energies for such species are not known, but we note that an orthocarborane ($B_{10}C_2H_{12}$) film deposited on copper is reported to have B 1s binding energy of 189.3 eV,[56] also in reasonable agreement with the lower binding energy feature. For reference, in previous studies of low temperature diborane adsorption/decomposition on Mo(100) and Ni(100) two B 1s peaks were observed at 189.2 eV and 187.6 eV, but in those experiments the boranes were binding directly to metals,

rather than oxides.

After heating to 700 K, both alumina and Pt_7/alumina samples show a single broad B 1s peak at ~190.5 eV, suggesting boron is present in a distribution of intermediate oxidation states. This conclusion is broadly consistent with the distribution of boron oxidation states ($B^{0.5+}$ - $B^{1.9+}$) found for B atoms in Pt-B-O_{surf} bridge bonds, as shown for Pt_4B_4 in Figure 4.7.

In summary, XPS indicates that at 130 K, diborane adsorbs preferentially in association with Pt clusters, compared to the alumina support, and that little, if any, of this Pt-associated boron desorbs during heating to 700 K. As a result, the boration process investigated leaves Pt clusters with much larger boron coverages than the alumina support. The final B:Pt ratio for the clusters is estimated to be quite high, but we note that the absolute coverages are uncertain by ~ ±40%, due to the very weak B 1s signal. Note also that both the cluster coverage and diborane exposure used in these XPS experiments was twice those for all the other experiments. It is not clear how these changes might have affected the amount of boron deposited *per* cluster, however, we did study how the diborane exposure used in boration affected subsequent ethylene TPD/R. Boration with 0.5 L diborane exposure was found to be almost as effective at suppressing dehydrogenation as boration with 1.5 L exposure, that is, at least the *chemical effects* of boration appear to saturate at exposures below those used in all the experiments described in this report.

XPS also shows that the boration process leads to some boron deposition on the alumina film support, thus it is important to know how the catalytic properties of the samples are affected by the boron atoms on (or in) the support. To address this question,

Figure 4.8 compares the ethylene adsorption, desorption, and dehydrogenation behavior of three samples:

1. As-deposited Pt_7/alumina with no boron exposure ("Pt_7/alumina").

2. Pt_7/alumina borated after cluster deposition, that is, both Pt_7 and alumina with boron ("B/Pt_7/alumina").

3. Pt_7 deposited on a pre-borated alumina support, that is, only the alumina was borated ("Pt_7/B/alumina").

Boration was done using our standard method (1.5 L B_2H_6 exposure at 130 K, followed by heating to 700 K), and ethylene TPD/R was carried out under conditions identical to those used in our previous studies[6, 14] (5 L C_2D_4 exposure at 150 K, heating at 3 K/sec to 700 K). Ethylene desorbs from Pt_7/alumina in two components. The low temperature feature was shown to result from ethylene desorbing from defect sites in the alumina film, and the broad feature peaking near 300 K results from ethylene adsorbed at Pt_7 sites.[14] A substantial amount of D_2 desorption is observed above 300 K for Pt_7/alumina, but none is observed for the alumina film alone.

Boration of both the clusters and the support (B/Pt_7/alumina) leads to a substantial decrease in the desorption temperature distribution for ethylene, and near-total attenuation of D_2 desorption. In contrast, borating only the alumina support (Pt_7/B/alumina) has little effect on the Pt_7 chemistry. The low temperature ethylene desorption feature attributed to desorption from the alumina support is less intense and sharper for this sample, suggesting that boration of the alumina support weakens the ethylene-alumina binding, possibly due to boron occupying alumina defect sites. Pre-boration has little effect, however, on the amount or temperature dependence of ethylene desorbing from Pt sites, or on the D_2

production, suggesting that the presence of a small amount of boron in the support has little effect on supported Pt clusters. Clearly, the large effects of boron on chemistry of supported Pt clusters are due to boration of the Pt clusters, rather than the support.

XPS probes boron on the surface, thus providing an indirect method to estimate the fraction that desorbs during heating. TPD/R (Figure 4.1) provides a complementary probe of the desorbing fraction, provided that we can convert the measured $B_xH_y^+$ ion signals to fluxes of various neutrals desorbing from the surface. It is impractical to directly calibrate the mass spectrometer for detection of species such as BH_3, tetraborane, or pentaborane (toxic, pyrophoric, not commercially available), but we can do an approximate analysis. We previously calibrated the ion intensity – neutral desorption relationship for C_2D_4,[14] which should have EI cross section similar to that for B_2H_6, and also has similar EI cracking behavior. For desorbing BH_x, B_4H_{10}, and B_5H_9, we note that the EI cross section should scale roughly with number of B atoms, that is, the total ionization signal should increase roughly linearly with borane size. The extent of EI cracking also increases with borane size,[37] however, such that the fraction of the ion signal appearing at the detected mass values decreases with size.[6] As a result of these two factors, we expect that the detection sensitivity for the various borane products should be similar, and that they should be similar to that for ethylene. Using this crude approximation, we can estimate that of the ~5 B_2H_6 molecules found by XPS to be adsorbed at 130 K, the equivalent of ~0.9 B_2H_6/nm^2 (~20%) desorbs in the form of various boranes, which is in reasonable agreement with the ~30% desorption estimated from XPS. For Pt_7/alumina, ~7 B_2H_6/nm^2 adsorb at 130 K, but only the equivalent of ~0.80 B_2H_6/nm^2 (~11%) desorb, compared to ~21% boron desorption estimated by XPS. Considering the crude approximations

required for this analysis, and low XPS signal, the TPD and XPS results are in reasonable agreement regarding the amount of boron lost during heating.

Figures C.2 and C.3 give the desorption energy distributions for the various borane products observed, all of which are below 0.5 eV. The DFT adsorption energies for diborane on Pt_7/alumina are all much higher – ranging up to ~3 eV on the single layer isomer. This discrepancy is easily explained. The DFT calculations were done to find the structure and energetics for a single diborane molecule in the strongest binding sites, which are on the Pt clusters. The experiments were done at much higher diborane coverages and include diborane bound to Pt sites and to the alumina film. As shown by XPS, boron bound to the Pt clusters does not desorb during heating, thus the TPD/R experiments are only sensitive to boranes desorbing by recombination of B_xH_y and H adsorbed on the alumina support, where the binding energies are clearly much lower than for Pt-associated sites.

XPS shows the amount of boron associated with Pt, but provides no insight into the nature of the boron-Pt binding. TPD/R gives the temperature ranges in which boranes (Figure 4.1) and hydrogen (Figure C.5) desorb, but provides no insight into the sites they desorb from. Analysis of the TD-ISS results (Figure 4.3) in light of the XPS and TPD data provides some of this structural information. The large attenuation of Pt ISS signal, and much smaller attenuations of Al and O signals, are consistent with the XPS results. Both show that diborane adsorbs more efficiently in association with the Pt clusters than on alumina sites, and ISS shows that a significant fraction adsorbs on top of the clusters where it attenuates Pt signal. Figure 4.1 shows that desorption of B_nH_m species is complete by ~200 K, thus it is surprising that there is no significant recovery of Pt, O, or Al ISS signals

as the sample is heated to 200 K. Recovery of the Pt ISS signal occurs in two stages at higher temperatures. Between 200 and 400 K, the Pt signal increases to about half the expected value for adsorbate-free Pt_7. This is the temperature range in which hydrogen desorbs from Pt_7 (Figure C.5), suggesting that desorption of hydrogen exposed some Pt atoms but that ~half the Pt atoms remained blocked by adsorbed boron. This conclusion is consistent with the XPS results indicating that little of the boron associated with Pt sites desorbs, that is, the borane desorption observed in TPD/R originates almost entirely from the alumina film.

Between 400 and 550 K, the Pt signal recovers to almost the adsorbate-free limit. Since nothing desorbs in this temperature range, the recovery of Pt ISS signal must reflect a structural change in the Pt clusters, and the DFT results suggest the explanation. Both the MD simulations (Figures 4.5 and 4.6) and the structures found for adsorbed Pt_4B_4 indicate that the most stable binding sites for boron atoms in Pt_nB_m clusters are in Pt-B-O_{surf} bridging sites, where the B atoms are under the Pt cluster, anchoring it to the surface. As a result, the Pt atoms are in surface layer and detectable by ISS.

The fact that the Pt ISS signal recovers to 95% of the value for adsorbate-free Pt_7 also suggests that sintering or agglomeration of the clusters during the boration process is limited, because either process would tend to form larger, 3D clusters in which a smaller fraction of Pt is in the ISS accessible surface layer. Indeed, the final Pt ISS signal is well above what would be expected from He^+ sputtering of Pt during the series of ISS scans. This, too, is consistent with the XPS results, which indicate high diborane coverage on the Pt clusters, which would tend to shield the underlying Pt from most of the sputtering that occurs for adsorbate-free clusters.

4.6 Conclusion

We have shown that diborane exposure followed by heating, preferentially deposits boron atoms on supported Pt clusters, with a much smaller boron coverage on the alumina support. The boron on the alumina support is shown to have essentially no effect on ethylene binding or dehydrogenation on the supported Pt clusters. Therefore, the weakening of the ethylene binding and suppression of dehydrogenation when Pt_n/alumina is borated can be attributed to boron atoms associated with the Pt clusters. This boron is found by DFT, in agreement with TD-ISS, to move to sites beneath the Pt clusters, forming Pt-B-O_{surf} bonds that anchor the clusters to the support.

4.7 Acknowledgement

This work was supported by the Air Force Office of Scientific Research under a Basic Research Initiative grant (AFOSR FA9550-16-1-0141) to A.N.A. and S.L.A. M.-A.H. was also funded by the UCLA Graduate Division Dissertation Year Fellowship. CPU resources at the DoD (Department of Defense) High Performance Computing Modernization Program (the US Air Force Research Laboratory DoD Supercomputing Resource Center—AFRL DSRC, the US Army Engineer Research and Development Center—ERDC, and the Navy Supercomputing Resource Center—Navy DSRC), Pacific Northwest National Laboratory's Environmental Molecular Sciences Laboratory's (EMSL) Cascade cluster, Extreme Science and Engineering Discovery Environment's (XSEDE) computing resources, and the UCLA-IDRE cluster were used to conduct this work.

4.8 References

1. Schulz, H. Short History and Present Trends of Fischer–Tropsch Synthesis. *Appl. Catal., A* **1999**, *186*, 3-12.

2. Rahimi, N.; Karimzadeh, R. Catalytic Cracking of Hydrocarbons over Modified Zsm-5 Zeolites to Produce Light Olefins: A Review. *Appl. Catal., A* **2011**, *398*, 1-17.

3. Shaikhutdinov, S. K.; Frank, M.; Bäumer, M.; Jackson, S. D.; Oldman, R. J.; Hemminger, J. C.; Freund, H.-J. Effect of Carbon Deposits on Reactivity of Supported Pd Model Catalysts. *Catal. Lett.* **2002**, *80*, 115-122.

4. Tan, K. F.; Chang, J.; Borgna, A.; Saeys, M. Effect of Boron Promotion on the Stability of Cobalt Fischer–Tropsch Catalysts. *J. Catal.* **2011**, *280*, 50-59.

5. Xu, J.; Chen, L.; Tan, K. F.; Borgna, A.; Saeys, M. Effect of Boron on the Stability of Ni Catalysts During Steam Methane Reforming. *J. Catal.* **2009**, *261*, 158-165.

6. Ha, M.-A.; Baxter, E. T.; Cass, A. C.; Anderson, S. L.; Alexandrova, A. N. Boron Switch for Selectivity of Catalytic Dehydrogenation on Size-Selected Pt Clusters on Al2o3. *J. Am. Chem. Soc.* **2017**, *139*, 11568-11575.

7. Rousset, J.; Cadrot, A.; Cadete Santos Aires, F.; Renouprez, A.; Mélinon, P.; Perez, A.; Pellarin, M.; Vialle, J.; Broyer, M. Study of Bimetallic Pd–Pt Clusters in Both Free and Supported Phases. *J. Chem. Phys.* **1995**, *102*, 8574-8585.

8. Yang, B.; Khadra, G.; Tuaillon-Combes, J.; Tyo, E. C.; Pellin, M. J.; Reinhart, B.; Seifert, S.; Chen, X.; Dupuis, V.; Vajda, S. Temperature-Dependent Evolution of the Oxidation States of Cobalt and Platinum in Co1–Xptx Clusters under H2 and Co + H2 Atmospheres. *J. Phys. Chem. C* **2016**, *120*, 21496-21504.

9. Bardotti, L.; Tournus, F.; Albin, C.; Boisron, O.; Dupuis, V. Self-Organisation of Size-Selected Coxpt1-X Clusters on Graphite. *Phys. Chem. Chem. Phys.* **2014**, *16*, 26653-26657.

10. Moskovkin, P.; Pisov, S.; Hou, M.; Raufast, C.; Tournus, F.; Favre, L.; Dupuis, V. Mo l Predictions and Experimental Characterization of Co-Pt Alloy Clusters. *Eur. Phys. J. D* **2007**, *43*, 27-32.

11. Kaden, W. E.; Kunkel, W. A.; Anderson, S. L. Cluster Size Effects on Sintering, Co Adsorption, and Implantation in Ir/Sio_2. *J. Chem. Phys.* **2009**, *131*, 114701, 1-15.

12. Roberts, F. S.; Kane, M. D.; Baxter, E. T.; Anderson, S. L. Oxygen Activation

and Co Oxidation over Size-Selected Ptn/Alumina/Re(0001) Model Catalysts: Correlations with Valence Electronic Structure, Physical Structure, and Binding Sites. *Phys. Chem. Chem. Phys.* **2014**, *16*, 26443 – 26457.

13. Aizawa, M.; Lee, S.; Anderson, S. L. Deposition Dynamics and Chemical Properties of Size-Selected Ir Clusters on Tio2. *Surf. Sci.* **2003**, *542*, 253-275.

14. Baxter, E. T.; Ha, M.-A.; Cass, A. C.; Alexandrova, A. N.; Anderson, S. L. Ethylene Dehydrogenation on Pt4,7,8 Clusters on Al2o3: Strong Cluster Size Dependence Linked to Preferred Catalyst Morphologies. *ACS Catal.* **2017**, *7*, 3322-3335.

15. Blöchl, P. E. Projector Augmented-Wave Method. *Phys. Rev. B* **1994**, *50*, 17953.

16. Kresse, G.; Joubert, D. From Ultrasoft Pseudopotentials to the Projector Augmented-Wave Method. *Phys. Rev. B* **1999**, *59*, 1758.

17. Perdew, J. P.; Burke, K.; Ernzerhof, M. Generalized Gradient Approximation Made Simple. *Phys. Rev. lett.* **1996**, *77*, 3865.

18. Kresse, G.; Furthmüller, J. Efficient Iterative Schemes for Ab Initio Total-Energy Calculations Using a Plane-Wave Basis Set. *Phys. Rev. B* **1996**, *54*, 11169-86.

19. Kresse, G.; Furthmüller, J. Efficiency of Ab-Initio Total Energy Calculations for Metals and Semiconductors Using a Plane-Wave Basis Set. *Comput. Mater. Sci.* **1996**, *6*, 15-50.

20. Kresse, G.; Hafner, J. Ab Initio Molecular Dynamics for Liquid Metals. *Phys. Rev. B* **1993**, *47*, 558.

21. Kresse, G.; Hafner, J. Ab Initio Molecular-Dynamics Simulation of the Liquid-Metal–Amorphous-Semiconductor Transition in Germanium. *Phys. Rev. B* **1994**, *49*, 14251.

22. Bourdillon, A.; El-Mashri, S.; Forty, A. Application of Tem Extended Electron Energy Loss Fine Structure to the Study of Aluminium Oxide Films. *Philos. Mag. A* **1984**, *49*, 341-352.

23. Levin, I.; Brandon, D. Metastable Alumina Polymorphs: Crystal Structures and Transition Sequences. *J. Am. Ceram. Soc.* **1998**, *81*, 1995-2012.

24. Wales, D. J.; Doye, J. P. Global Optimization by Basin-Hopping and the Lowest Energy Structures of Lennard-Jones Clusters Containing up to 110 Atoms. *J. Phys. Chem. A* **1997**, *101*, 5111-5116.

25. Boyd, K. J.; Lapicki, A.; Aizawa, M.; Anderson, S. L. A Phase-Space-

Compressing, Mass-Selecting Beamline for Hyperthermal, Focused Ion Beam Deposition. *Rev. Sci. Instrum.* **1998**, *69*, 4106-4115.

26. Kane, M. D.; Roberts, F. S.; Anderson, S. L. Mass-Selected Supported Cluster Catalysts: Size Effects on Co Oxidation Activity, Electronic Structure, and Thermal Stability of Pd_n/Alumina ($N \leq 30$) Model Catalysts. *Int. J. Mass Spectrom.* **2014**, *370*, 1-15.

27. Kane, M. D.; Roberts, F. S.; Anderson, S. L. Effects of Alumina Thickness on Co Oxidation Activity over Pd_{20}/Alumina/Re(0001): Correlated Effects of Alumina Electronic Properties and Pd_{20} Geometry on Activity. *J. Phys. Chem. C* **2015**, *119*, 1359–1375.

28. Chen, P. J.; Goodman, D. W. Epitaxial Growth of Ultrathin Al_2o_3 Films on Ta(110). *Surf. Sci.* **1994**, *312*, L767-L773.

29. Street, S. C.; Goodman, D. W. Chemical and Spectroscopic Studies of Ultrathin Oxide Films. *Chem. Phys. Solid Surf.* **1997**, *8*, 375-406.

30. Lai, X.; Chusuei, C. C.; Luo, K.; Guo, Q.; Goodman, D. W. Imaging Ultrathin Al2o3 Films with Scanning Tunneling Microscopy. *Chem. Phys. Lett.* **2000**, *330*, 226-230.

31. Wu, Y.; Garfunkel, E.; Madey, T. E. Growth and Oxidation of Ultra-Thin Al Films on the Re(0001) Surface. *Surf. Sci.* **1996**, *365*, 337-352.

32. Wu, Y.; Garfunkel, E.; Madey, T. E. Growth of Ultrathin Crystalline Al2o3 Films on Ru(0001) and Re(0001) Surfaces. *J. Vac. Sci. Technol., A* **1996**, *14*, 2554-2563.

33. Yu, J.; Boatz, J. A.; Anderson, S. L. Borane-Aluminum Surface Interactions: Enhanced Fracturing and Generation of Boron-Aluminum Core-Shell Nanoparticles. *J. Phys. Chem. C* **2017**, *121*, 14176-14190.

34. Yeh, J. J.; Lindau, I. Atomic Subshell Photoionization Cross Sections and Asymmetry Parameters: $1< Z < 103$. *At. Data and Nucl. Data Tables* **1985**, *32*, 1-155.

35. Rabalais, J. W. *Principles and Applications of Ion Scattering Spectrometry : Surface Chemical and Structural Analysis*; Wiley: New York, 2003; pp 336.

36. Bandiera, J.; Naccache, C.; Mathieu, M. V. Products Formed by the Hydrolysis of Diborane in Contact with Γ-Alumina. *C. R. Acad. Sci., Paris, Ser. C* **1969**, *268*, 901-4.

37. Stein, S. E., Ir and Mass Spectra. In *Nist Chemistry Webbook, Nist Standard*

Reference Database Number 69, Mallard, W. G, Linstrom, P. J., Eds; NIST Mass Spec Data Center, National Institute of Standards and Technology: Gaithersburg MD 20899 (http://webbook.nist.gov). 2000.

38. Chase, M. W., Jr. ; Davies, C. A.; Downey, J. R., Jr.; Frurip, D. J.; McDonald, R. A. anaf Thermochemical Tables, Third Edition. *J. Phys. Chem. Ref. Data* **1985**, *14*

39. Fehlner, T. P.; Koski, W. S. Direct Detection of the Borane Molecule and the Boryl Radical by Mass Spectrometry. *J. Am. Chem. Soc.* **1964**, *86*, 2733-2734.

40. Kaden, W. E.; Kunkel, W. A.; Roberts, F. S.; Kane, M.; Anderson, S. L. Co Adsorption and Desorption on Size-Selected Pdn/Tio2(110) Model Catalysts: Size Dependence of Binding Sites and Energies, and Support-Mediated Adsorption. *J. Chem. Phys.* **2012**, *136*, 204705/1-204705/12.

41. Zhai, H.; Alexandrova, A. N. Fluxionality of Catalytic Clusters: When It Matters and How to Address It. *ACS Catal.* **2017**, *7*, 1905-1911.

42. Gao, M.; Lyalin, A.; Takagi, M.; Maeda, S.; Taketsugu, T. Reactivity of Gold Clusters in the Regime of Structural Fluxionality. *J. Phys. Chem. C* **2015**, *119*, 11120-11130.

43. Hakkinen, H.; Abbet, S.; Sanchez, A.; Heiz, U.; Landman, U. Structural, Electronic, and Impurity-Doping Effects in Nanoscale Chemistry: Supported Gold Nanoclusters. *Angew. Chem., Int. Ed.* **2003**, *42*, 1297-1300.

44. Xing, X.; Li, X.; Yoon, B.; Landman, U.; Parks, J. H. Dynamic Fluxionality and Enhanced Co Adsorption in the Presence of Coadsorbed H 2 O on Free Gold Cluster Cations. *Int. J. Mass Spectrom.* **2015**, *377*, 393-402.

45. Sams, R. L.; Blake, T. A.; Sharpe, S. W.; Flaud, J. M.; Lafferty, W. J. High-Resolution Infrared Study of the N14, N17, and N18bands Of11b2h6and10b11bh6. *J. Mol. Spectrosc.* **1998**, *191*, 331-342.

46. Huynh, M. T.; Alexandrova, A. N. Persistent Covalency and Planarity in the B N Al6–N 2–and Lib N Al6–N–(N= 0–6) Cluster Ions. *J. Phys. Chem. Lett.* **2011**, *2*, 2046-2051.

47. Dadras, J.; Jimenez-Izal, E.; Alexandrova, A. N. Alloying Pt Sub-Nano-Clusters with Boron: Sintering Preventative and Coke Antagonist? *ACS Catal.* **2015**, 5719-5727.

48. Perry, D. A.; Hemminger, J. C. Σ-Bond Metathesis on a Surface: Dehydrogenation of Cyclohexane on Hydrogen-Saturated Pt (111). *J. Am. Chem. Soc.* **2000**, *122*, 8079-8080.

49. Carlsson, A.; Madix, R. The Dynamics of Ethylene Adsorption on Pt (111) into Di-Σ and Π-Bonded States. *J. Chem. Phys.* **2001**, *115*, 8074-8082.

50. Stöhr, J.; Sette, F.; Johnson, A. L. Near-Edge X-Ray-Absorption Fine-Structure Studies of Chemisorbed Hydrocarbons: Bond Lengths with a Ruler. *Phys. Rev. Lett.* **1984**, *53*, 1684.

51. Ha, M.-A.; Dadras, J.; Alexandrova, A. Rutile-Deposited Pt–Pd Clusters: A Hypothesis Regarding the Stability at 50/50 Ratio. *ACS Catal.* **2014**, *4*, 3570-3580.

52. Moulder, J. F.; Stickle, W. F.; Sobol, P. E.; Bomben, K. D.; Chastain, J., King, R.C. J. *Handbook of X-Ray Photoelectron Spectroscopy*; Physical Electronics: Eden Prarie, MN, 1995.

53. Powell, C. J.; Jablonski, A. *Nist Electron Effective-Attenuation-Length Database* 1.0; NIST: Gaithersburg, 2001.

54. Briggs, D.; Seah, M. P. *Practical Surface Analysis, Volume 1 : Auger and X-Ray Photoelectron Spectroscopy*, 2nd ed.; John Wiley & sons: Chichester, 1992; Vol. 1; pp 1-657.

55. NIST X-ray Photoelectron Spectroscopy Database, NIST Standard Reference Database Number 20, National Institute of Standards and Technology, Gaithersburg MD, 20899 (2000), doi:10.18434/T4T88K, (accessed December 20, 2017).

56. Pasquale, F. L.; Kelber, J. A. Site-Specific Electron-Induced Cross-Linking of Ortho-Carborane to Form Semiconducting Boron Carbide. *Appl. Surf. Sci.* **2012**, *258*, 2639-2642.

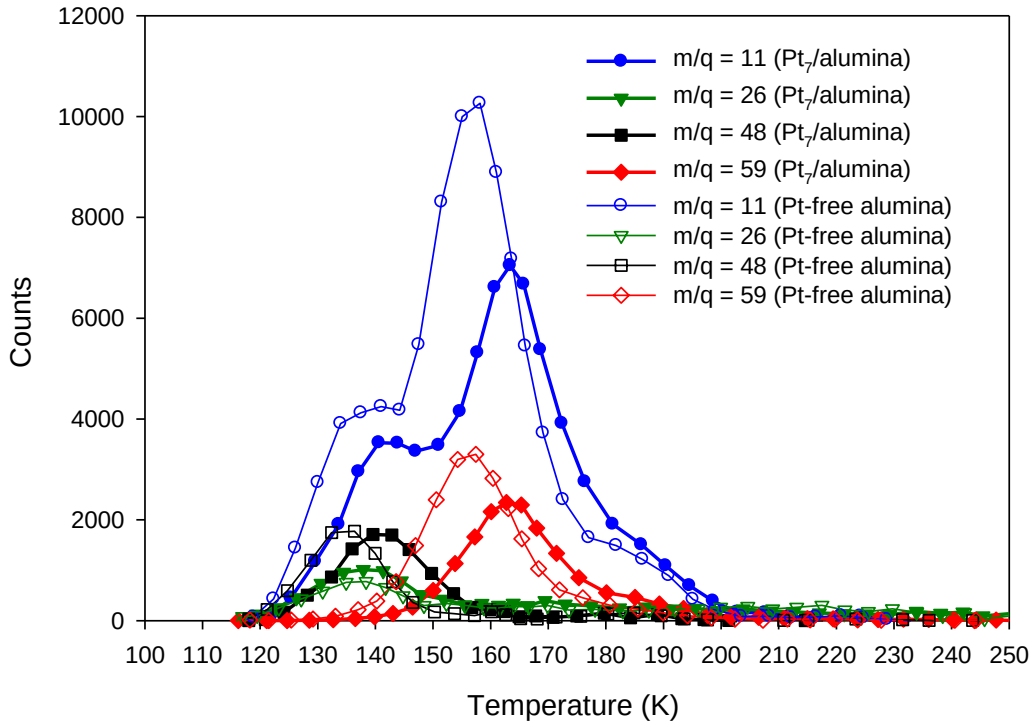

Figure 4.1: TPD spectra for select ion signals, corrected for EI cracking of borane species. Alumina and Pt_7/alumina samples were exposed to 1.5 L of diborane at 130 K, then heated at 3 K/sec while monitoring desorption mass spectrometrically.

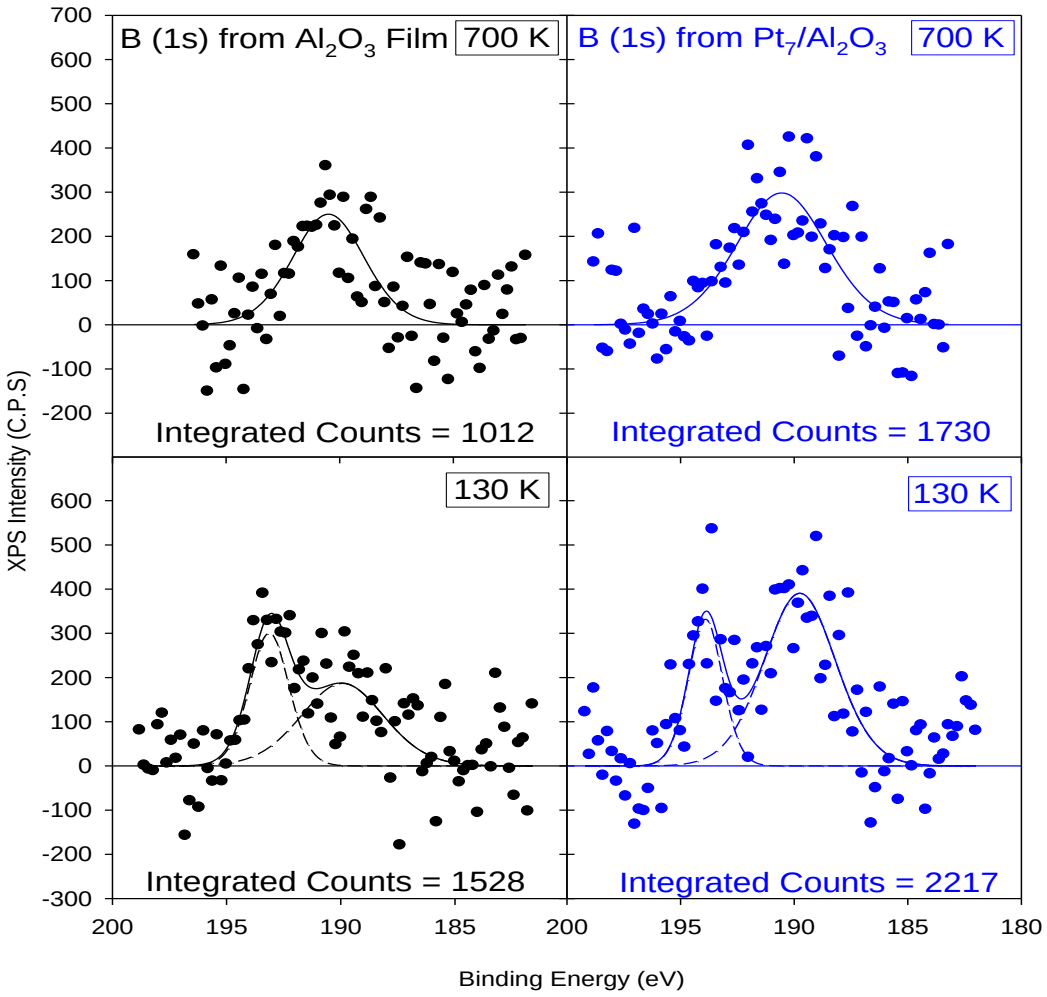

Figure 4.2: XPS spectra obtained for both Pt-free alumina (black) and Pt_7/alumina (blue) samples following exposure to 3 L of B_2H_6 at 130 K and after heating to 700 K.

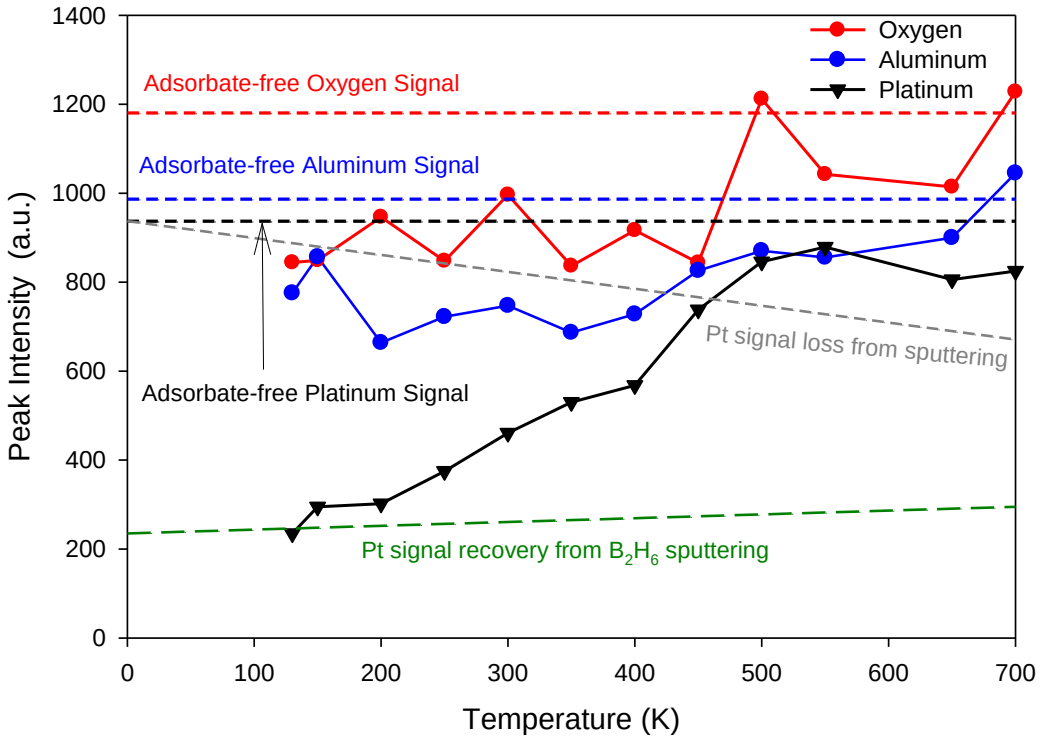

Figure 4.3: TD-ISS of Pt_7/alumina exposed to 1.5 K of diborane at 110 K. The intensities for adsorbate-free Pt_7/alumina, measured separately, are indicated as horizontal dashed lines. The effects of He^+ sputtering on Pt signal in adsorbate-free and diborane-dosed Pt_7/alumina held at 110 K are shown as dashed lines labeled "Pt signal loss from sputtering" and "Pt signal recovery from B_2H_6 sputtering," respectively.

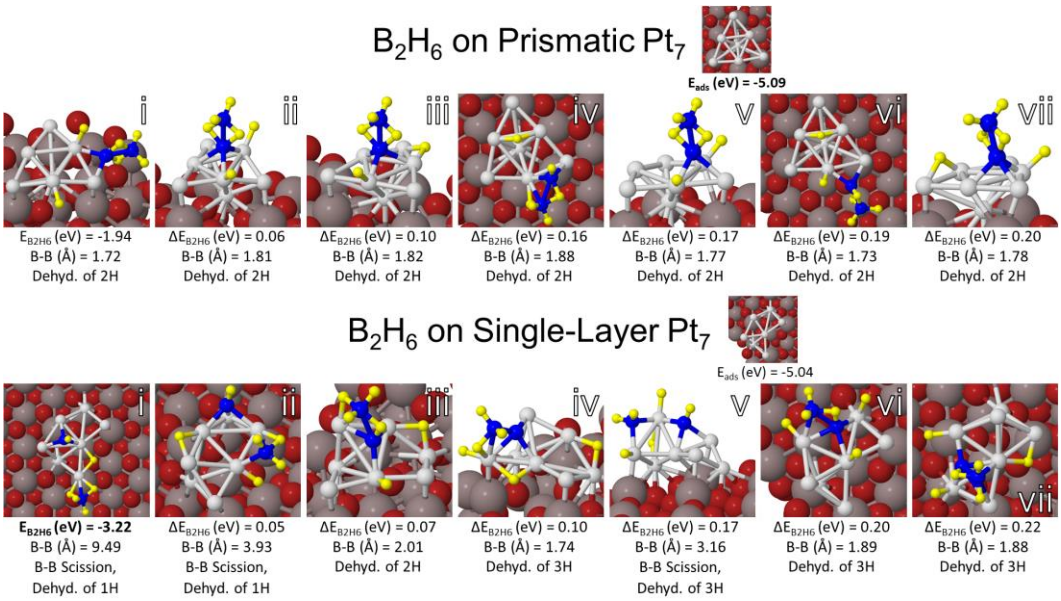

Figure 4.4: The seven lowest minima of diborane (B_2H_6) adsorbed on the two lowest minima of Pt_7, which also represent two different structural classes of Pt clusters, i.e., "prismatic" and "single-layer." The most stable adsorbate-free Pt_7/alumina isomer is prismatic, but with diborane adsorbed the single layer isomer becomes more stable by over 1 eV. Boron atoms are depicted in blue, platinum in light gray, hydrogen in yellow, aluminum in dark gray, oxygen in red.

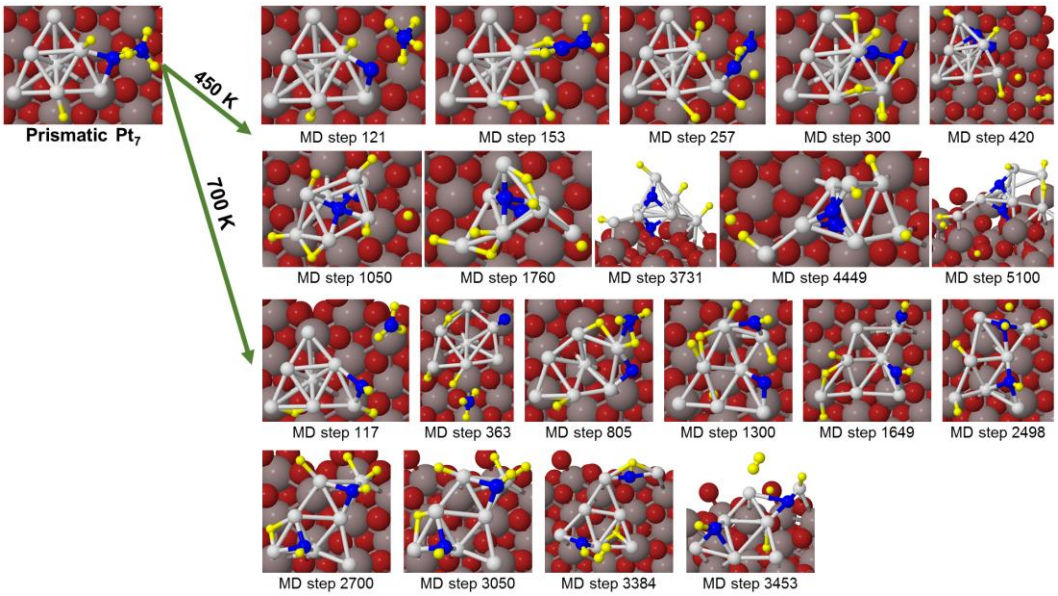

Figure 4.5: MD trajectories of diborane decomposition on prismatic Pt_7 reveal that diborane may either split apart to form a B-O_{surf} anchor or maximize Pt-B bonds by adsorbing onto a Pt cluster facet. The prismatic structure can also distort significantly or form a flattened, single-layer geometry. At 450 K, beyond 3.0 ps, the cluster changed very little with only the hydrogens translating from one atom to the next or H_2 diffusing through the vacuum gap. Each MD time step corresponded to 1 fs.

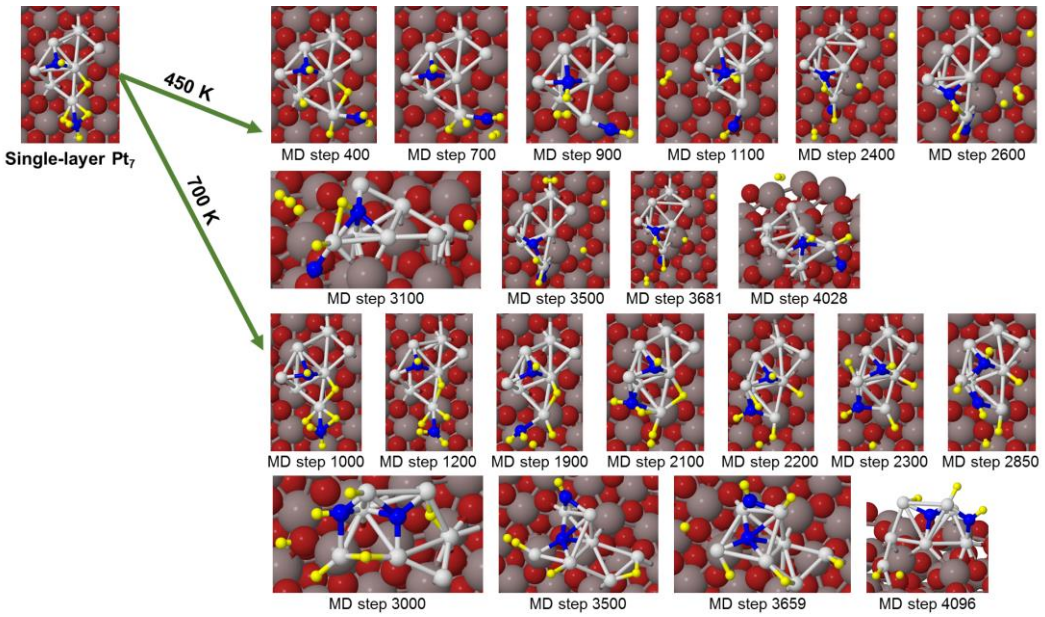

Figure 4.6: MD trajectories of the decomposition of diborane on single-layer Pt_7 reveal similar bonding trends to prismatic Pt_7. The stability of the single-layer structure observed in ground state calculations is retained during MD trajectories at these elevated temperatures of 450 and 700 K. At 450 K, MD steps >3100 resemble MD step 2600. Angled side views of the system at MD steps 3100 and 4028 were taken in order to highlight the B-O_{surf} anchor. Each MD time step corresponded to 1 fs.

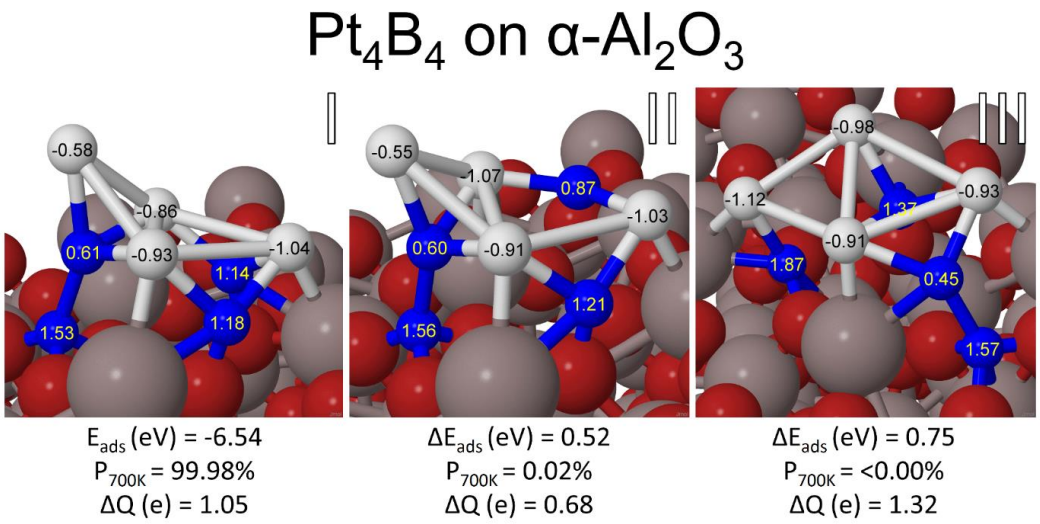

Figure 4.7: The three lowest minima of Pt_4B_4 adsorbed on alumina with their associated adsorption energies (E_{ads}), Boltzmann populations at 700 K (P_{700K}), and Bader charges on individual atoms. Boron atoms are depicted in blue, platinum in light gray, aluminum in dark gray, oxygen in red. Isomer II is very similar to Isomer I but with a B-O_{surf} anchor broken.

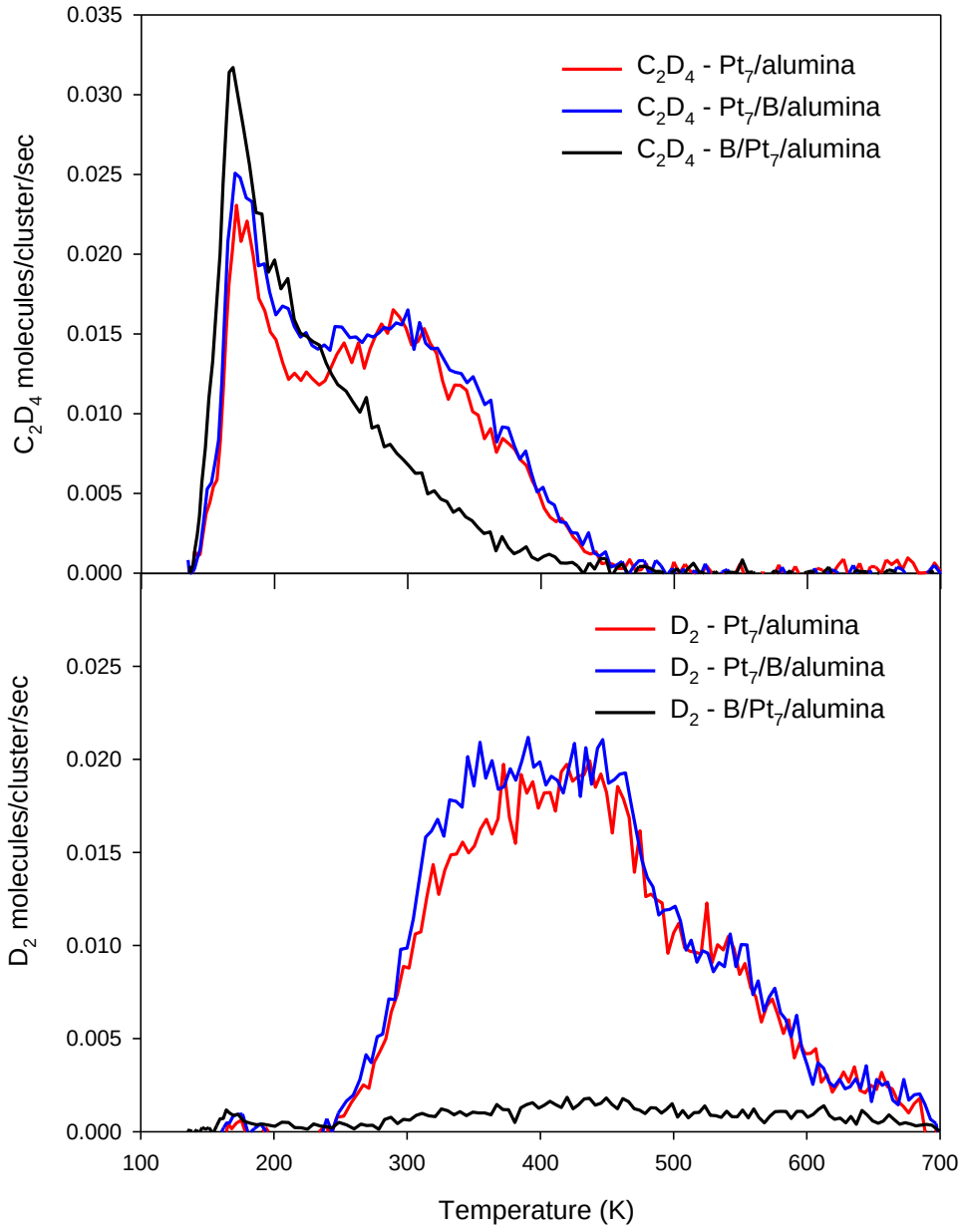

Figure 4.8: Thermal desorption spectra of unreacted ethylene and deuterium product obtained from three samples: (Red) As-deposited Pt_7/alumina with no boron exposure, (blue) Pt_7 deposited on pre-borated alumina, and (black) Pt_7/alumina borated after Pt_7 deposition. Each sample was exposed to 5 L C_2D_4 at 150K. Boration was done using our standard method (1.5 L B_2H_6 at 130 K, heating to 700 K). Separate samples were used for each experiment.

CHAPTER 5

CONCLUSION

The work presented in this dissertation has focused on fundamental studies of ethylene desorption and dehydrogenation on alumina-supported size-selected Pt_n model catalysts, and the effects of boron doping the clusters. In Chapter 2, we show that ethylene binds to the Pt_n clusters with a broad distribution of binding energies. The more strongly bound C_2D_4 decomposed to produce D_2, leading to deactivation of the catalyst through coking. Pt_7 was found to be significantly more active than both the deposited Pt_4 and Pt_8 clusters and also deactivated quicker. To fully understand the experimental results, we found that one must consider the ensemble of accessible cluster isomers and how it evolves with temperature and coverage.

In Chapter 3, we found that boron doping the Pt_n clusters shifted the distribution of ethylene binding to lower energies, therefore lowering the affinity for dehydrogenation. To further understand the results of borated clusters, we investigated the interactions between diborane and the Pt_7 clusters in Chapter 4. We found that exposing the Pt_7/alumina sample to diborane followed by heating resulted in the preferential deposition of boron atoms onto the Pt clusters. Furthermore, we found that that the much smaller boron coverage on the alumina film had no effect on the ethylene binding/dehydrogenation on the Pt clusters. Therefore, we can attribute the decrease in ethylene binding/dehydrogenation to the boration of the Pt clusters. Additionally, the Pt-bound boron was found by DFT, in agreement with TD-ISS, to move to sites beneath the Pt clusters, forming Pt-B-O_{surf} bonds that anchor the clusters to the support.

The implication from this study is that using a catalytic reaction to seed deposition of a second element may be a useful strategy to selectively modify a catalyst in a beneficial way. For example, we observed that boron deposited on Pt clusters (by

exposure to diborane and heating) reduced the ethylene binding energy, thereby reducing the tendency to undergo dehydrogenation to coke precursors. This approach could be used to coat the fuel lines of supersonic aircrafts with a coke resistant catalytic material that could assist in increasing the available heat sink. The results from this study may be broadly valuable since coking is one of the major mechanisms for deactivation of industrial catalyst.

This study raises a number of opportunities for future research. Dehydrogenation of an alkane to an alkene is the overall goal of the catalyst in hypersonic vehicles and needs to be investigated for the boron doped Pt cluster catalyst. The strategy for producing bimetallic cluster catalysts to tune selectivity could also be investigated for a number of important catalytic materials.

APPENDIX A

SUPPORTING INFORMATION FOR CHAPTER 2

A.1 TPD Fitting Method and Results

A distribution of population in sites with different energies for desorption/dehydrogenation, θ(E), is assumed, and then the TPD/R spectra are fit using the first order rate equation:[1]

$$I(t)\ \alpha\ \frac{-d\theta}{dt} = (\theta(E)\cdot\ \nu)\ e^{\frac{-E}{kT(t)}},$$

where I(t) is the desorption as a function of time, ν is a prefactor and T(t) is the temperature as a function of time. θ(E) is adjusted until the simulated I(t) matches the experiment. Because size-selected cluster samples are time consuming to prepare, and irreversibly changed by a single TPD/TPR run, it is simply not practical to extract ν from a series of coverage-dependent experiments on every cluster size. Therefore, the simulations were tested for ν ranging from 10^{13} to 10^{15} s^{-1}, covering a range often found in TPD.[2] The simulated desorption/dehydrogenation energies shift by only ~7% *per* order-of-magnitude variation in ν, and in Figure A.3 we present the θ(E) distributions obtained for ν = 10^{14} s^{-1}.

A.2 ISS Extrapolation Method

Figure S5 shows the normalized Pt ISS intensity as a function of He^+ exposure in a sequence of low He^+ flux (0.1 μA) ISS measurements. The increase in Pt signal during the initial measurements is evidence of a small coverage of adventitious adsorbates (CO and H_2O as determined by separate TPD measurements) that had adsorbed onto the clusters during the ~ 15 min cluster deposition time. The initial increase in Pt signal is a result of the adsorbates being sputtered off the cluster to expose the underlying Pt to He^+ scattering. The Pt signal eventually reaches a maximum and begins to decrease due to Pt sputtering.

To determine the as-deposited value the Pt intensity is extrapolated back to the limit of zero He^+ exposure and zero adsorbate coverage as shown by the fit in Figure A.5.

A.3 Pt_4 CO TD-ISS

Figure A.6 shows the results from a $^{13}C^{16}O$ TPD and a TD-ISS experiment performed in our group by F. Sloan Roberts and Matthew Kane on the Pt_4/alumina/Re(0001) system. The $^{13}C^{16}O$ TPD (blue) measurement was collected by exposing a freshly prepared Pt_4/alumina/Re(0001) sample with 10 L of $^{13}C^{16}O$ at a 180 K. The sample was allowed to cool to 140 K before heating the sample at a rate of 3 K/sec while detecting the amount of $^{13}C^{16}O$ desorbing from the surface.

The TD-ISS measurements were collected by exposing a separately prepared Pt_4/alumina/Re(0001) sample to 10 L of $^{13}C^{16}O$ at 180 K and colleting an ISS spectrum with a single low He^+ flux (0.1μA) scan. The succeeding points in the TD-ISS curve were collected by heating the sample in 50 K increments and measuring the ISS spectrum at the indicated temperatures. The loss of Pt signal due to sputtering, the recovery of Pt signal due to removal of $^{13}C^{16}O$, and the as-deposited Pt signal are represented by sloping dashed lines and were determined on separately prepared samples using the same procedure that was used for Figure 2.2.

From the TPD results, heating the sample to 350 K desorbs ~35 % of the total $^{13}C^{16}O$ coverage but results in an insignificant recovery in the Pt ISS signal. As the sample is heated from 350 to 650 K there is a sharp recovery of the Pt ISS signal as the remaining $^{13}C^{16}O$ coverage desorbs. These results suggest that the weakly bound $^{13}C^{16}O$ that is desorbed at temperatures < 350 K is bound in sites that are inefficient at blocking or

shadowing the He^+ from scattering off the Pt, such as around the periphery of the cluster. On the other hand, the $^{13}C^{16}O$ desorbed at temperatures above 350 K leads to a strong recovery of the Pt ISS signal suggesting it desorbs from sites that efficiently attenuate the signal, such as on top sites.

A.4 Theoretical Methods - Details

The relevant equations regarding formation (E_{form}), adsorption (E_{ads}), and sintering energies (E_s) are described in the following. E_{form} is VASP's DFT energy of the gas phase cluster with the component, atomic energies already subtracted. The atomic energies arise from the calculated energies of the elements from which the pseudopotential was generated.

$$E_{ads}[Pt_n] = E[Surf+Pt_n]-E[Surf]-Egas,min[Pt_n],$$

where E [Surf + Pt_n] is the total DFT energy of the supported cluster system, E[Surf] is the total energy of the bare support, and $E_{gas,min}$[Pt_n] is the global minimum of the gas-phase cluster.

An analogous equation to E_{ads} for reagent species (*reag*) such as ethylene and C (a single carbon atom is used as a first-order approximation to coking) is detailed below:

$$E_{reag} = E[Surf+Pt_n+reag]-E[Surf+Pt_n]-E_{reag},$$

where $E[Surf+Pt_n+reag]$ is the total DFT energy of the supported cluster system with the reagent species and E_{reag} is the total energy of the gas-phase cluster. In coverage calculations of ethylene, E_{reag} will encompass the $n \times E_{ethyl}$, where E_{ethyl} is the energy of ethylene in the gas-phase.

Statistical analysis is performed through use of the Boltzmann probability for *i*-th

configuration (P_i) by taking the Boltzmann distribution of each minimum (e^{-E_i/k_BT}) divided by the sum of the distributions of all relevant low energy minima:

$$\mathrm{P_i} = \frac{e^{-E_i/k_BT}}{\sum e^{-E_i/k_BT}},$$

where E_i is the *i*-th configuration energy of a gas phase cluster (i.e., E_{form} as defined above), adsorbed cluster *(E[Surf+Pt_mB_n])* or adsorbed cluster with a reagent *(E[Surf+Pt_n+reag])*, k_B is the Boltzmann constant, and T is the temperature.

The entropic contribution of relevant minima may also be found by considering the fundamental thermodynamic relation of the Helmholtz free energy ($F = U - TS$). Specifically, the Gibbs' entropy equation (S_G) allows us to analyze the effect of discrete states with their respective Boltzmann probabilities on the ensemble of particular cluster types:

$$S_G = -k_B \sum_i P_i \, ln(P_i),$$

where the P_I are the Boltzmann weights and k_B is the Boltzmann constant. In this way, we may analyze the entropic contribution at a catalytically relevant temperature (TS_G).

In the gas phase, the septamer and octamer contain many isomers whose energies are within 0.2-0.3 eV of the most stable geometry (Figure A.9).[3,4] The gas phase isomers present a mixture of 2D and 3D geometries. Adsorbed structures were formed from the deposition of the lowest 5-6 gas phase structures, with a thorough sampling of cluster faces to possible binding sites. The complexity of the corrugated alumina surface leads to a combination of Pt-Al and Pt-O coordination so that single-layer gas phase isomers crinkle in order to maximize wetting of the surface (observed in Pt_7, Isomer II, Main text Fig. 2.1). As the surface is Al-terminated, Pt coordinating to electropositive Al gains a negative charge. Likewise, Pt-O coordination yields positively charged Pt so that a single cluster

features a range of electronic depletion or augmentation from one atom to the next. These atomic charges (Δq) are visualized in the main text's Fig. 2.1. The charge separation between atoms yields an electrostatic potential that further stabilizes clusters and attenuates their site reactivity.

There is an apparent switch in dimensionality between Pt_7 to Pt_8, where Pt_7 on average features more open geometries that wet the corrugated support. The adsorbed Pt_7 clusters feature a prismatic geometry (ΣP_{700K} = 66.67%, Isomers I and IV) and a single-layer geometry (ΣP_{700K} = 33.33%, Isomers II, III, and V). This mix of structures offers a complex and rich set of binding sites for adsorbates. In contrast, all of the isomers of Pt_8 are prismatic. In prismatic structures, some of the Pt atoms are buried inside the cluster, becoming unavailable as binding sites. These results are in agreement with the experimental findings that suggest that Pt_7 provides more binding sites for ethylene as compared to Pt_8. Additionally, there is a greater uniformity in the nature of the exposed binding sites, as can be judged by their partial charges. The septamer optimizes the cluster-support interactions with a relatively high charge transfer ($\Delta Q > -1.20$ e) in the global minimum, and, unsurprisingly, features the most favorable adsorption. The added negative charge does not distribute uniformly over the cluster; instead, there is a polarization of Pt atoms in Pt_7. Pt_8 preserves the charge transfer behavior of Pt_7, but adsorption to the support is weaker: of the global minimum of Pt_8, $Pt_{8,glob}$, it is 0.2 eV weaker than that of $Pt_{7,glob}$. The Pt atoms within $Pt_{8,glob}$ are charged more uniformly (details in Table A.4).

A.5 References

1. Redhead, P.A. *Vacuum*, **1962**, 12, 203–211

2. Kaden, W.E.; Kunkel, W.A.; Roberts, F.S; Kane, M.; Anderson, S.L. *J. Chem. Phys.*, **2012**, 136, 204705

3. Zhai, H.; Ha, M.; Alexandrova, A. N. J. *Chem. Theor. Comput*. **2015**, 11, 2385-2393.

4. Tian, W. Q.; Ge, M.; Sahu, B.; Wang, D.; Yamada,T.; Mashiko, S. *J. Phys. Chem. A* **2004**, 108, 3806-3812.

Table A.1: Formation energies of global minima of Pt_7, Pt_8

	Pt_7	**Pt_8**
E_{form} (eV)	-27.05	-31.97
E_{form}/atom (eV)	-3.86	-4.00

Table A.2: Gas phase isomers

Cluster	**Isomer**	**Δ E_{form} (eV)**	$P_{450\ K}$	$P_{1000\ K}$
Pt_7	I	0.00	75.60%	47.39%
	II	0.05	19.85%	25.97%
	III	0.13	2.63%	10.45%
	IV	0.17	0.99%	6.75%
	V	0.19	0.60%	5.38%
	VI	0.21	0.32%	4.06%
Pt_8	I	0.00	56.98%	38.31%
	II	0.03	24.95%	26.42%
	III	0.06	13.66%	20.15%
	IV	0.10	4.31%	11.99%
	V	0.26	0.06%	1.81%
	VI	0.29	0.03%	1.33%

Table A3. Gas phase isomers under def2/TZVPP basis with pure and hybrid functionals calculated in TURBOMOLE V6.6

Cluster	Isomer	Δ E_{form} (eV), Multipl-icity	Δ E_{form} (eV), Multipl-icity	Δ E_{form} (eV), Multipl-icity	Δ E_{form} (eV), Multipl-icity	Δ E_{form} (eV), Multipl-icity
		VASP	**TM/PBE**	**TM/PBE0**	**TM/TPSS**	**TM/TPSSh**
Pt_7	I	0.00	0.00, 5	0.86, 5	0.34, 5	0.65, 5
	II	0.05	0.15, 5*	0.36, 5, I	0.18, 5	0.32, 5, I
	III	0.13	0.01, 5	0.00, 5	0.00, 5	0.00, 5
	IV	0.17	0.20, 5, I	0.72, 5	0.40, 3*	0.71, 3
	V	0.19	0.05, 5	0.31, 5, I	0.10, 5	0.15, 5
	VI	0.21	0.20, 5*	0.40, 5, I	0.26, 5*	0.16, 5

* geometries had difficulty converging, I = geometries with an imaginary frequency

Table A.4: Adsorbed isomers of Pt_7, Pt_8 with Boltzmann populations (P) at experimentally relevant temperatures of 450 and 1000 K and charge transfer (ΔQ) from the support

Cluster	Isomer	Δ E_{ads} (eV)	$P_{450\ K}$	$P_{700\ K}$	ΔQ (e)
Pt_7	I	0.00	75.27%	65.89%	-1.22
	II	0.04	24.49%	32.02%	-1.44
	III	0.24	0.16%	1.26%	-1.33
	IV	0.27	0.07%	0.77%	-1.25
	V	0.43	<0.01%	0.05%	-1.23
	$\Sigma P_T E_{ads}$ (eV)		-5.08	-5.07	
	TS_G (eV)		0.010	0.019	
Pt_8	I	0.00	97.65%	87.73%	-1.24
	II	0.17	1.14%	5.03%	-1.07
	III	0.19	0.74%	3.82%	-0.94
	IV	0.21	0.41%	2.61%	-1.08
	V	0.30	0.04%	0.57%	-1.22
	VI	0.39	<0.01%	0.14%	-1.08
	VII	0.41	<0.01%	0.10%	-0.80
	$\Sigma P_T E_{ads}$ (eV)		-4.89	-4.87	
	TS_G (eV)		0.002	0.009	

Table A5. Local minima of adsorbed ethylene on Pt_7 (Isomer I and II)

Ads.	Con-fig.	$\Delta E_{ethylene}$ (eV)	$P_{450\ K}$	$P_{700\ K}$	$\Delta Q_{et-hylene}$ (e)	Hyb-rid.	C-C Bond Lengt-hs (Å)	Bond Angles (°)
Pt_7, Isomer I	i	0.00	86.93%	72.48%	0.00	sp2	1.41	115.4–120.5
	ii	0.10	7.35%	14.81%	-0.07	sp3	1.49	100.6–114.9
	iii	0.11	5.72%	12.59%	0.00	sp2	1.40	116.0–120.5
	iv	0.38	<0.01%	0.13%	-0.16	sp3	1.49	99.7–115.4
	v	0.79	<0.01%	<0.01%	-0.10	sp3	1.50	97.5–114.9
	vi	0.87	<0.01%	<0.01%	-0.02	sp3	1.51	100.6–113.9
Pt_7, Isomer II	i	0.00	99.64%	96.30%	0.01	sp2	1.42	115.0–120.5
	ii	0.24	0.22%	1.90%	-0.01	sp2	1.41	114.6–121.0
	iii	0.26	0.12%	1.26%	-0.05	sp3	1.49	97.5–115.9
	iv	0.34	0.02%	0.36%	-0.03	sp2	1.42	114.8–120.4
	v	0.39	<0.01%	0.15%	-0.03	sp2	1.42	115.3-120.4
	vi	0.49	<0.01%	0.03%	-0.05	sp3	1.50	100.4–115.5

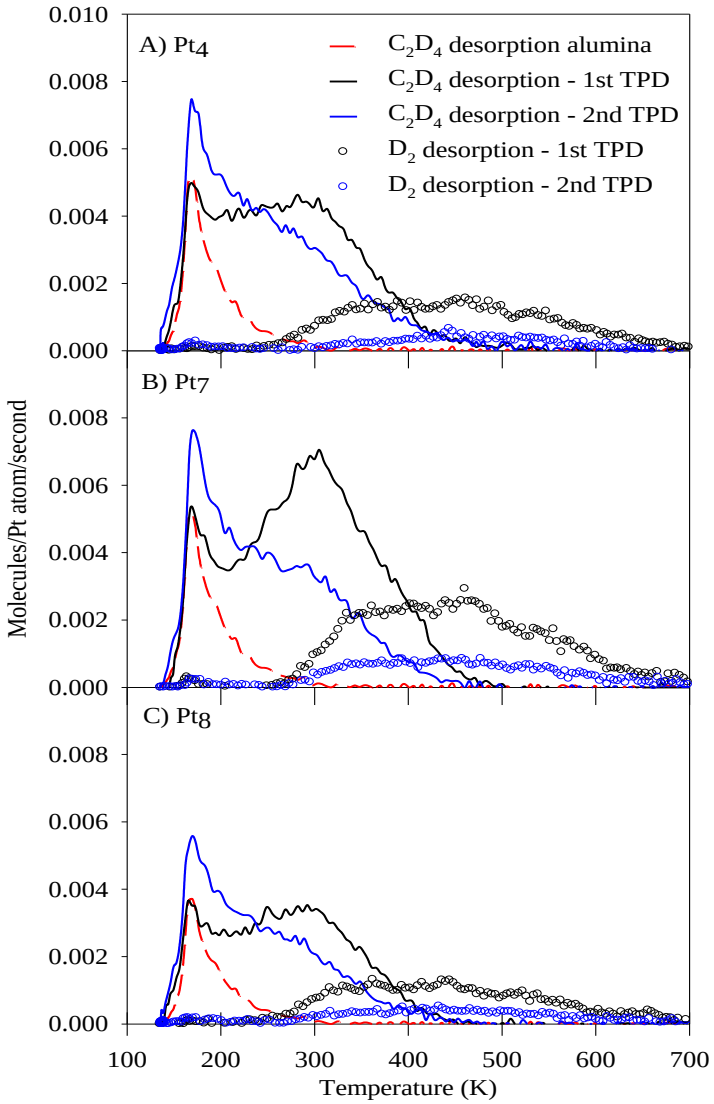

Figure A.1: Intact C_2D_4 (solid) and D_2 (circles) desorbing from Pt_n/alumina/Ta(110) (n=4,7,8) sample during two consecutive TPD measurements. Intact C_2D_4 (red dashed line) desorbing from a cluster free alumina/Ta(110) sample. All samples were exposed to 5 L of C_2D_4 at 150 K before starting the TPD measurement. The D_2 signal has not be corrected for the amount of D_2 produced from the fragmentation of C_2D_4 caused by electron impact ionization.

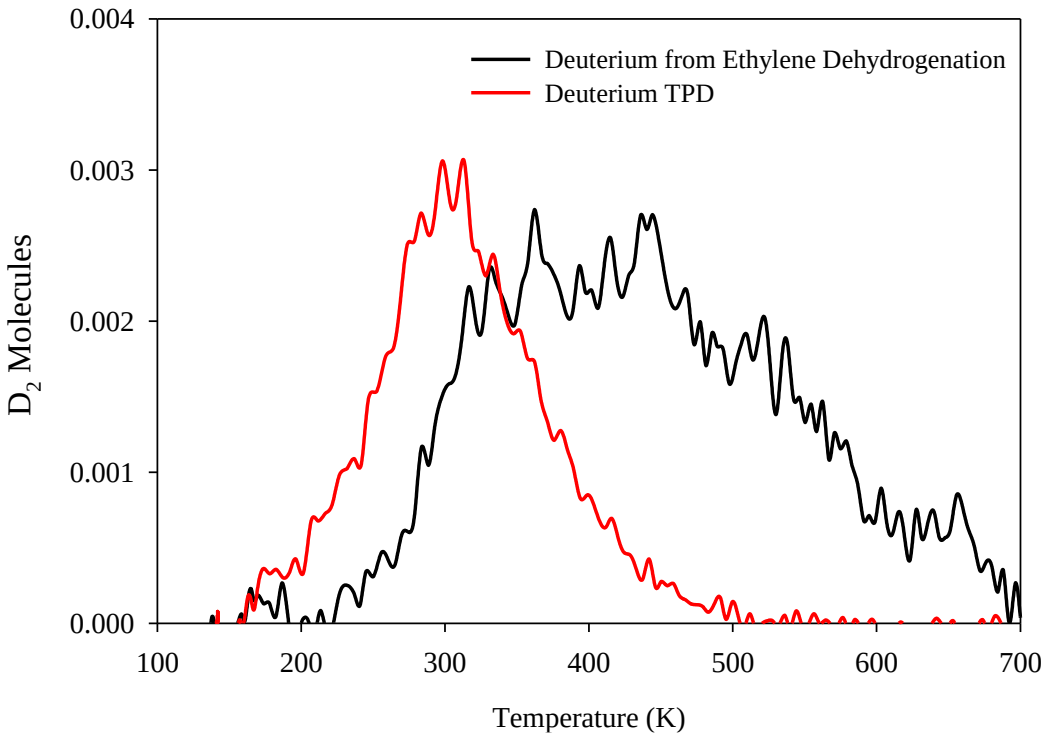

Figure A.2: D_2 desorbing from Pt_8/alumina/Ta(110) after exposing the sample to 5 L of D_2 at 150 K (red). D_2 produced by C_2D_4 dehydrogenation during a C_2D_4 TPD/R measurement (black).

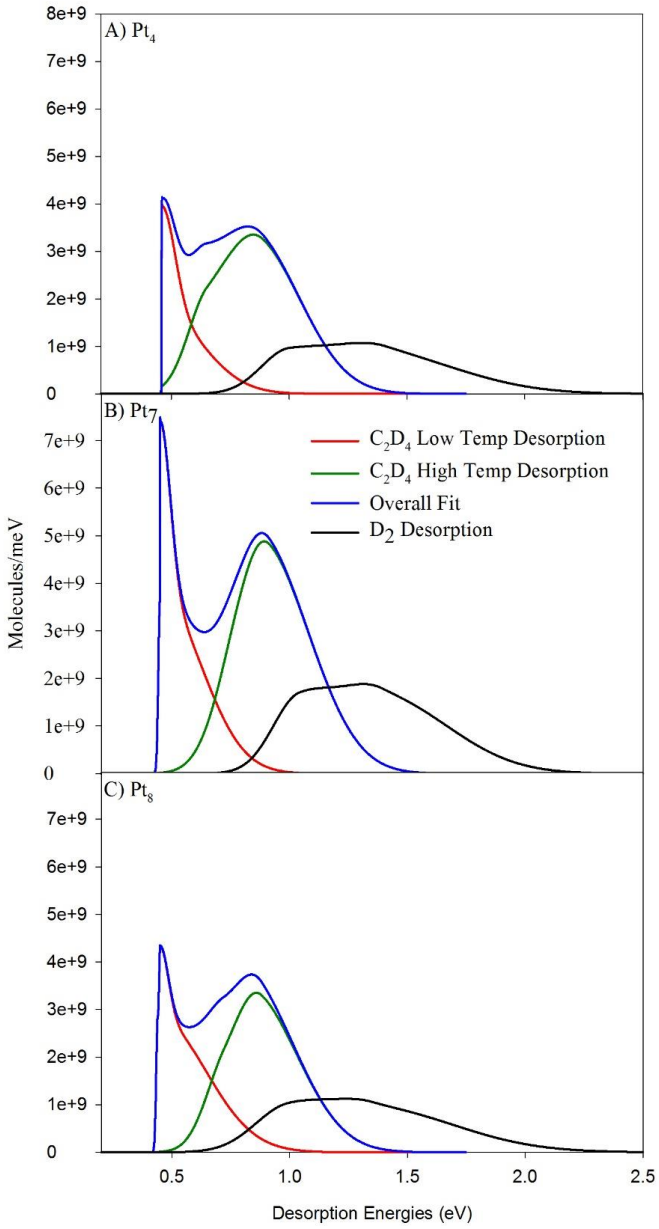

Figure A.3: Energy of desorption fits for C_2D_4 and D_2 desorbing during the first C_2D_4 TPD/R experiments for Pt_4, Pt_7, and Pt_8.

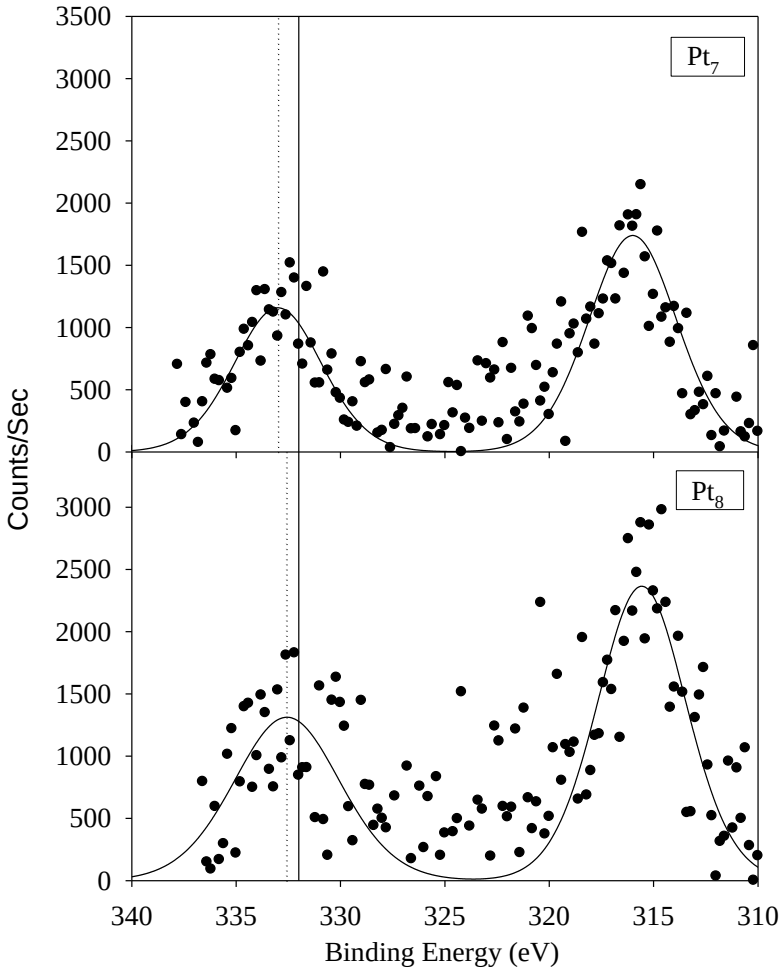

Figure A.4: Pt 4d XPS for Pt_7 and Pt_8, as-deposited on alumina/Ta(110).

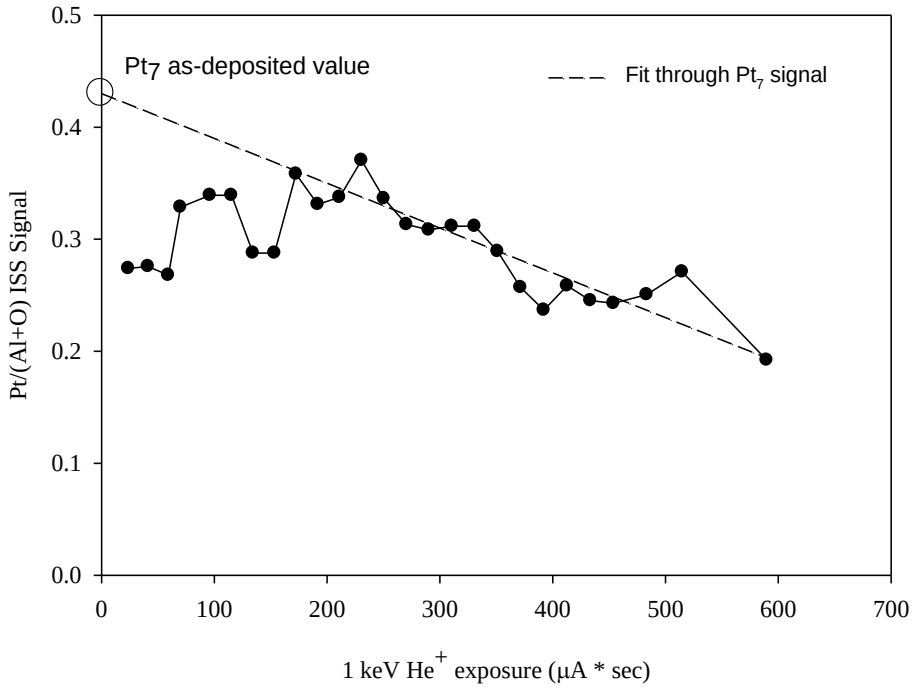

Figure A.5: Normalized Pt intensity for Pt_7 as a function of He^+ exposure during a sequence of low He^+ flux (0.1 μA) ISS scans. The as-deposited value of the Pt intensity can be determined by extrapolating back to the limit of zero exposure and adsorbate coverage as shown by the fit.

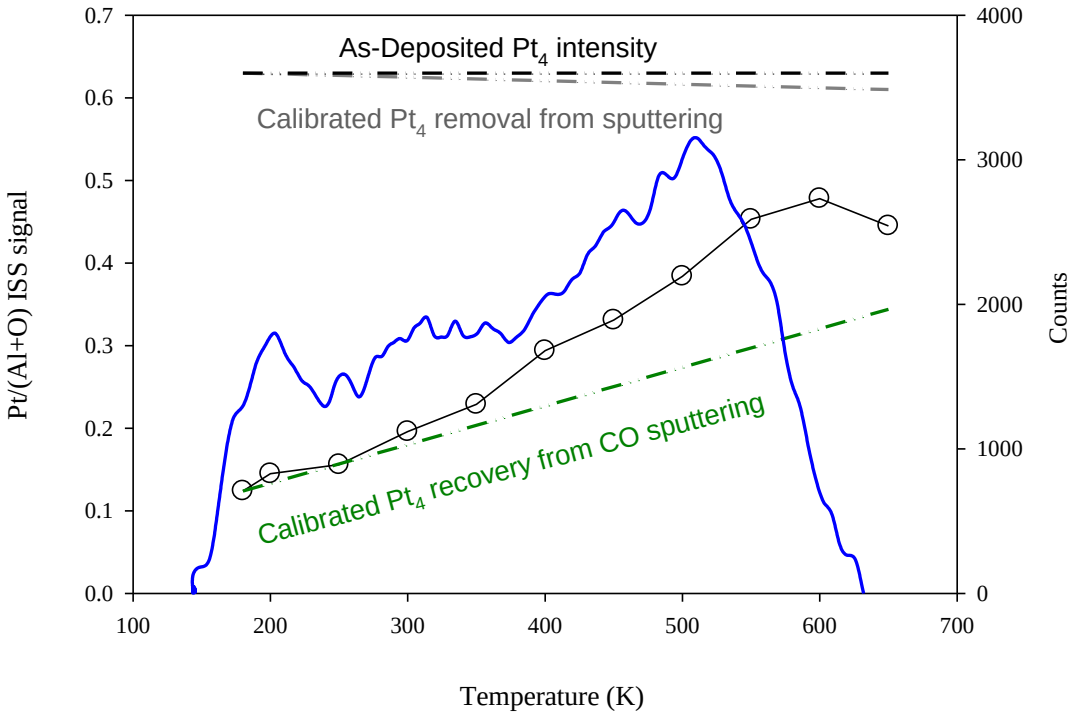

Figure A.6: Pt/(Al+O) ISS signal as function of temperature (circles) after exposing the sample with 10 L of $^{13}C^{16}O$ at 180 K. CO desorbing from a separately prepared Pt_4/alumina/Re(0001) sample exposed to 10 L of $^{13}C^{16}O$ at 180 K during the first TPD measurement (blue). Both samples contained a 0.1 ML of deposited Pt_4 clusters.

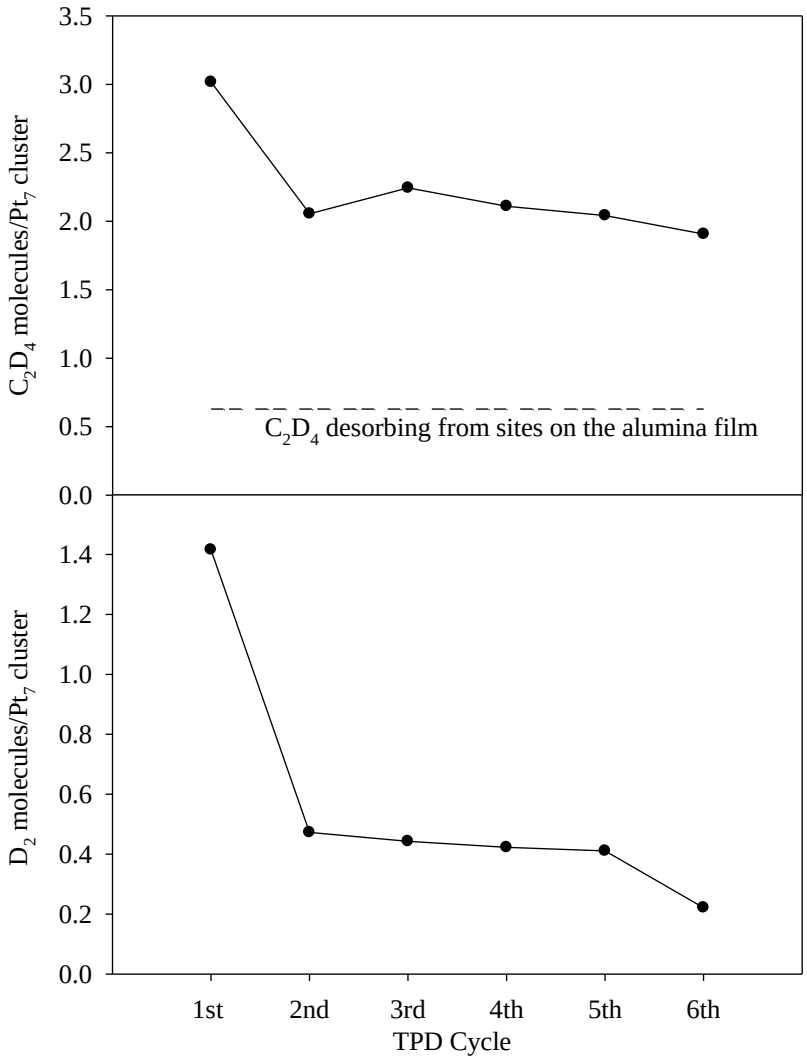

Figure A.7: Integrated amounts of C_2D_4 (top) and D_2 (bottom) desorbing, *per* deposited Pt_7 cluster, during a sequence of 6 TPD/R runs under the conditions used in Fig. 2.2 The dashed horizontal line gives an estimate for the C_2D_4 desorbing from alumina sites, taken from the integrated desorption measured for cluster-free alumina.

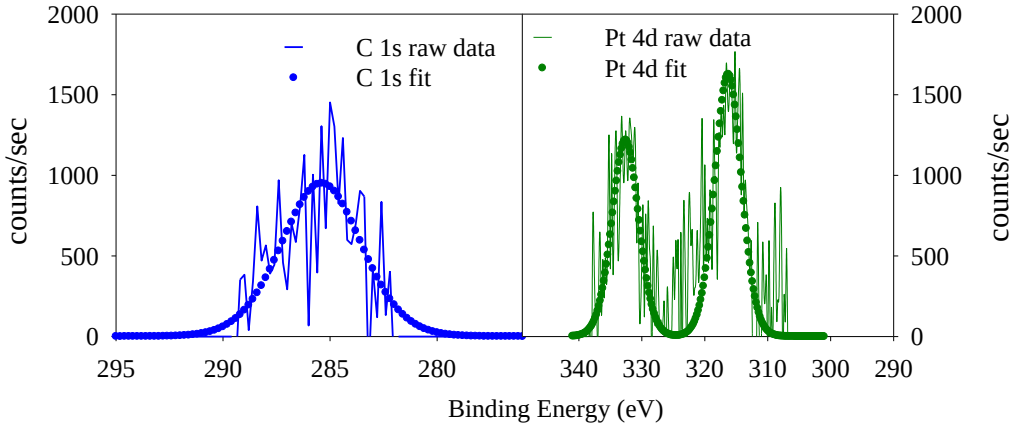

Figure A.8: C 1s and Pt 4d peaks measured by XPS after 6 consecutive TPD cycles on a Pt_7/alumina sample. The presence of carbon suggest that dehydrogenation of ethylene leads to the deposition of carbon onto the model catalyst.

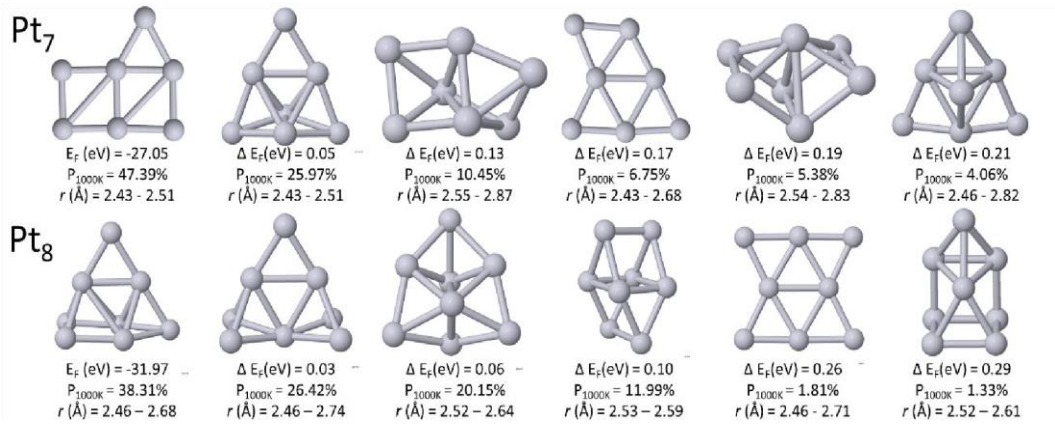

Figure A9: Gas phase isomers of Pt_7, Pt_8 at catalytically relevant temperature of 1000K.

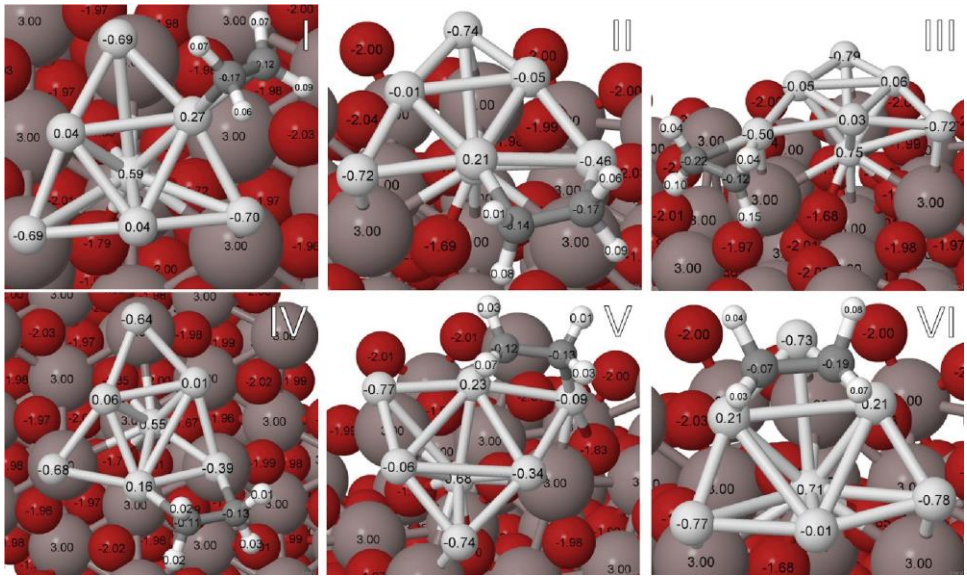

Figure A.10: The lowest minima of ethylene adsorbed on $Pt_{7,\,glob}$, with calculated Bader charges.

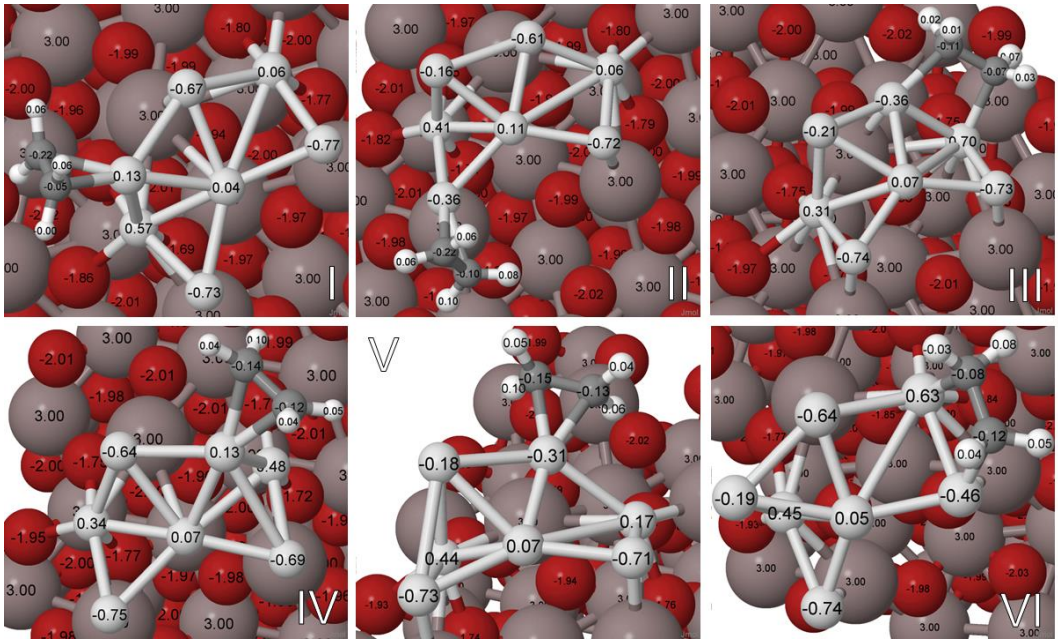

Figure A.11: The lowest minima of ethylene adsorbed on the second lowest minimum of adsorbed Pt_7, with calculated Bader charges.

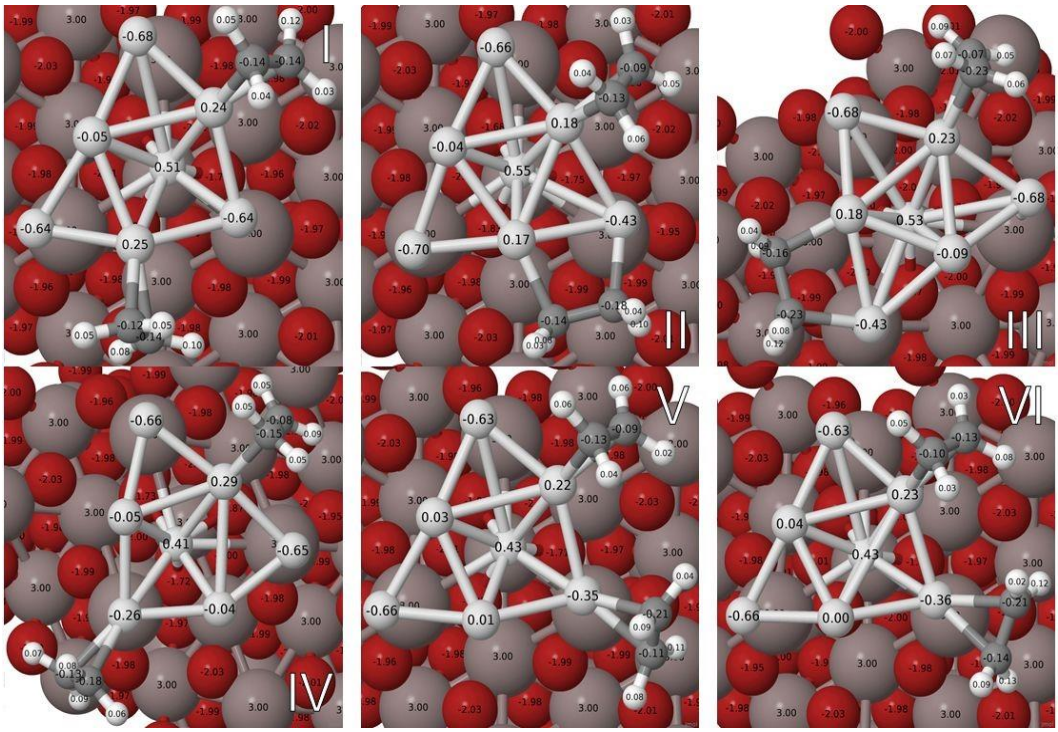

Figure A.12: The lowest minima of 2 ethylene adsorbed on the Pt_7, Isomer I (the global minimum).

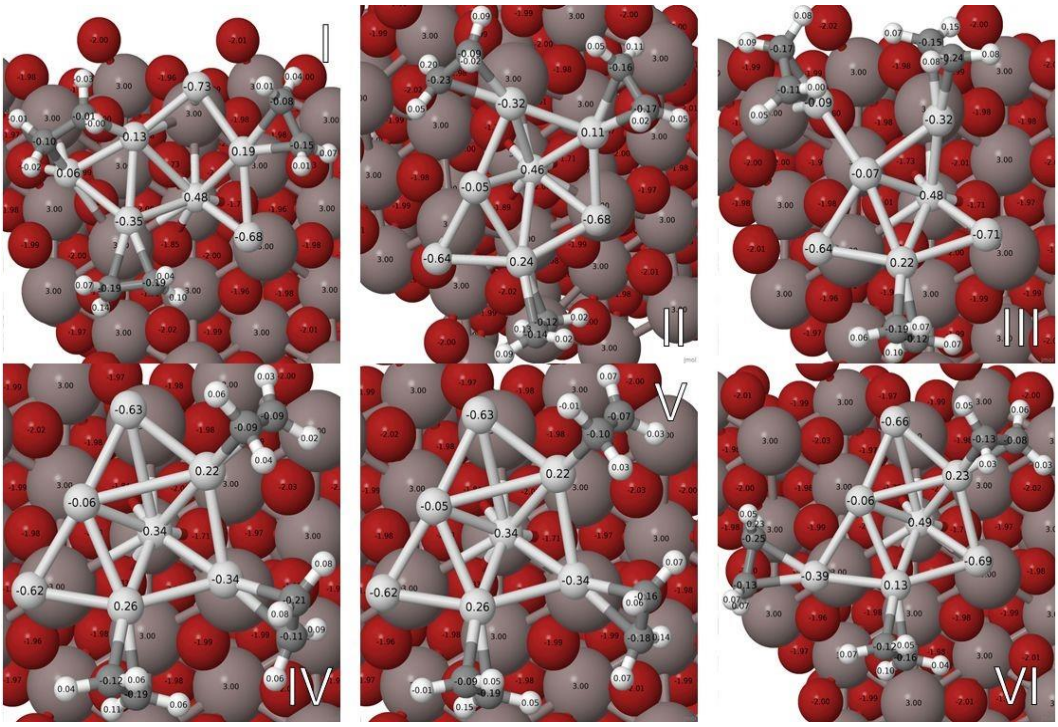

Figure A.13: The lowest minima of 3 ethylene adsorbed on the Pt7, isomer I (the global minimum).

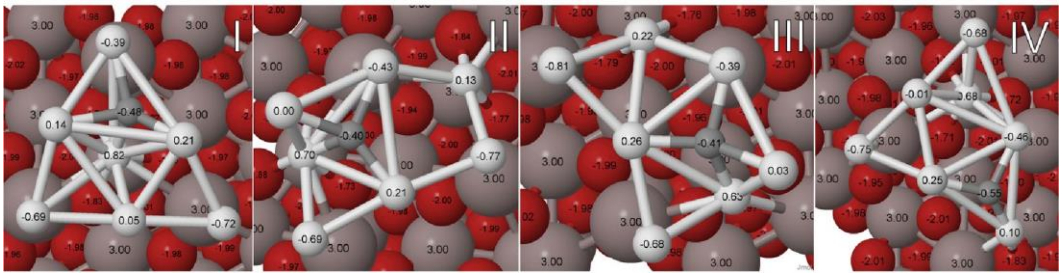

Figure A:14: The C-sticking configurations of the lowest four isomers of Pt_7, with calculated Bader charges.

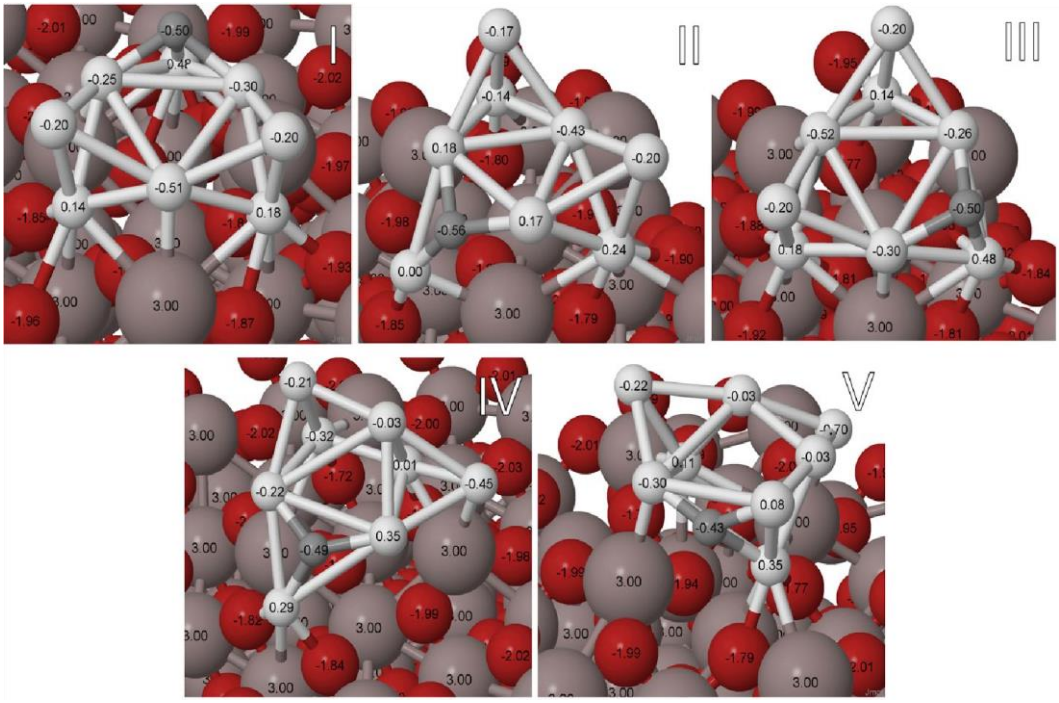

Figure A.15: The C-sticking configurations of the lowest five isomers of Pt_8, with calculated Bader charges.

APPENDIX B

SUPPORTING INFORMATION FOR CHAPTER 3

B.1 Experimental discussion

Further discussion of Fig. 3.2 in the main text: A small amount of CO is seen desorbing from the alumina film at low temperatures, presumably from defect sites in the alumina film. However, strong bimodal desorption of CO from the as-deposited Pt7/alumina is seen, which we attribute to CO desorbing from sites related to the Pt cluster. Heating the sample to 700 K results in a small attenuation in high temperature desorption component and a small increase in the low temperature desorption component. Exposing the sample to 1.5 L of B2H6 and heating it to 300 K prior to the CO TPD resulted in the amount of CO desorbing at temperatures above ~350 K to decrease by 70%, presumably from a combination of cluster restructuring and site blocking from residual boron species left on the cluster. Heating the sample to 700 K following the 1.5 B2H6 exposure resulted in a small loss of CO desorption in the 300-400 K range. Further discussion of Fig. 3.3 in the main text: Simply heating Pt7/alumina to 300 K results in a ~38% decrease in the amount of C2D4 desorbing from Pt sites above 200 K (1.3 C2D4/Pt7), and also a ~28% reduction in the amount D2 production (1.0 D2/Pt7). Heating to 700 K has no further effect on C2D4 desorption above ~300 K, but results in a significant increase in desorption at lower temperatures, such that the total C2D4 desorption (1.9/Pt7) is only ~10% below that for as-deposited Pt7/alumina. D2 production (1.3/Pt7) recovers nearly to the as-deposited value, but shifts to slightly lower temperatures. These effects are attributed to a combination of thermal changes to the cluster morphology, and desorption at temperatures above 300 K, of the small amount of adventitious CO present on the as-deposited Pt7,[1] consistent with the ISS results in Figure 3.1.

B.2 Additional Theoretical Methods

The relevant equations regarding formation (E_{form}), adsorption (E_{ads}), and sintering energies (E_s) are described in the following. E_{form} is VASP's DFT energy of the gas phase cluster with the component, atomic energies already subtracted. The atomic energies arise from the calculated energies of the elements from which the pseudopotential was generated.

$$E_{ads}[\mathrm{Pt_7B}] \;=\; E[\mathrm{Surf} + \mathrm{Pt_7B}] - E[\mathrm{Surf}] - E_{gas,min}[\mathrm{Pt_7B}],$$

where E [Surf +$\mathrm{Pt_7B}$] is the total DFT energy of the supported cluster system, E[Surf] is the total energy of the bare support, and $E_{gas,min}[\mathrm{Pt}_m\mathrm{B}_n]$ is the global minimum of the gas-phase cluster. Table B.3 lists the adsorption energies of the global minima of adsorbed clusters as well as the sintering energy penalty, that is, the energy cost of an atom of a given element to break away from an octomer, forming a septamer and a monomer on the support:

$$E_s[Pt_7B - B] = \; E[Surf + Pt_7] + E[Surf + B_1] - E[Surf + Pt_7B] - E[Surf]$$

$$E_s[Pt_8 - Pt] = \; E[Surf + Pt_8] + E[Surf + Pt_1] - E[Surf + Pt_7] - E[Surf].$$

In Table B.3, the sintering energy penalty refers to the monomer energy $E[\mathrm{Surf} + \mathrm{Pt/B_1}]$ in the most favorable position on the support from potential energy surface (PES) calculations. Our PES utilized a fine 10 × 10 grid on a sample unit of our (3 × 3) surface.

An analogous equation to E_{ads} for reagent species (*reag*) such as diborane, ethylene, and C (a single carbon atom is used as a first-order approximation to coking) is detailed below:

$$E_{reag} \;=\; E[\mathrm{Surf} + \mathrm{Pt_7B} + reag] - E[\mathrm{Surf} + \mathrm{Pt_7B}] - E_{reag}$$

where $E[\mathrm{Surf} + \mathrm{Pt}_m\mathrm{B}_n + reag]$ is the total DFT energy of the supported cluster system with the reagent species and E_{reag} is the total energy of the gas-phase cluster. In coverage calculations of ethylene, ethylene adsorption reflected our method of sequential adsorption:

$$E_{2\ ethylene} = E_{2\ ethylene+glob,Pt7Bads} - E_{1\ ethylene+glob,Pt7Bads} - E_{1\ ethylene,gas}$$

$$E_{3\ ethylene} = E_{3\ ethylene+glob,Pt7Bads} - E_{2\ ethylene+glob,Pt7Bads} - E_{1\ ethylene,gas}.$$

Further statistical analysis is performed through use of the Boltzmann probability for *i*-th configuration (P_i) by taking the Boltzmann distribution of each minimum (e^{-E_i/k_BT}) divided by the sum of the distributions of all relevant low energy minima:

$$P_i = \frac{e^{-E_i/k_BT}}{\Sigma\, e^{-E_i/k_BT}},$$

where E_i is the *i*-th configuration energy of a gas phase cluster cluster (i.e., E_{form} as defined above), adsorbed cluster ($E[\mathrm{Surf} + \mathrm{Pt}_m\mathrm{B}_n]$) or adsorbed cluster with a reagent ($E[\mathrm{Surf} + \mathrm{Pt}_m\mathrm{B}_n + reag]$), k_B is the Boltzmann constant, and *T* is the temperature.

The entropic contribution of relevant minima may also be found by considering the fundamental thermodynamic relation of the Helmholtz free energy ($F = U - TS$). Specifically, the Gibbs' entropy equation (S_G) allows us to analyze the effect of discrete states with their respective Boltzmann probabilities on the ensemble of particular cluster types:

$$S_G = -k_B \sum_i P_i \ln(P_i),$$

where the P_I are the Boltzmann weights and k_B is the Boltzmann constant. In this way, we may analyze the entropic contribution at a catalytically relevant temperature (TS_G).

Intracluster bonding was evaluated through a summation of the electrostatic potential present in a cluster:

$$V_C = k_e \sum_{i,j} \frac{q_i q_j}{r_{i,j}},$$

where q_i and q_j represent two different atoms, $r_{i,j}$ is the distance between them, and k_e is Coulomb's constant $\frac{1}{4\pi\varepsilon_0}$.

B.3 Theoretical Discussion

The geometric diversity present in Pt_7 is enhanced even further in Pt_7B with 10 isomers. This results in a substantial increase in the configurational entropy's contribution to the free energy of the system (Table B.3-B.4). In a previous study, 1:1 ratios of Pt:Pd were preferentially stabilized and sintering-resistant over other ratios of Pt:Pd due to intra-cluster bonding and the configurational entropy arising from the presence of many isomers.[1] Due to the limitation of our cluster sizes, the sintering modality is limited to extrapolation from Pt and B potential energy surfaces. Pt's PES yields typical behavior of ~2 eV sintering penalty, observed in other systems, but B's PES resists facile characterization. The B monomer adsorbs nearly as strongly as the B-doped Pt clusters and distorts the surface by abstracting surface O-Al from their initial positions, raising them by 0.2-2.4 Å (Fig. A.6). Unlike other dopants such as the weakly-bound Zn^2, which can evaporate from oxides such as TiO_2 and MgO, or the mobile Pd/Pt^1 monomers, B will resist sintering by Ostwald ripening (Table B.3). Thus, borated Pt may exhibit considerable stability compared to other dopants due to the stability of the $B\text{-}O_{surf}$ anchor, the entropic influence of many isomers lowering the free energy of the system, and the intracluster attraction present in the clusters.

In order to analyze the effects of both temperature and reagent adsorption on structural reformation, Molecular Dynamics calculations were performed at higher temperatures relevant to catalysis. In a previous publication, we predicted that in pure Pt_7 clusters, prismatic geometries would stabilize to single-layer geometries during ethylene adsorption. We observe this in MD trajectories at 450, 700, and 1000 K. At 450 and 700 K, the prismatic geometry undergoes multiple transformations: it opens up from a prism

to a distorted hexagon (circa MD step 150) and varies between other prismatic configurations and other single-layer configurations. Notably, at 450 K after 2000 MD steps, the prismatic geometry has transformed to a configuration very similar to the single-layer. At higher temperatures such as 1000 K, the cluster may also fragment into extended, branched configurations that may be a precursor to the mobile monomers that contribute to sintering by Ostwald ripening. Moreover, the sp^2 adsorbed ethylene may interconvert to sp^3 adsorption. In MD trajectories of ethylene adsorbed on the single-layer Pt_7, at 450 and 700 K, the stability of this configuration leads to only twisting and rotation of ethylene at circa 2000 MD steps with little to no change in the Pt cluster's geometry.

B.4 References

1. Baxter, E. T.; Ha, M.; Cass, A. C.; Alexandrova, A. N.; Anderson, S. L. *ACS Cat.* **2017**, 7, 3322-3335.

2. Desrosiers, R. M.; Greve, D. W.; Gellman, A. J. *J. Vac. Sci. Tech. A: Vac. Surf. Films.* **1997**, 15, 2181-2189.

3. Krawczyk, M.Appl. *Surf. Sci.* **1998**, 135, 209-217.

4. Rodriguez, J. A.; Truong, C. M.; Corneille, J.; Goodman, D. W. *J. Phys. Chem.* **1992**, 96, 334-341.

5. Ha, M.; Dadras, J.; Alexandrova, A. *ACS Cat.* **2014**, 4, 3570-3580.

6. Dadras, J.; Shen, L.; Alexandrova, A. *J. Phys. Chem. C.* **2015**, 119, 6047-6055.

Table B.1 Formation energies of global minima of Pt_7, Pt_8, and Pt_7B

	Pt_7	Pt_8	Pt_7B
E_{form} (eV)	-27.05	-31.97	-35.38
E_{form}/atom (eV)	-3.86	-4.00	-5.05

Table B.2: Gas phase isomers

Cluster	Isomer	Δ E_{form} (eV)	P_{450K}	P_{1000K}
Pt_7B	I	0.00	59.90%	35.26%
	II	0.06	14.19%	18.44%
	III	0.06	12.84%	17.63%
	IV	0.07	9.72%	15.56%
	V	0.12	2.83%	8.93%
	VI	0.18	0.52%	4.17%

Table B.3: Characteristics of borated platinum vs pure platinum clusters

	Pt_7	Pt_8	Pt_7B
Isomers	5	7	10
$\Sigma P_{450K} E_{ads}$ (eV)	-5.08	-4.89	-4.60
ΔQ (e)	-1.22 to -1.44	-0.94 to -1.24	-0.03 to -1.17
$T_{450K}S_G$ (eV)	0.010	0.002	0.012
$T_{700K}S_G$ (eV)	0.034	0.037	0.061
E_s—Pt		2.17	
E_s—B			3.28

Table B.4: Adsorbed isomers of Pt_7, Pt_8, Pt_7B with Boltzmann populations (P) at experimentally relevant temperatures of 450 and 1000 K and charge transfer (ΔQ) from the support

Cluster	Isomer	Δ E_{form} (eV)	P_{450K}	P_{700K}	ΔQ (e)	V_C (eV)
Pt_7	I	0.00	75.27%	65.89%	-1.22	-3.63
	II	0.04	24.49%	32.02%	-1.44	-1.32
	III	0.24	0.16%	1.26%	-1.33	-1.35
	IV	0.27	0.07%	0.77%	-1.25	-3.29
	V	0.43	<0.01%	0.05%	-1.23	-2.79
	ΣP E_{ads} (eV)		-5.08	-5.07		
	TS_G (eV)		0.010	0.019		
Pt_8	I	0.00	97.65%	87.73%	-1.24	0.99
	II	0.17	1.14%	5.03%	-1.07	0.22
	III	0.19	0.74%	3.82%	-0.94	-1.37
	IV	0.21	0.41%	2.61%	-1.08	0.66
	V	0.30	0.04%	0.57%	-1.22	0.59
	VI	0.39	<0.01%	0.14%	-1.08	0.72
	VII	0.41	<0.01%	0.10%	-0.80	-0.47
	ΣP E_{ads} (eV)		-4.89	-4.87		
	TS_G (eV)		0.002	0.009		
Pt_7B	I	0.00	81.22%	59.26%	-0.37	-11.85
	II	0.10	6.40%	11.57%	-0.70	-25.41
	III	0.10	6.39%	11.56%	-0.44	-10.95
	IV	0.12	3.54%	7.91%	-0.03	-6.83
	V	0.16	1.37%	4.29%	-1.17	-4.49
	VI	0.19	0.62%	2.59%	-0.95	-22.08
	VII	0.21	0.38%	1.88%	-0.96	-30.11
	VIII	0.29	0.05%	0.52%	-0.64	-18.84
	IX	0.31	0.03%	0.34%	-0.91	-30.32
	X	0.39	<0.01%	0.09%	-1.04	-21.92
	ΣP E_{ads} (eV)		-4.66	-4.78		
	TS_G (eV)		0.013	0.036		

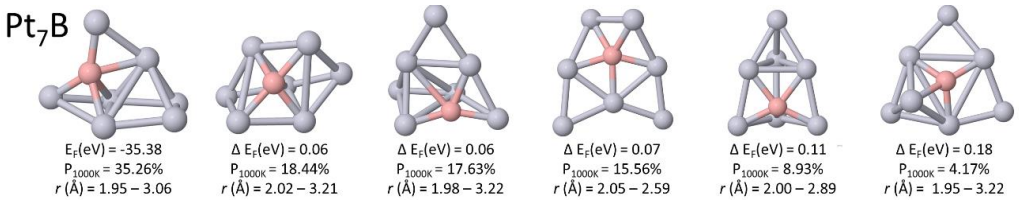

Figure. B.1: Gas phase isomers of Pt_7B at catalytically relevant temperature of 1000K.

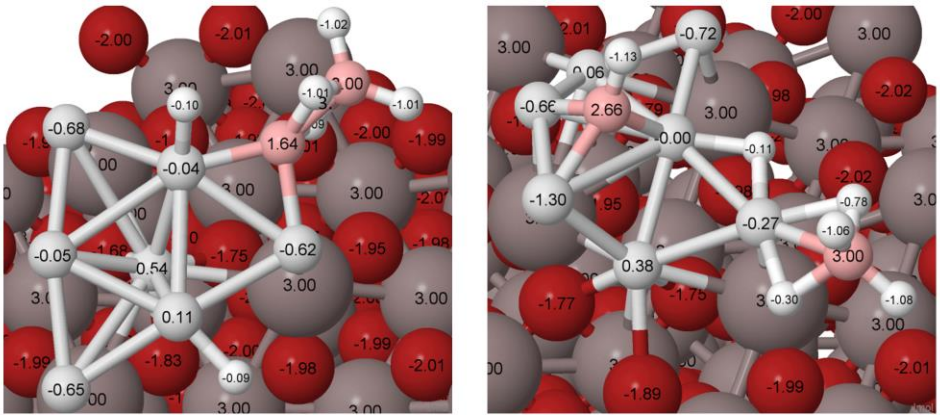

Figure B.2: Global minima of adsorbed diborane on Pt_7, Isomer I (prismatic) and II (single-layer).

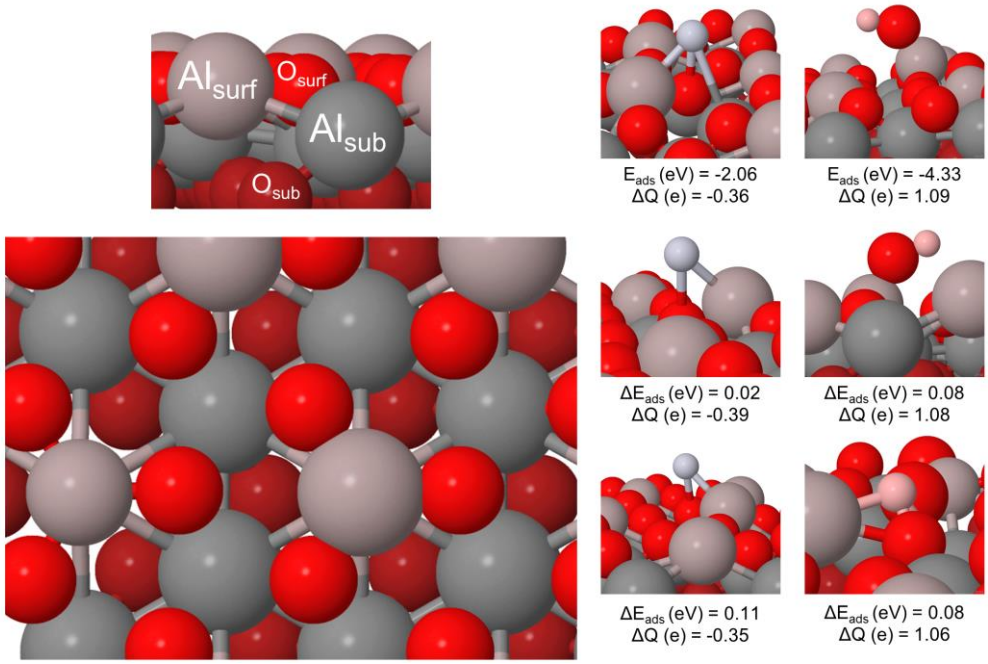

Figure B.3: The highest affinity configurations from Pt (light gray) and B (light pink) potential energy surface calculations.

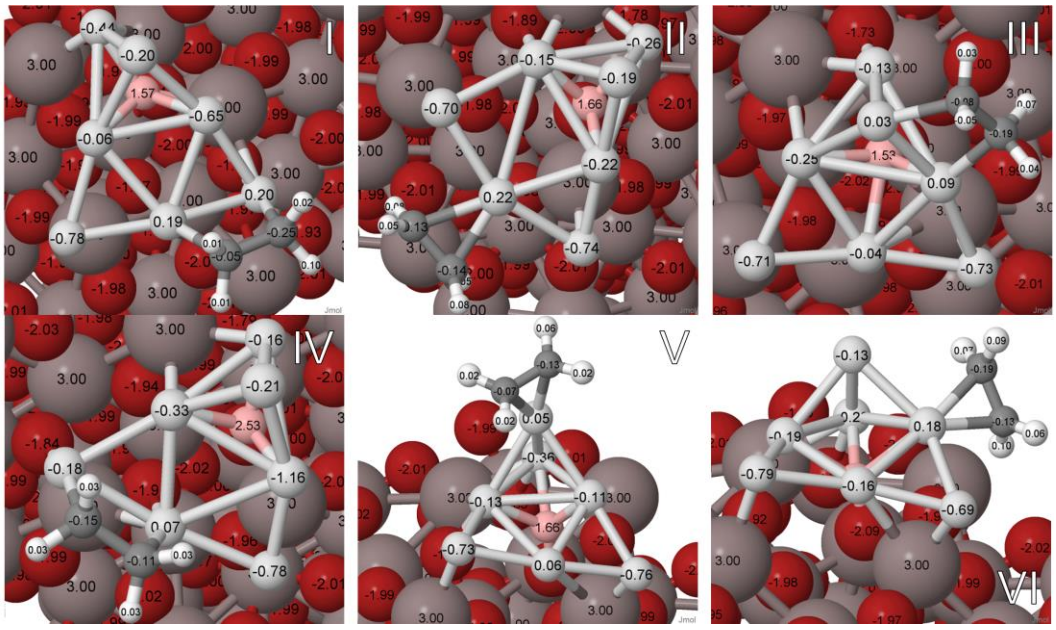

Figure B.4: The lowest minima of ethylene adsorbed on Pt_7B_{glob}.

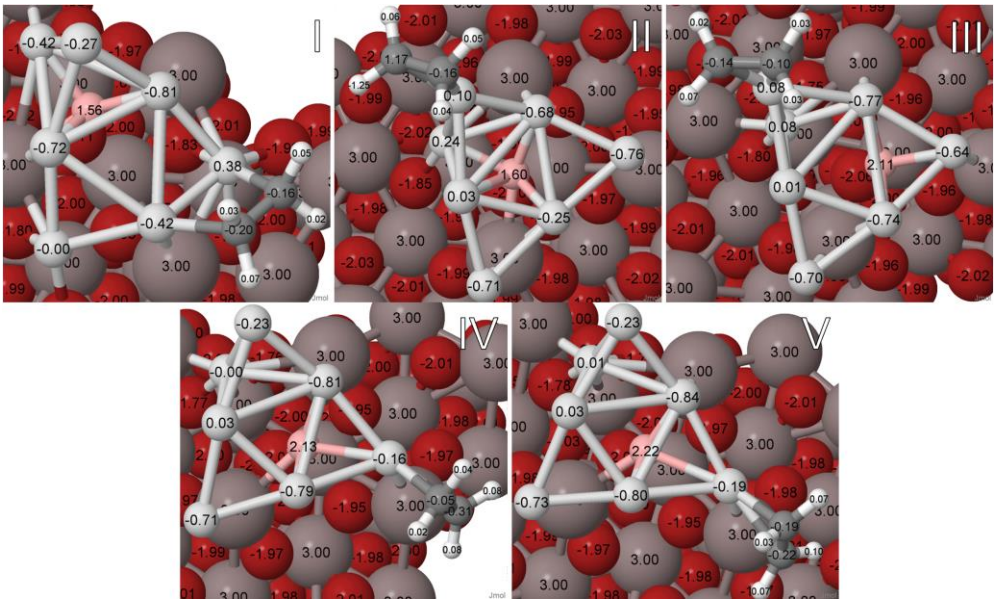

Figure B.5: The lowest minima of ethylene adsorbed on adsorbed Pt_7B, Isomer II.

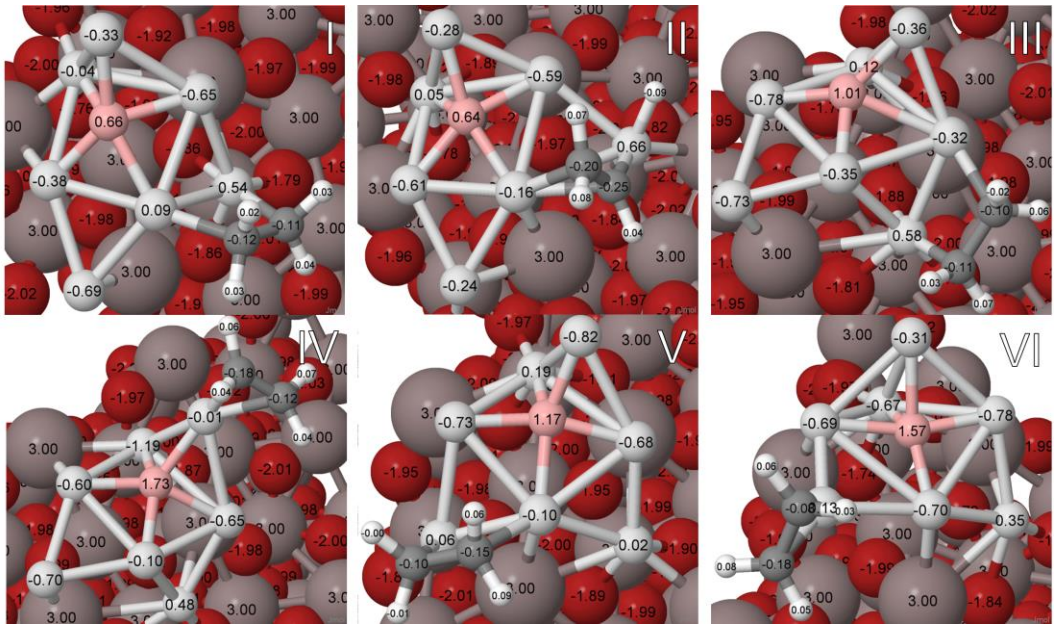

Figure B.6: The lowest minima of ethylene adsorbed on adsorbed Pt_7B, Isomer V.

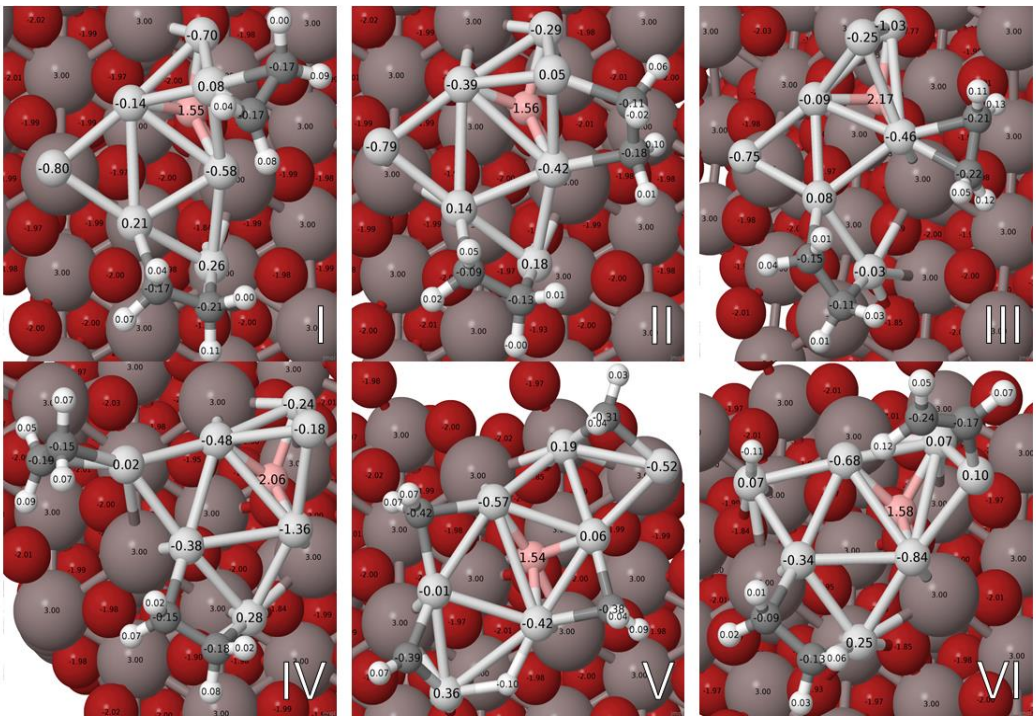

Figure B.7: The lowest minima of 2 ethylene adsorbed on adsorbed Pt_7B, Isomer I.

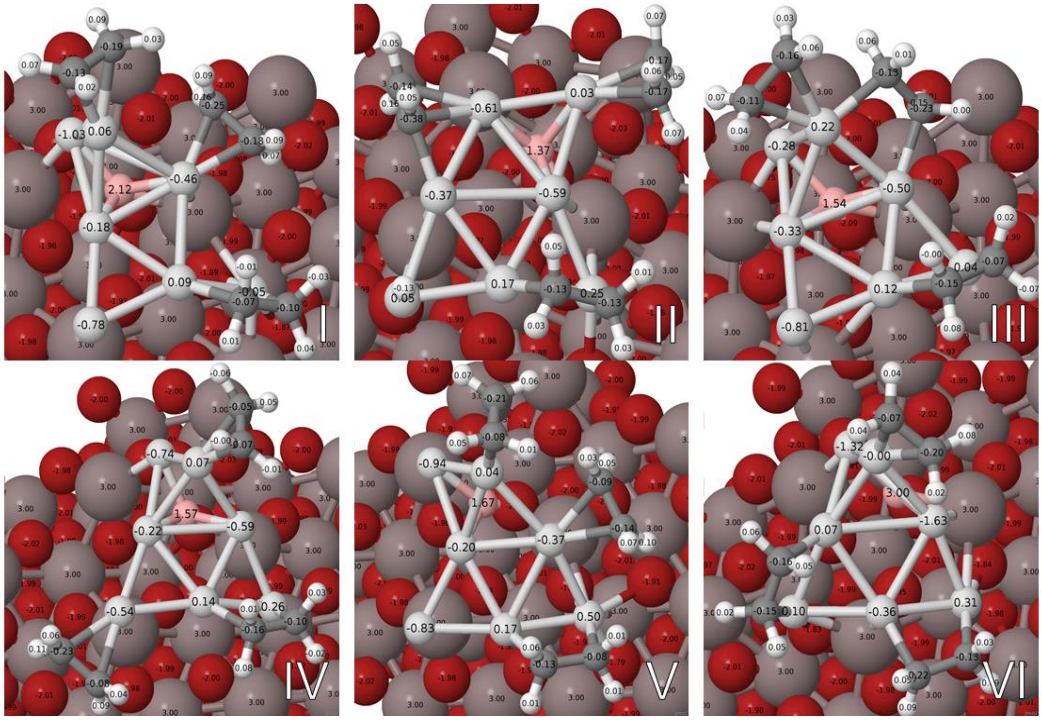

Figure B.8: The lowest minima of 3 ethylene adsorbed on adsorbed Pt_7B, Isomer I.

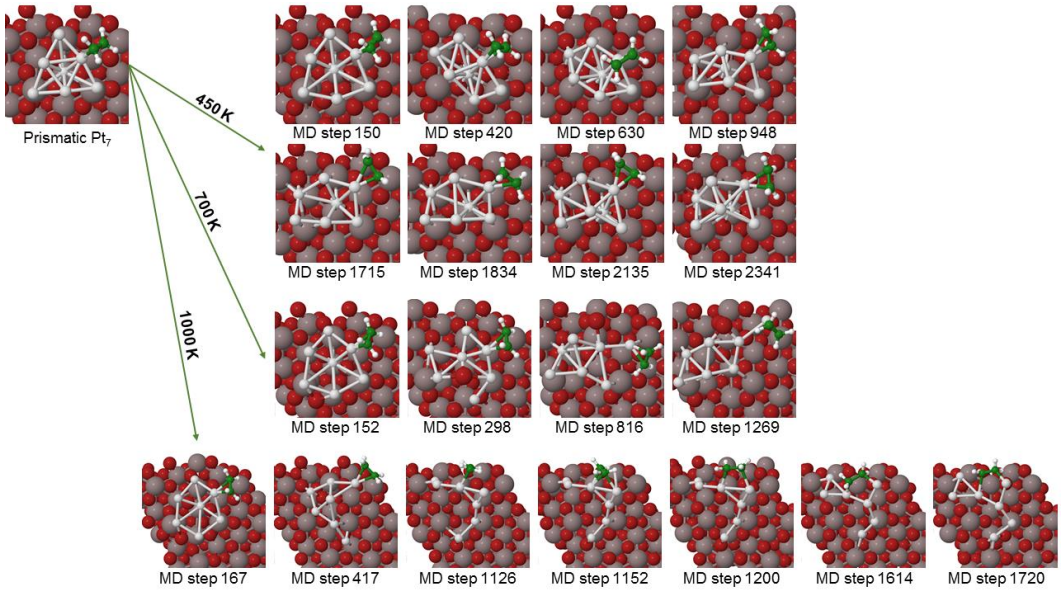

Figure B.9: Highlights from the MD trajectories of ethylene adsorbed on prismatic Pt_7 at catalytically relevant temperatures.

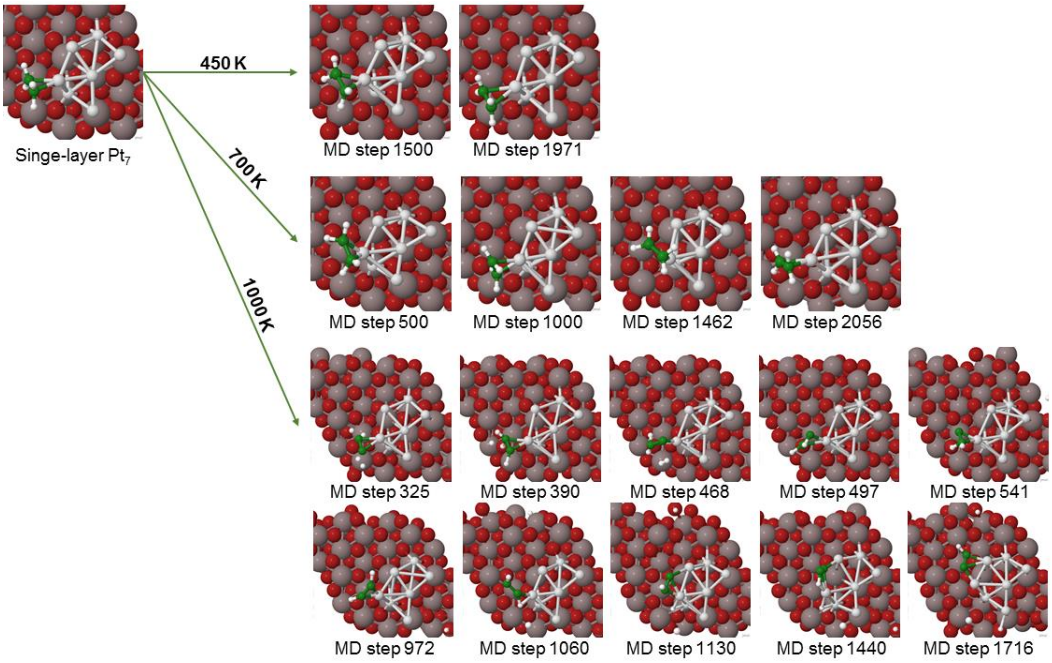

Figure B.10: Highlights from the MD trajectories of ethylene adsorbed on single-layer Pt_7 at catalytically relevant temperatures.

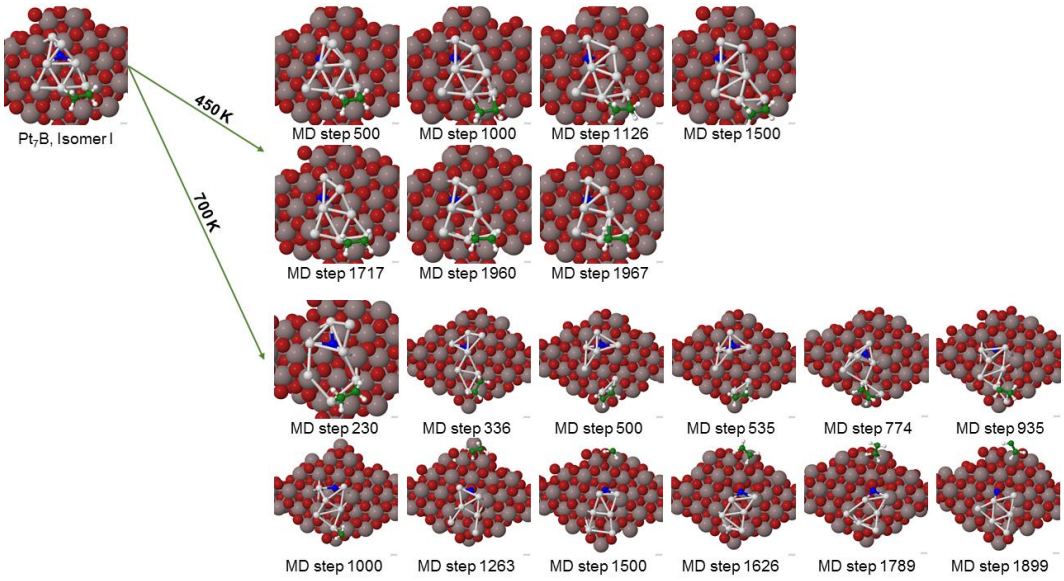

Figure B.11: Highlights from the MD trajectories of ethylene adsorbed on Pt_7B, Isomer I at catalytically relevant temperatures.

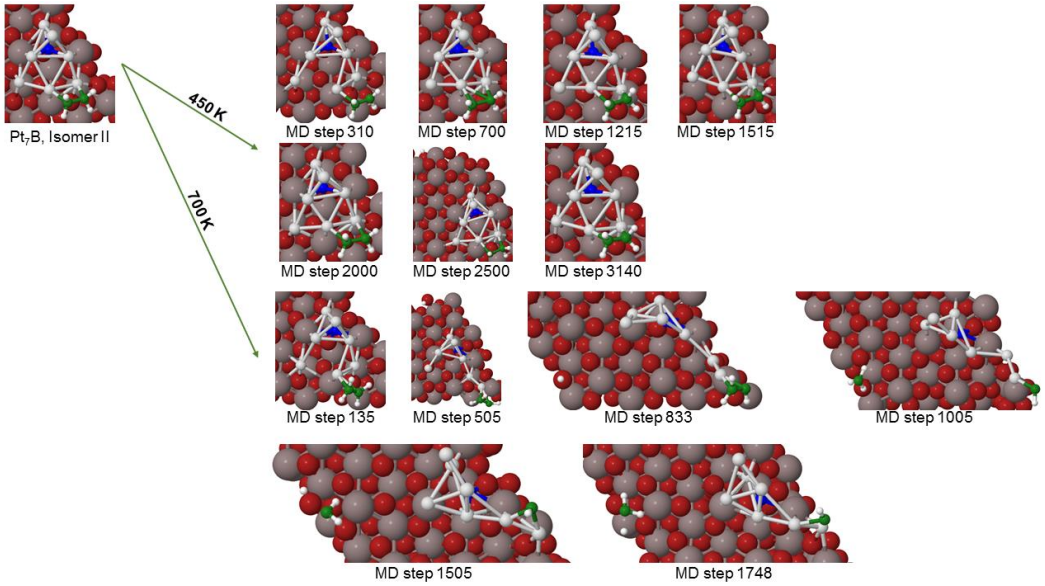

Figure B.12: Highlights from the MD trajectories of ethylene adsorbed on Pt_7B, Isomer II at catalytically relevant temperatures.

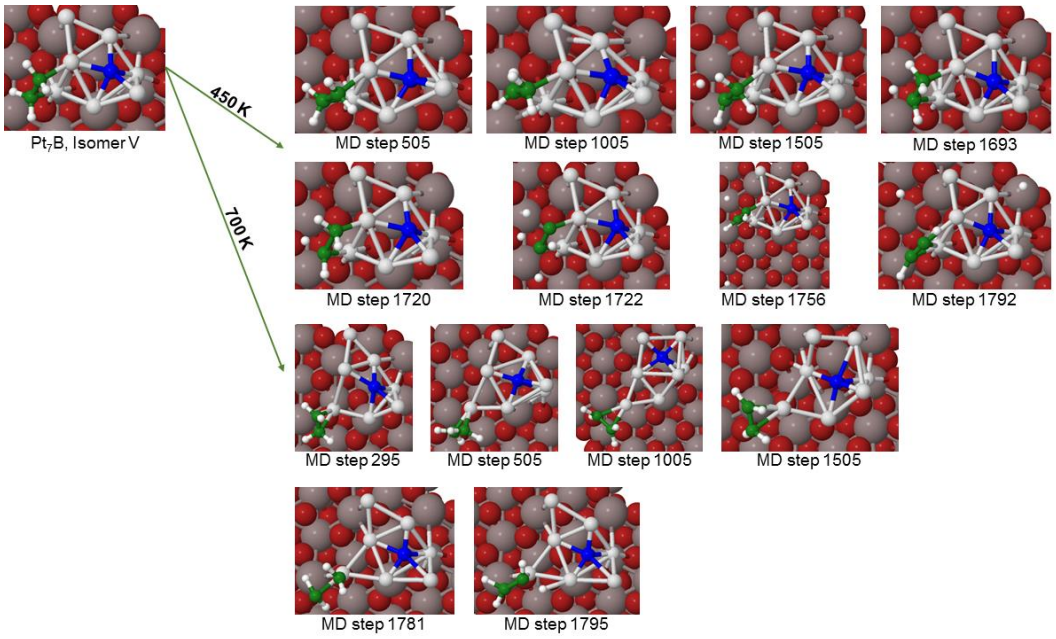

Figure B.13: Highlights from the MD trajectories of ethylene adsorbed on Pt_7B, Isomer V at catalytically relevant temperatures.

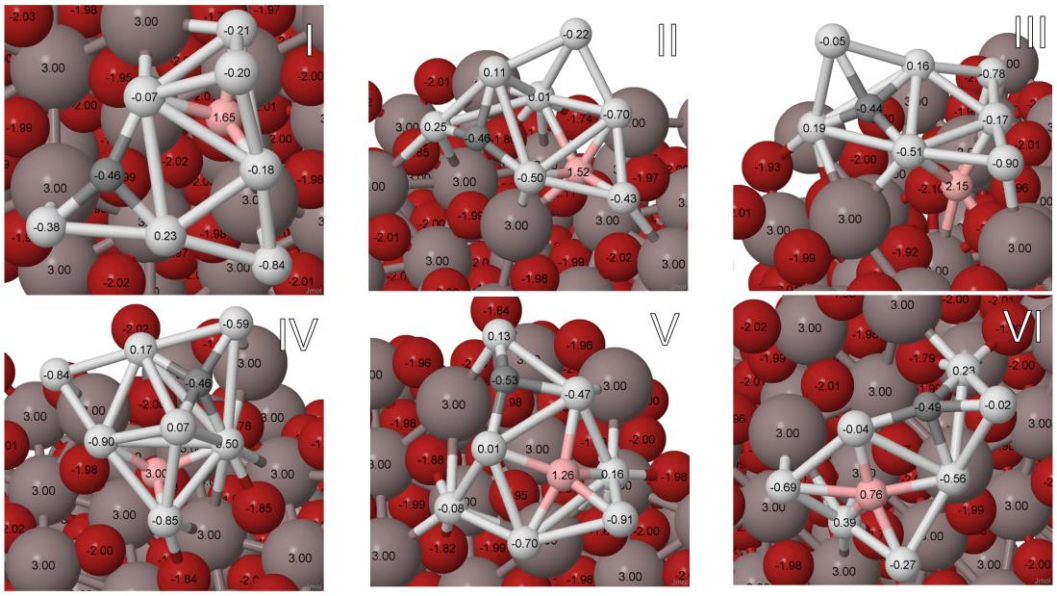

Figure B.14: The C-sticking configurations of the lowest six isomers of Pt_7B.

APPENDIX C

SUPPORTING INFORMATION FOR CHAPTER 4

C.1 TPD Fitting Method and Results

In order to determine the distribution of desorption energies for the various borane products observed, TPD/R spectra were fit to the second order rate equation:

$$I(t)\ \alpha\ \frac{-d\theta}{dt} = (\theta^2(E) \cdot\ \nu)\ e^{\frac{-E}{kT(t)}},$$

where I(t) is the desorption as a function of time, ν is a prefactor, and T(t) is the temperature as a function of time. A distribution of population in sites with different energies for desorption, θ(E), is assumed and ran through the simulation, the calculated $I(t)$ is compared to the experimental desorption versus time, and then θ(E) is adjusted until the simulated I(t) matches the experiment. Because size-selected cluster samples are time consuming to prepare, and irreversibly changed by a single TPD/TPR run, it is simply not practical to extract ν from a series of coverage-dependent experiments on every cluster size. Therefore, the simulations were tested for ν ranging from 10^{13} to 10^{15} s^{-1}, covering a range often found in TPD. The simulated desorption/dehydrogenation energies shift by only ~7% *per* order-of-magnitude variation in ν, and in Figures S2-3 we present the θ(E) distributions obtained for ν = 10^{14} s.

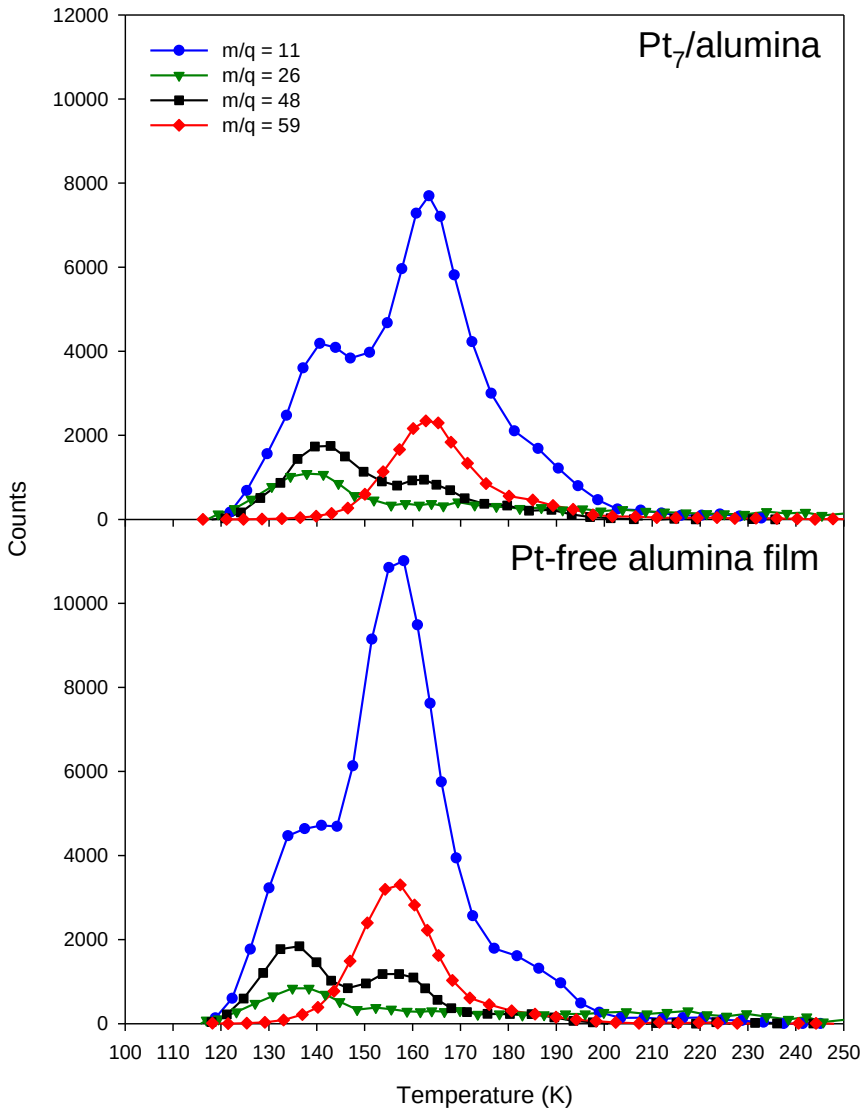

Figure C.1: Raw TPD spectra for select ion masses produced by electron impact ionization of species desorbing from Pt_7/alumina, and from a sample of the alumina/Ta(110) support, following exposure to 1.5 L of diborane at 130 K, followed by heating at 3 K/second.

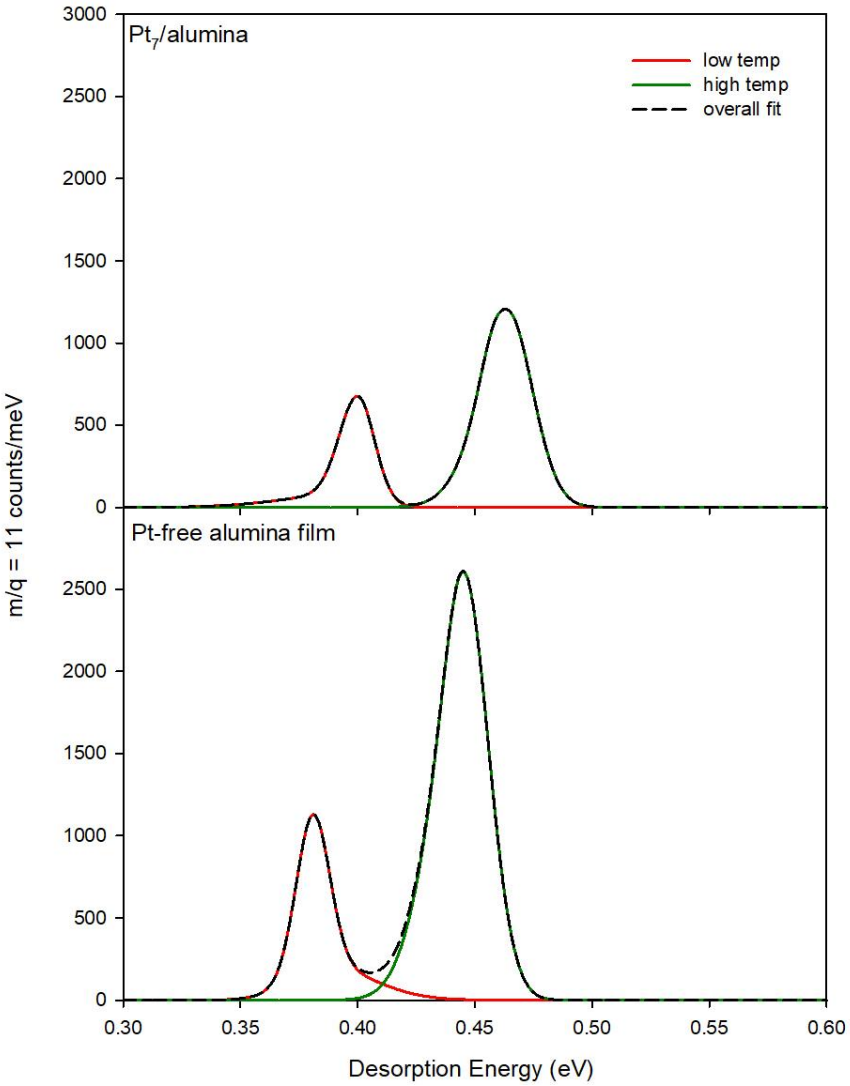

Figure C.2: Desorption energy distributions obtained by fitting the m/q = 11 desorption temperature dependences for B_2H_6 TPD/R experiments on Pt-free alumina and Pt_7/alumina.

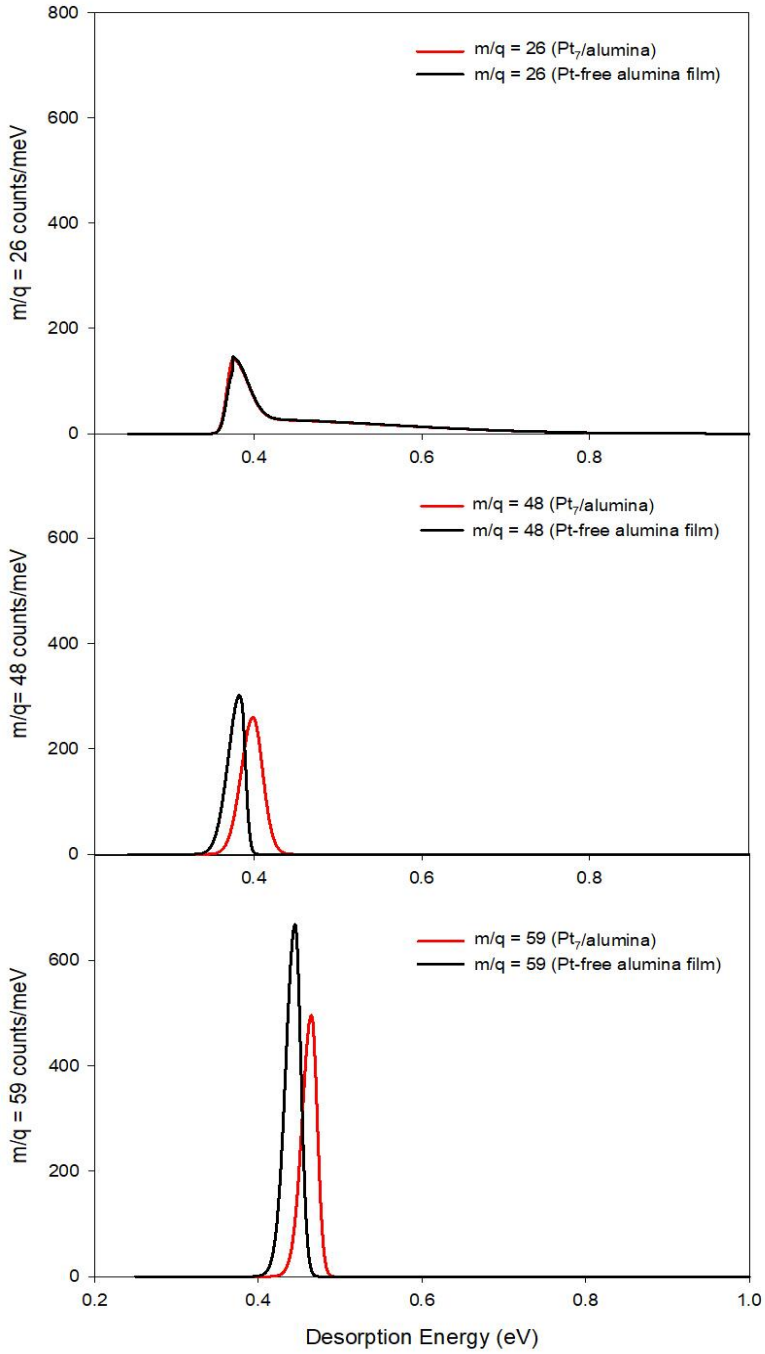

Figure C.3: Desorption energy distributions obtained by fitting the m/q = 26, 48, 59 desorption temperature dependences for B_2H_6 TPD/R experiments on Pt-free alumina and Pt_7/alumina.

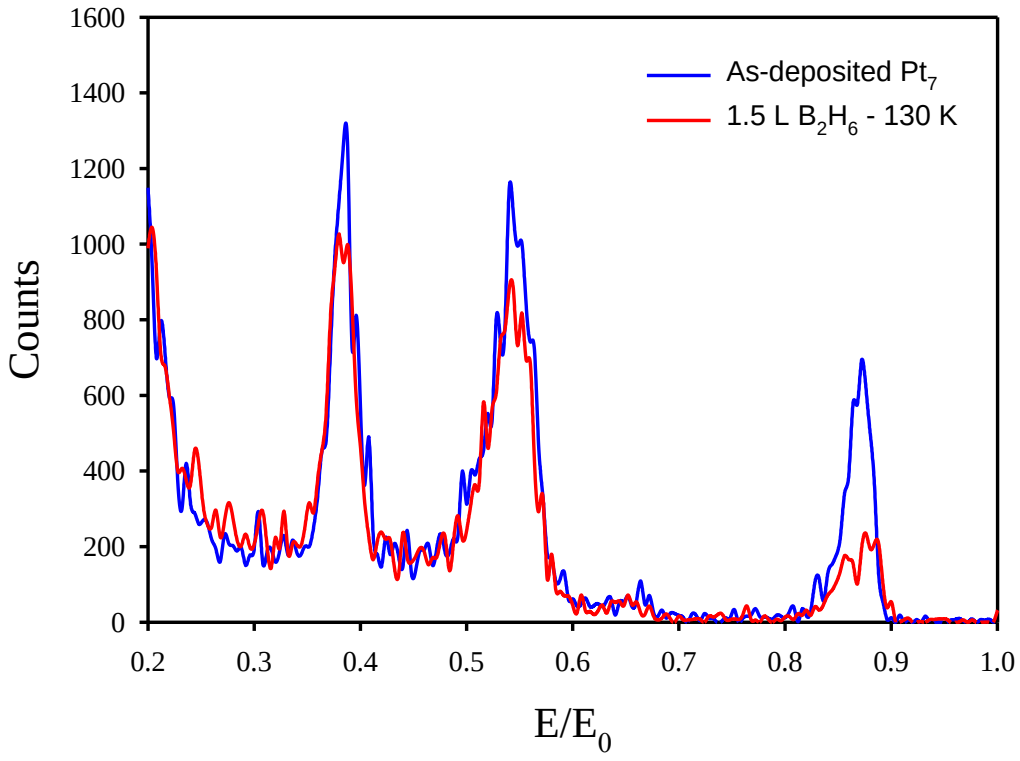

Figure C.4: Raw ISS for Pt_7/alumina samples. A spectrum measured immediately after depositing 0.1 ML of Pt_7 is shown in blue. A spectrum taken immediately after exposing a Pt_7/alumina sample to 1.5 L B_2H_6 at 130 K is shown in red. Note the large attenuation of Pt ISS signal ($E/E_0 \approx 0.93$), and smaller attenuations of the Al and O signals ($E/E_0 \approx 0.6$ and 0.41). Note also that no significant growth of signal is seen in the region expected for boron ($E/E_0 \approx 0.26$) after diborane exposure.

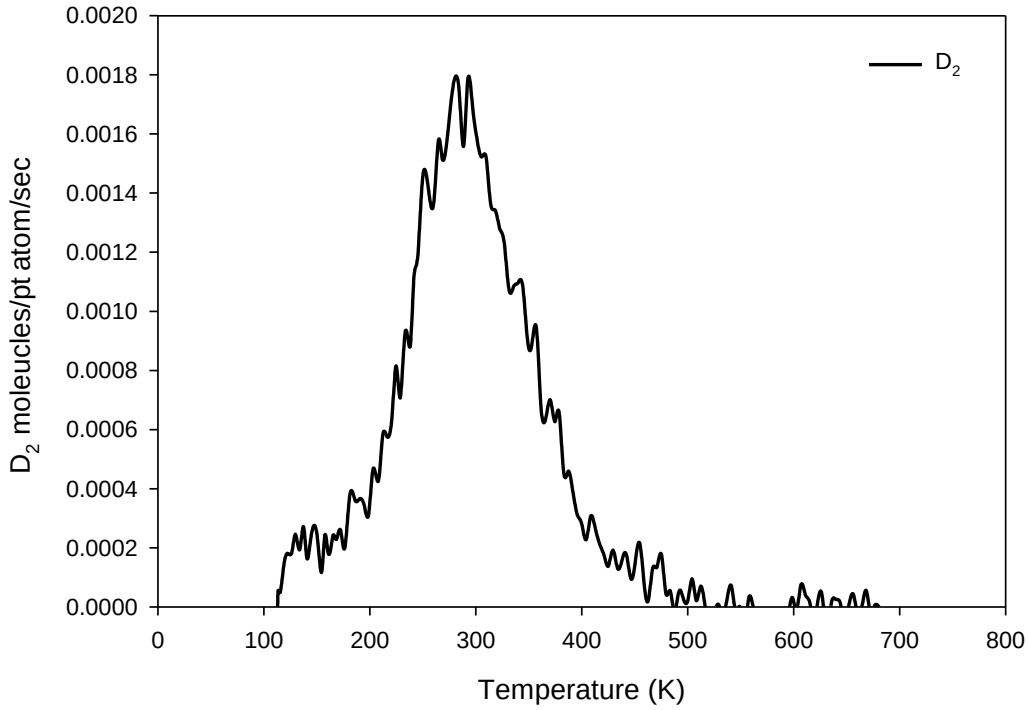

Figure C.5: TPD of D_2 from Pt_7/alumina, dosed with 5 L of D_2 at 130 K, then heated at 3 K/sec.

Computational

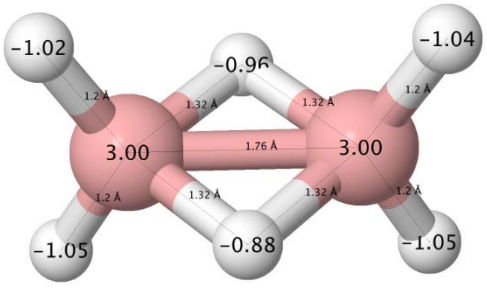

Figure C.6: Gas phase diborane with an E_{form} of -33.90 eV.

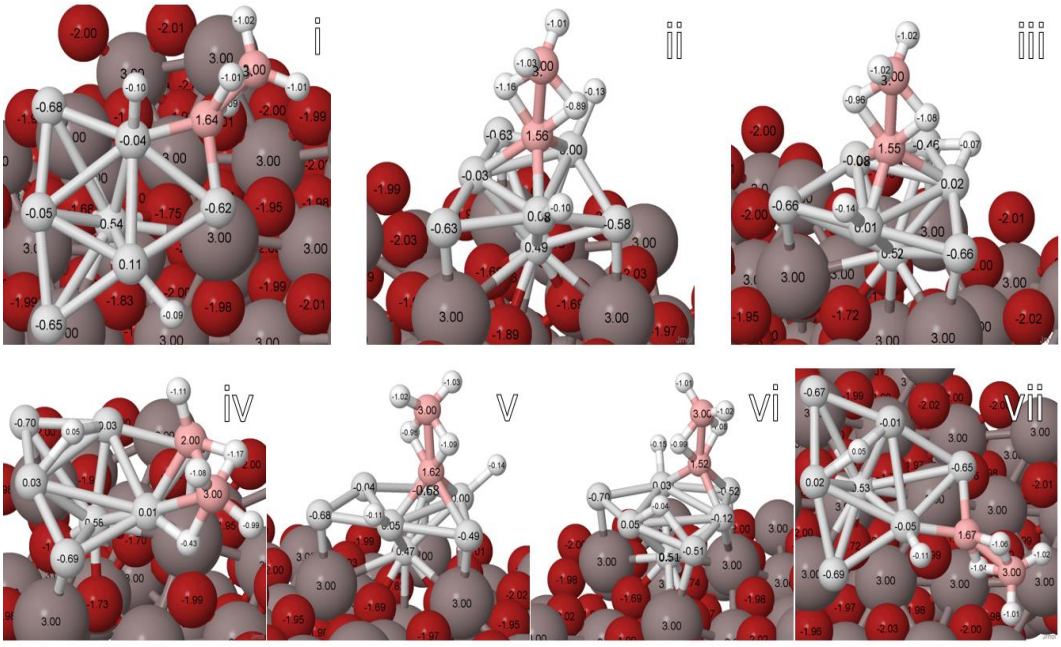

Figure C.7: Local minima of adsorbed diborane on Pt_7, Isomer I (prismatic).

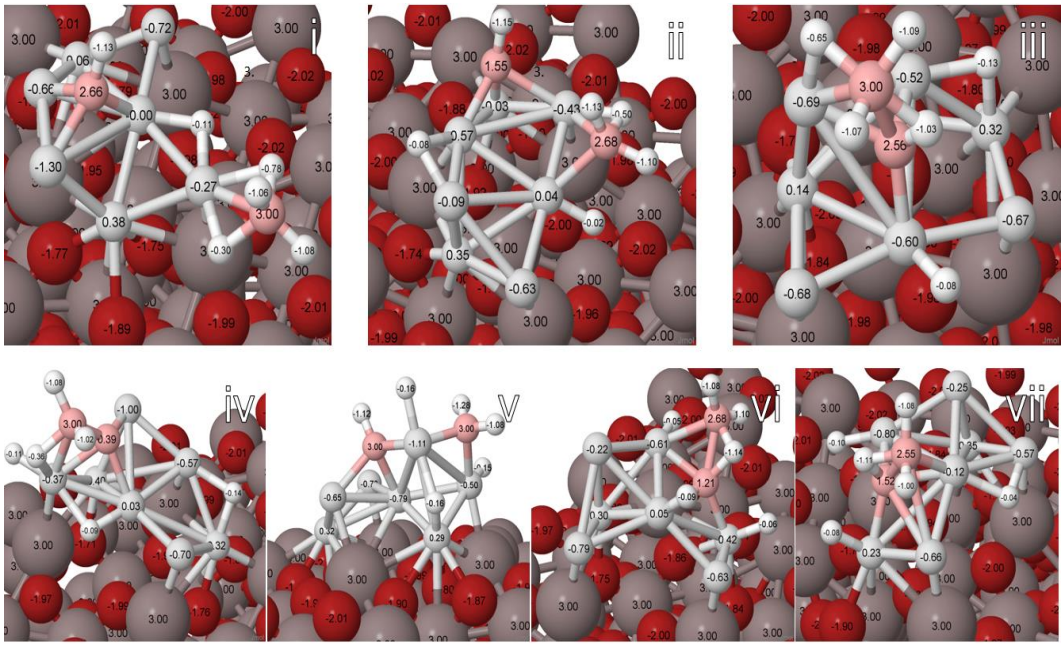

Figure C.8: Local minima of adsorbed diborane on Pt_7, II (single-layer).

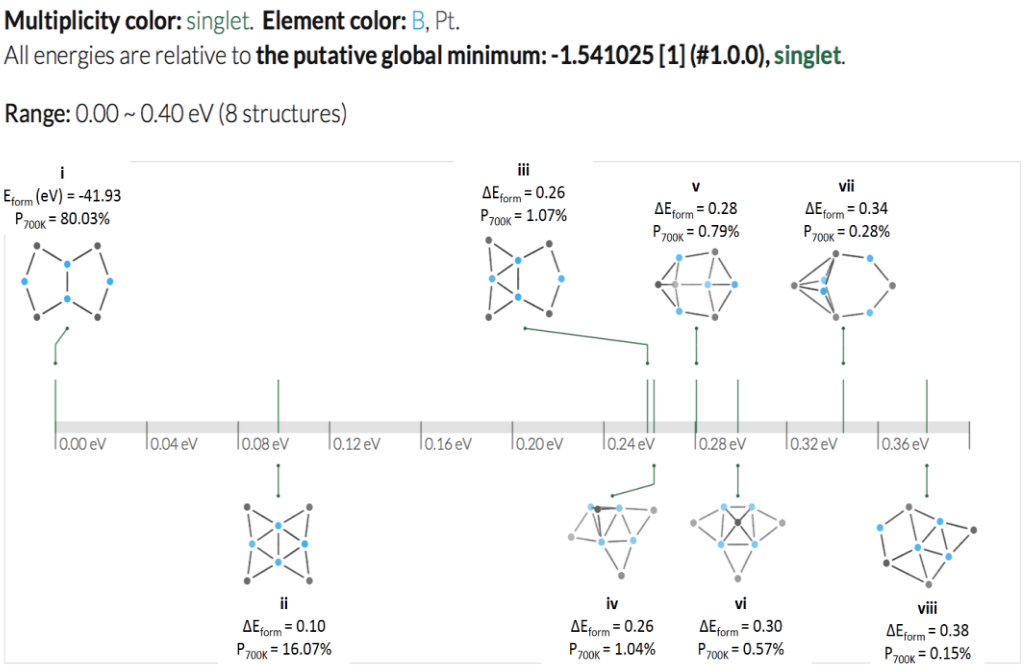

Figure C.9: Local minima of gas phase Pt_4B_4.